AD_____

GRANT NUMBER DAMD17-93-J-3003

TITLE: Wavelet Representations for Digital Mammography

PRINCIPAL INVESTIGATOR: Andrew F. Laine, D.Sc.

CONTRACTING ORGANIZATION: University of Florida
Gainesville, Florida   32611-5500

REPORT DATE: December 1997

TYPE OF REPORT: Annual

PREPARED FOR: Commander
U.S. Army Medical Research and Materiel Command
Fort Detrick, Maryland   21702-5012

DISTRIBUTION STATEMENT: Approved for public release;
distribution unlimited

The views, opinions and/or findings contained in this report are those of the author(s) and should not be construed as an official Department of the Army position, policy or decision unless so designated by other documentation.

REPORT DOCUMENTATION PAGE

1. AGENCY USE ONLY *(Leave blank)*	2. REPORT DATE December 1997	3. REPORT TYPE AND DATES COVERED Annual (16 Nov 96 - 15 Nov 97)

4. TITLE AND SUBTITLE

Wavelength Representations for Digital Mammography

5. FUNDING NUMBERS

DAMD17-93-J-3003

6. AUTHOR(S)

Laine, Andrew F., D.Sc.

7. PERFORMING ORGANIZATION NAME(S) AND ADDRESS(ES)

University of Florida
Gainesville, Florida 32611-5500

8. PERFORMING ORGANIZATION REPORT NUMBER

9. SPONSORING / MONITORING AGENCY NAME(S) AND ADDRESS(ES)

U.S. Army Medical Research and Materiel Command
Fort Detrick, Maryland 21702-5012

10. SPONSORING / MONITORING AGENCY REPORT NUMBER

11. SUPPLEMENTARY NOTES

12a. DISTRIBUTION / AVAILABILITY STATEMENT

Approved for public release; distribution unlimited

12b. DISTRIBUTION CODE

19980722 013

13. ABSTRACT *(Maximum 200 words)*

The goal of this project is to develop an interactive diagnostic tool for radiologists that shall refine the perception of mammographic features (including lesions, masses and calcifications). By improving the visualization of breast pathology we can increase the chances of early detection of breast cancers (improve quality) while requiring less time to evaluate mammograms for most patients (lower costs).

We are investigating a methodology for accomplishing mammographic feature analysis through multiresolution representations. We show that overcomplete representations may be used to detect and enhance specific mammographic features within a continuum of scale space. Such "focused" reconstructions can allow a radiologist to examine interactively diagnostic features within a selected scale space.

The improved contrast of mammographic features make these techniques appealing for computed aided diagnosis (CAD) and screening mammography. Screening mammography examinations are certain to grow substantially in the next few years, and analytic methods that can assist general radiologists in reading mammograms shall be of great importance.

14. SUBJECT TERMS

Breast Cancer, Digital Mammography, Contrast Enhancement, Multiscale Representations, Wavelet Analysis.

15. NUMBER OF PAGES
134

16. PRICE CODE

17. SECURITY CLASSIFICATION OF REPORT Unclassified	18. SECURITY CLASSIFICATION OF THIS PAGE Unclassified	19. SECURITY CLASSIFICATION OF ABSTRACT Unclassified	20. LIMITATION OF ABSTRACT Unlimited

FOREWORD

Opinions, interpretations, conclusions and recommendations are those of the author and are not necessarily endorsed by the U.S. Army.

_____ Where copyrighted material is quoted, permission has been obtained to use such material.

_____ Where material from documents designated for limited distribution is quoted, permission has been obtained to use the material.

_____ Citations of commercial organizations and trade names in this report do not constitute an official Department of Army endorsement or approval of the products or services of these organizations.
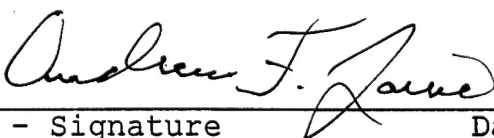
_____ In conducting research using animals, the investigator(s) adhered to the "Guide for the Care and Use of Laboratory Animals," prepared by the Committee on Care and Use of Laboratory Animals of the Institute of Laboratory Resources, National Research Council (NIH Publication No. 86-23, Revised 1985).

_____ For the protection of human subjects, the investigator(s) adhered to policies of applicable Federal Law 45 CFR 46.

_____ In conducting research utilizing recombinant DNA technology, the investigator(s) adhered to current guidelines promulgated by the National Institutes of Health.

_____ In the conduct of research utilizing recombinant DNA, the investigator(s) adhered to the NIH Guidelines for Research Involving Recombinant DNA Molecules.

_____ In the conduct of research involving hazardous organisms, the investigator(s) adhered to the CDC-NIH Guide for Biosafety in Microbiological and Biomedical Laboratories.

_____ 3-22-98
PI - Signature   Date

Table of Contents

3 Conclusions

List of Figures

1 Introduction

Breast cancer is the most frequently diagnosed malignancy among women in the United States [1]. In 1996 the American Cancer Society estimates that 184,300 women will be newly diagnosed with breast cancer and that 44,300 will die from the disease [1]. Breast cancer accounts for 31% of all cancers detected and 17% of all cancer deaths, and ranks as the second leading cause of death from cancer among women in the United States [1]. Five year survival rates are generally very high (93%) for breast cancer staged as being localized, falling to 72% for regional disease and only 18% for distant disease [2]. The early detection of breast cancer is clearly a key ingredient of any strategy designed to reduce breast cancer mortality.

Mammography's role is the early detection of breast cancer. Although more accurate than any other modality, existing techniques for mammography only find 80 to 90% of the breast cancers. Moreover, in 7 to 10% of cases, the cancer will not be visible on the mammogram. It has been suggested that mammograms as normally viewed, display only about 3% of the total information detected. Perception is a problem particularly for patients with dense fibroglandular patterns. The importance of diagnosis of breast cancer at an early stage is critical to patient survival. The general inability to detect small tumors and other salient features within mammograms motivates our investigation.

The goal of this project is to develop an interactive diagnostic tool for radiologists that shall refine the perception of mammographic features (including lesions, masses and calcifications) and improve the accuracy of diagnosis. By improving the visualization of breast pathology we can increase the chances of early detection of breast cancers (improve quality) while requiring less time to evaluate mammograms for most patients (lower costs). We are investigating a methodology for accomplishing mammographic feature analysis through multiresolution representations. We have shown that overcomplete representations may be identified and used to detect and enhance specific mammographic features within a continuum of scale space. Such "focused" reconstructions may complement existing modalities and allow a radiologist to examine interactively diagnostic features within a selected scale space. Similar to traditional coarse to fine matching strategies, the radiologist may first choose to look for coarse features (e.g. dominant mass) within low frequency levels of a wavelet transform and later examine finer features (e.g. microcalcifications) at higher frequency levels.

A major reason for poor visualization of small malignant masses is the subtle difference in x-ray attenuation between normal glandular tissues and malignant disease [3]. This fact makes the detection of small malignancies problematical, especially in younger women who

have denser breast tissue. Although calcifications have high inherent attenuation properties, their small size also results in a low subject contrast [4]. As a result, the visibility of small tumors, and any associated microcalcifications, will always be a problem in mammography as it is currently performed using analog film.

In this report, we describe in detail results accomplished during the past year. Presented below in executive summary, we encapsulate progress related to the specific tasks and objectives stated in Phases III, IV and V of our Statement of Work.

In the sections below, we describe in overview, our processing algorithms, experimental methods and sample results obtained. In addition, we list in summary, publications of our researchers accomplished during the past year of our investigation. Finally, we include our response to the reviewers comments and suggestions regarding contractual and technical issues in reference to last year's report.

1.1 Overview of Contents

Enhancement via Fusion of Mammographic Features

Existing methods of mammographic image enhancement can be divided roughly into two categories: (1) methods aimed at better visualization of all features present in an image, and (2) methods that target specific features of importance (e.g., microcalcifications, stellate lesions). Methods from the first category are not optimized for a specific type of cancer, while methods in the second category are typically tailored for a single type of malignancy only. We present a synthesis of the two paradigms by means of image fusion to overcome these shortcomings and practical limitations.

Both processing for enhancement of selected features and fusion of the resultant images were accomplished within a single wavelet transform framework. We chose a multiscale spline derivative-based transform with wavelets equal to the second derivative of a central B-spline function. Such a transform not only includes the two-dimensional discrete dyadic wavelet transform decomposition as its subset, but also enables incorporation of a variety of known wavelet based image enhancement methods. Enhancement and fusion of mammographic features within a single transform framework enabled both efficient implementation and independent optimization of processing modules.

Detection of Subtle Masses in Mammography via Precision Multiscale Analysis

We introduce a continuous scale wavelet detector for identifying masses (possible breast cancers) in mammograms. Continuous-scale wavelet algorithms have been discussed in the past, however this is the first reported algorithm that uses a scaled version of the same mother wavelet at each scale of analysis. This single mother wavelet property leads to a

simpler implementation and a more direct application of detection theory to recognition problems than traditional multiscale analysis. In addition, we show that a continuous-scale search is necessary for computer aided diagnosis of mammography since traditional solutions using dyadic scales (powers of two) either fail to detect some masses or signal too many false alarms. Our novel wavelet detector combines a wavelet formulation with the classical theory of constant false alarm rate (CFAR) detectors. We show that our algorithm is able to detect masses in dense mammograms that could not be seen using conventional windowing and leveling or other traditional methods of contrast enhancement.

Coherence of Multiscale Features for Digital Mammogram Enhancement

Mammographic features are extracted according to their coherence and orientation. In this chapter of the report, an artifact free enhancement algorithm based on overcomplete multiscale wavelet analysis is presented. First, an image was decomposed using a fast wavelet transform algorithm. At the same time, the energy and phase information at each level are determined using a set of separable steerable filters. Then, a measure of coherence within each level is obtained by weighting an energy measure with the ratio of projections of the energy within a specified window onto the central point of a window with respect to the total energy within each window. Finally, a nonlinear operation, integrating coherence and orientation information, is applied to modify transform coefficients within distinct levels of analysis. These modified coefficients are then reconstructed, via an inverse fast wavelet transform, resulting in an improved visualization of mammographic features. The novelty of this algorithm lies in its detection of directional features and reconstruction without artifacts. This algorithm represents the "state-of-the-art" of multiscale enhancement approaches, and is the algorithm of choice for our ongoing ROC studies.

A Lifting Algorithm for Overcomplete Wavelet Representations for Interactive Feature Analysis

The Fourier transform has been the traditional mathematical tool in wavelet processing because operations of a wavelet family defined by translates and dilates become algebraic operations in Fourier space. However, the Fourier transform is not efficient if the filter length involved is fairly short, and may not be applicable to problems on more complex domains. In addition, since wavelet functions dealing with bounded inputs are not translation invariant, the Fourier transform is best not used as a construction tool of wavelets. To overcome these drawbacks, we propose a flexible and efficient tool of analysis, namely *overcomplete lifting scheme*, which will be used to compute overcomplete wavelet representations (in real time) for interactive mammographic feature analysis.

1.2 Publications

Below, we list in summary, an update of publications accomplished during 1997.

1. D. Chen, A. Laine, J. G. Harris, and W. Huda, "A continuous scale discrete wavelet transform for the detection of spicular masses in mammograms," submitted to *IEEE Transactions on Signal Processing*, February 1997.

2. D. Ioannou, W. Huda, A. F. Laine, and I. Koren, "Enhancement of computer simulated masses for mammography via wavelet analysis," submitted to *IEEE Transactions on Medical Imaging*, January 1997.

3. I. Koren, A. Laine, and F. Taylor, "Enhancement via fusion of mammographic features," submitted to *IEEE International Conference on Image Processing*, Chicago, IL, October 1998.

4. M. Shim and A. Laine, "Overcomplete lifted wavelet representations for multiscale feature analysis," submitted to *IEEE International Conference on Image Processing*, Chicago, IL, October 1998.

5. I. Koren and A. Laine, "A discrete dyadic wavelet transform for multidimensional feature analysis," in M. Akay (Editor), *Time-Frequency and Wavelets in Biomedical Signal Engineering*, New York, NY: IEEE Press, 1998, pp. 425–449.

6. S. Schuler and A. Laine, "Hexagonal QMF banks and wavelets," in M. Akay (Editor), *Time-Frequency and Wavelets in Biomedical Signal Engineering*, New York, NY: IEEE Press, 1998, 451–472.

7. D. Chen, C.-M. Chang, and A. Laine, "Detection and enhancement of small masses via precision multiscale analysis," in *Proceedings of the Third Asian Conference on Computer Vision*, Hong Kong, PRC, January 1998, vol. 1, pp. 192–199.

8. A. Laine, W. Huda, J. Honeyman, and B. Steinbach, "Wavelet representations for digital mammography," in *Proceedings of the Department of Defense Breast Cancer Research Program Meeting Era of Hope*, Washington, D.C., October–November 1997, vol. 1, pp. 105–106.

9. I. Koren, A. Laine, and F. Taylor, "An overcomplete enhancement of digital mammograms," in *Proceedings of the Department of Defense Breast Cancer Research Program Meeting Era of Hope*, Washington, D.C., October–November 1997, vol. 1, pp. 107–108.

10. X. Zong, A. Meyer-Baese, and A. Laine, "Multiscale segmentation through a radial

basis neural network," in *Proceedings of the IEEE International Conference on Image Processing*, Santa Barbara, October 1997, vol. 3, pp. 400–403.

11. C.-M. Chang and A. Laine, "Enhancement of mammograms from oriented information," in *Proceedings of the IEEE International Conference on Image Processing*, Santa Barbara, October 1997, vol. 3, pp. 524–527.

1.3   Responses to Technical and Contractual Issues

With regard to the ROC studies mentioned in Phase V of our SOW, we include below a description of an ongoing investigation. The ROC studies have been delayed due to the fact that the principal investigator and two of the three principal collaborators of the project within the Department of Radiology at the University of Florida, resigned their positions to accept new academic positions at other institutions. The length of the project, has been extended to accommodate this adjustment and allow successful completion of the project. In addition, new personnel affiliated with Columbia-Presbyterian Hospital, Department of Radiology, Columbia University, will assist in carrying out the final ROC studies described in Phase V of the Statement of Work. We expect that these studies will be complete within six months time.

Performance Study: We will use an existing national mammography database (currently under development at the University of South Florida and Massachusetts General Hospital under the supervision of Dr. Bowyer and Dr. Kopans, respectively) in order to carry out a receiver operating characteristic (ROC) study to evaluate the effect of multiscale enhancement (MSE) on the diagnostic performance of radiologists. The study will use 360 four-view clinical cases: 180 cases with cancer proved by means of biopsy and 180 cases with negative findings at examination and follow-up. To measure the radiologists performance with and without MSE, the 360 cases will be divided into three groups of 120 cases each (randomly chosen.) The study will be conducted in two phases. In each phase all 360 cases will be prepared on an alternator in random order. During the first phase, cases in the first group will be presented with four original views and enhanced images, while cases in the second and third groups will be presented with only four original views. Similarly, during the second phase, cases in the second group will be presented with four original views and MSE images, while cases in the first and third groups will be presented with only four original views. Eight weeks will be allowed between the two phases of the study to minimize any potential learning by the observers. Each phase will be divided into six reading sessions on separate days. During each session an observer will read one-sixth

Table 1: Case distribution.

Total number of cases	360
Number of normal cases	180
Number of malignant cases	180
Number of phases	2
Number of groups per phase	3
Number of cases per group	120
Number of sessions per phase	6
Number of cases per session	60

Table 2: Reading conditions for each group of cases.

Group	Cases with MSE	
	Phase 1	Phase 2
1	All	None
2	None	All
3	None	None

of the mammograms (60 cases) sequentially. Table 1 and Table 2 show a summarized description of the performance study.

Six mammographers will participate in the ROC study. None of the observers will be informed of the prevalence rate or have previous exposure to the cases in the study. In each session the observers will be required to rate for each case their confidence regarding the presence of malignancy using a five category scale (1 = definitely not present, 2 = probably not present, 3 = possibly present, 4 = probably present, 5 = definitely present.)

ROC analysis [5, 6] will be employed to compare the observers performance in detecting the presence of malignancy with and without MSE. For each observer, the accuracy index A_z will be calculated for each group of cases. The differences in A_z between phases one and two for a given group will indicate if the performance of an observer increased or decreased with MSE. Table 2 summarizes the reading conditions for each group of cases. The first group will measure the change in A_z when the cases are first presented with the computerized outputs as ancillary films. The second group will measure the change in A_z when the cases are first presented without the computerized outputs. The third group serves as a control and will measure the change (if any) when the cases are presented to the observers twice without computerized outputs. By means of this study we will learn whether or not mammographers perform better in the detection of small malignancies

when MSE images are made available.

2 Body

2.1 Enhancement via Fusion of Mammographic Features

2.1.1 Introduction

In mammography, early detection of breast cancer relies upon the ability to distinguish between malignant and benign mammographic features. The detection of small malignancies and subtle lesions is often difficult. Contrast enhancement can make more obvious unseen or barely seen features of a mammogram without requiring additional radiation.

Existing methods of mammographic image enhancement can be divided roughly into two categories: (1) methods aimed at better visualization of all features present in an image [7, 8, 9, 10], and (2) methods that target specific features of importance (e.g., microcalcifications [11, 12, 13], stellate lesions [14]). Methods from the first category are not optimized for a specific type of cancer, while methods in the second category are typically tailored for a single type of malignancy only. In this chapter, we present a novel approach which overcomes these shortcomings and problematic limitations.

Since diagnostic features in mammograms appear in a variety of shapes and sizes, traditional image enhancement techniques such as histogram equalization and unsharp masking seldom produce satisfactory results and are clearly outperformed by more sophisticated methods [9, 10]. Due to their ability to analyze images across different scales, wavelet-based techniques have become particularly popular for processing of mammograms [7, 8, 9, 11, 12, 13]. The majority of researchers lean toward redundant wavelet representations which do not introduce significant processing artifacts such as aliasing inherent to orthogonal and biorthogonal wavelet transforms. Here, we continue with a generalization of the discrete dyadic wavelet transform started in our previous report and concentrate on wavelets that are equal to the second derivative of a central B-spline function.

This chapter is organized as follows: in Sections 2.1.2 and 2.1.3 a discrete dyadic wavelet transform in one and two dimensions, respectively, is presented. Next, Section 2.1.4 explains a novel approach of transform-based feature enhancement via image fusion. Section 2.1.5 then describes transform implementation in detail. Finally, Section 2.1.6 provides a conclusion.

2.1.2 1-D Discrete Dyadic Wavelet Transform Revisited

Let us begin with a brief review of properties of the one-dimensional discrete dyadic wavelet transform as described in our previous report, but included here for completeness.

The dyadic wavelet transform of a function $s(x) \in L^2(\mathbf{R})$ is defined as a sequence of functions

$$\{W_m s(x)\}_{m \in \mathbf{Z}}, \tag{1}$$

where $W_m s(x) = s * \psi_m(x) = \int_{-\infty}^{\infty} s(t) \, \psi_m(x-t) \, dt$, $\psi_m(x) = 2^{-m} \psi(2^{-m} x)$ is a wavelet $\psi(x)$ expanded by a dilation parameter (or scale) 2^m, and "$*$" denotes the convolution operator. To ensure coverage of the frequency axis the requirement on the Fourier transform of $\psi_m(x)$ is the existence of $A_1 > 0$ and $B_1 < \infty$ such that

$$A_1 \le \sum_{m=-\infty}^{\infty} |\hat{\psi}(2^m \omega)|^2 \le B_1$$

is satisfied almost everywhere. The constraint on the Fourier transform of the (nonunique) reconstructing function $\chi(x)$ is

$$\sum_{m=-\infty}^{\infty} \hat{\psi}(2^m \omega) \, \hat{\chi}(2^m \omega) = 1.$$

A function $s(x)$ can then be completely reconstructed from its dyadic wavelet transform using the identity

$$s(x) = \sum_{m=-\infty}^{\infty} W_m s * \chi_m(x),$$

where $\chi_m(x) = 2^{-m} \chi(2^{-m} x)$.

In numerical applications, processing is performed on discrete rather than continuous functions. When the function to be transformed is in the discrete form, the scale 2^m can no longer vary over all $m \in \mathbf{Z}$. Finite sampling rate prohibits the scale from being arbitrarily small, while computational resources restrict the use of an arbitrarily large scale. Let the finest scale be normalized to 1 and the coarsest scale set to 2^M.

The smoothing of a function $s(x) \in L^2(\mathbf{R})$ is defined as

$$S_m s(x) = s * \phi_m(x),$$

where $\phi_m(x) = 2^{-m} \phi(2^{-m} x)$ with $m \in \mathbf{Z}$, and $\phi(x)$ is a smoothing function (i.e., its integral is equal to 1 and $\phi(x) \to 0$ as $|x| \to \infty$).

Mallat and Zhong [15] selected a real smoothing function $\phi(x)$, whose Fourier transform satisfied

$$|\hat{\phi}(\omega)|^2 = \sum_{m=1}^{\infty} \hat{\psi}(2^m \omega) \, \hat{\chi}(2^m \omega). \tag{2}$$

In addition, it was shown that any discrete function of finite energy $s(n) \in l^2(\mathbf{Z})$ can be written as the uniform sampling of some function smoothed at scale 1, i.e., $s(n) = S_0 f(n)$, where $f(x) \in L^2(\mathbf{R})$ is not unique. Thus, the discrete dyadic wavelet transform of $s(n)$ for any coarse scale 2^M was defined as a sequence of discrete functions

$$\{S_M f(n+s), \{W_m f(n+s)\}_{m \in [1,M]}\}_{n \in \mathbf{Z}},$$

where s is a $\psi(x)$ dependent sampling shift.

The above initialization $s(n) = S_0 f(n)$ is rather standard in the discrete wavelet transform computation [16], although it yields correct results (i.e., the discrete wavelet transform is equal to the samples of its continuous counterpart) only when $s(n) = S_0 s(n)$. Here, we will concentrate on wavelets which are derivatives of spline functions and this will lead us to a simple initialization procedure [17] that alleviates the above problem.

For a certain choice of wavelets, the discrete dyadic wavelet transform can be implemented within a fast hierarchical digital filtering scheme. Next, we shall summarize the relations between filters, wavelets, and smoothing functions.

First, let us introduce a real smoothing function $\varphi(x)$ such that (2) can be rewritten as[1]

$$\hat{\phi}(\omega)\,\hat{\varphi}(\omega) = \sum_{m=0}^{\infty} \hat{\psi}(2^m \omega)\,\hat{\chi}(2^m \omega), \tag{3}$$

and let us set

$$\phi(x) = \beta_p(x) = \frac{1}{p!} \sum_{i=0}^{p+1} (-1)^i \binom{p+1}{i} \left(x + \frac{p+1}{2} - i\right)^p u\left(x + \frac{p+1}{2} - i\right), \tag{4}$$

where $\beta_p(x)$ denotes a central B-spline of order p. With the choice (4), we restrict ourselves to wavelets which are spline functions.

Computing (3) for the finest two scales shows that

$$\hat{\psi}(\omega)\,\hat{\chi}(\omega) = \hat{\beta}_p(\omega)\,\hat{\varphi}(\omega) - \hat{\beta}_p(2\omega)\,\hat{\varphi}(2\omega). \tag{5}$$

$\hat{\beta}_p(2\omega)$ can be related to $\hat{\beta}_p(\omega)$ by expressing $\hat{\beta}_p(2\omega)$ as (cf. Proposition 1 of [17])

$$\hat{\beta}_p(2\omega) = \frac{1}{2^{p+1}} \left(\frac{\sin(\omega)}{\sin\left(\frac{\omega}{2}\right)}\right)^{p+1} \left(\frac{\sin\left(\frac{\omega}{2}\right)}{\frac{\omega}{2}}\right)^{p+1},$$

and using $\sum_{m=0}^{M} e^{j(m\omega+\theta)} = \frac{\sin\left(\frac{(M+1)\omega}{2}\right)}{\sin\left(\frac{\omega}{2}\right)} e^{j\left(\frac{M\omega}{2} + \theta\right)}$:

$$\hat{\beta}_p(2\omega) = \left(\cos\left(\frac{\omega}{2}\right)\right)^{p+1} \hat{\beta}_p(\omega). \tag{6}$$

---

[1]Note that the sum index determines the range of scales of the discrete transform: using (2) we have $\hat{\psi}(2\omega)$ and $\hat{\chi}(2\omega)$ at the finest scale of the transform, while for (3) we get $\hat{\psi}(\omega)$ and $\hat{\chi}(\omega)$.

(Note that a relation similar to (6) can be derived for integer scales provided that the dilation parameter and the order p are not both even [17].)

Let $F(\omega)$ be a digital filter frequency response and let $F_s(\omega) = e^{j\omega s}F(\omega)$.

If we choose

$$\hat{\psi}(\omega) = G_{-s}(\omega)\,\hat{\beta}_p(\omega), \tag{7}$$

$$\hat{\varphi}(2\omega) = L_s(\omega)\,\hat{\varphi}(\omega), \tag{8}$$

$$\hat{\chi}(\omega) = K_s(\omega)\,\hat{\varphi}(\omega), \tag{9}$$

and

$$H(\omega) = e^{j\omega s}\left(\cos\left(\frac{\omega}{2}\right)\right)^{p+1}, \tag{10}$$

where $s \in \{0, \frac{1}{2}\}$ is a filter dependent sampling shift needed for $g(n)$, $l(n)$, $k(n)$, and $h(n)$ to be FIR filters, and insert Equations (6)–(10) into (5), we observe the relation between frequency responses of the filters

$$G(\omega)K(\omega) + H(\omega)L(\omega) = 1. \tag{11}$$

Similar to orthogonal and biorthogonal discrete wavelet transforms, the discrete dyadic wavelet transform can be implemented within a hierarchical filtering scheme. To derive such a digital filtering scheme, let us assume that $\hat{s}(\omega)$ from (1) is bandlimited to $[-\pi, \pi]$. Using Shannon's sampling theorem [18] and (7) in the definition of the dyadic wavelet transform (1) with $m=0$ shows

$$W_0 s(x) = \int_{-\infty}^{\infty} \sum_{i=-\infty}^{\infty} s(i)\mathrm{sinc}(t-i) \sum_{m=-\infty}^{\infty} g_{-s}(m)\beta_p(x-t-m)\,dt.$$

By making use of the fact that the cardinal spline functions $\eta_r(x)$ tend to the sinc function as their order r approaches infinity [19], and employing

$$\eta_r(x) = \sum_{i=-\infty}^{\infty} b_r^{-1}(i)\beta_r(x-i), \tag{12}$$

where $b_r^{-1}(n)$ denotes a direct B-spline filter [20], we can write

$$\widehat{W_0 s}(\omega) \simeq S(\omega)B_r^{-1}(\omega)\hat{\beta}_r(\omega)\,\hat{\beta}_p(\omega)\,G_{-s}(\omega),$$

or, by using (6) and (10),

$$\mathcal{F}\{W_m s(x)|_{x=n}\} \simeq S(\omega)\,B_r^{-1}(\omega)\,B_{p+r+1}(\omega)\,G_{-s}(2^m\omega)\prod_{i=0}^{m-1}H_{-s}(2^i\omega). \tag{13}$$

20
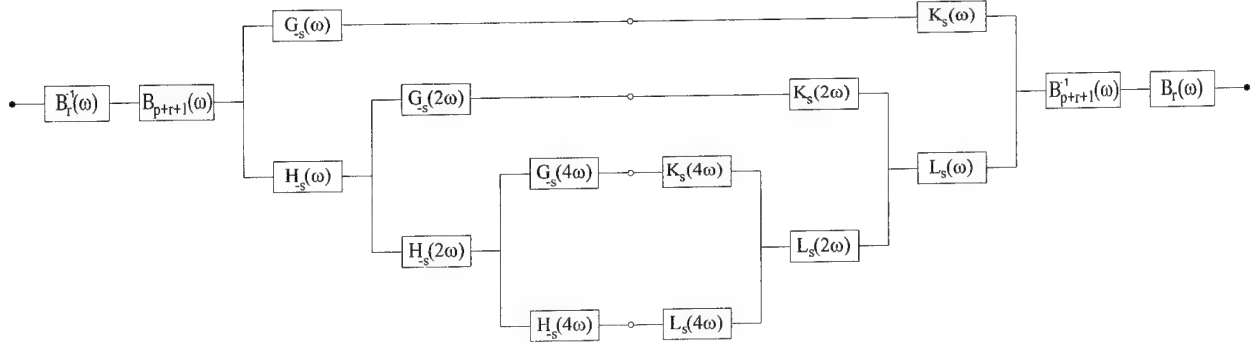
Figure 1: Filter bank implementation of a one-dimensional discrete dyadic wavelet transform decomposition (left) and reconstruction (right) for three levels of analysis.

Equation (13) entirely specifies the discrete dyadic wavelet transform decomposition, while the reconstruction follows from (5)–(10). Three levels of a filter bank implementation are shown in Figure 1. Note that the initialization is the same as the one proposed in [17] and that except for the prefiltering and postfiltering, this scheme is implementing "algorithme à trous" [21]. Noninteger shifts at scale 1 for filters with $s = \frac{1}{2}$ are rounded to the nearest integer.

Next, we choose filters in the filter bank implementation of the discrete dyadic wavelet transform. As previously mentioned, we are interested in wavelets which are derivatives of spline functions. From the property of the central B-spline functions [22]

$$\frac{\partial \beta_p(x)}{\partial x} = \beta_{p-1}\left(x + \frac{1}{2}\right) - \beta_{p-1}\left(x - \frac{1}{2}\right),$$

it follows that $G(\omega)$ in (7) is the Fourier transform of the difference operator centered around $-s$:

$$G(\omega) = e^{j\omega s}\left(2j\sin\left(\frac{\omega}{2}\right)\right)^d, \tag{14}$$

where d is the order of the derivative and the sampling shift for this filter is $s = \frac{d \bmod 2}{2}$. Since $H(\omega)$ was already given by (10), the remaining two filters to be determined are $L(\omega)$ and $K(\omega)$. Both of them are (as is true for $\varphi(x)$ and $\chi(x)$) nonunique.

If we choose $L(\omega)$ such that we can express $K(\omega)$ in terms of a finite geometric series having the smallest number of elements for an arbitrary p, we get

$$L(\omega) = e^{-j\omega s}\sum_{m=1}^{\lfloor\frac{d+1}{2}\rfloor}(-1)^{m+1}\binom{\lfloor\frac{d+1}{2}\rfloor}{m}\left(\cos\left(\frac{\omega}{2}\right)\right)^{(p+1)(2m-1)} \tag{15}$$

and

$$K(\omega) = \frac{1}{(2j)^d}\left(e^{-j\omega s}\sin\left(\frac{\omega}{2}\right)\right)^{d \bmod 2}\left(\sum_{m=0}^{p}\left(\cos\left(\frac{\omega}{2}\right)\right)^{2m}\right)^{\lfloor\frac{d+1}{2}\rfloor}, \tag{16}$$

Table 3: Impulse responses $h(n)$, $g(n)$, $l(n)$, and $k(n)$ for $p=0$ and $d \in \{1,2,3\}$.

n	$h(n)$	$d=1$			$d=2$			$d=3$		
		$g(n)$	$l(n)$	$k(n)$	$g(n)$	$l(n)$	$k(n)$	$g(n)$	$l(n)$	$k(n)$
-2								1		
-1	0.5	1			1			-3	-0.125	
0	0.5	-1	0.5	-0.25	-2	0.5	-0.25	3	0.625	0.0625
1			0.5	0.25	1	0.5		-1	0.625	-0.0625
2									-0.125	

where $\lfloor x \rfloor$ denotes the largest integer smaller than x, the sampling shift for $L(\omega)$ is the same as the one for $H(\omega)$ (i.e., $s = \frac{(p+1)\bmod 2}{2}$), and the sampling shift for $K(\omega)$ is the same as the one for $G(\omega)$.

Note that Equations (10) and (14)–(16) work fine from the mathematical point of view, but in practice the reconstruction may become cumbersome when both p and d are large. (The lengths of impulse responses $h(n)$, $g(n)$, $l(n)$, and $k(n)$ are $p+2$, $d+1$, $(p+1)(d-(d+1)\bmod 2)+1$, and $pd+(p+1)(d\bmod 2)+1$, respectively, while for the frequency responses of the decomposition filters we observe that $\lim_{p\to\infty} |H_{-s}(\omega)| = \delta_u(\omega + 2n\pi)$ and $\lim_{d\to\infty}(2j)^{-d}|G_{-s}(\omega)| = \delta_u(\omega + (2n+1)\pi)$ with $n \in \mathbf{Z}$.)

It is also worth noting that $K(\omega)$ is a lowpass filter when p is even (i.e., the reconstruction function $\chi(x)$ is a wavelet only for p odd).

Tables 3, 4, and 5 list impulse responses of the four filters for $p \in \{0,1,2\}$ and $d \in \{1,2,3\}$, while Figure 2 shows the corresponding wavelets $\psi(x) = \frac{d^d \beta_{p+d}(x)}{dx^d}$. Wavelets from this family have a support of length $d+p+1$, regularity order p, and are either symmetric or antisymmetric.

2.1.3 2-D Discrete Dyadic Wavelet Transform Revisited

In two dimensions, the dyadic wavelet transform of a function $s(x,y) \in L^2(\mathbf{R}^2)$ is defined as a set of functions [15]

$$\{W_m^1 s(x,y), W_m^2 s(x,y)\}_{m \in \mathbf{Z}}, \tag{17}$$

where $W_m^i s(x,y) = s * \psi_m^i(x,y)$ for $i = \{1,2\}$ and $\psi_m^i(x,y) = 2^{-2m}\psi^i(2^{-m}x, 2^{-m}y)$ are wavelets $\psi^i(x,y)$ expanded by a dilation parameter 2^m.

To ensure coverage of the frequency space there must exist $A_2 > 0$ and $B_2 < \infty$ such that

$$A_2 \leq \sum_{m=-\infty}^{\infty} \sum_{i=1}^{2} |\hat{\psi}^i(2^m \omega_x, 2^m \omega_y)|^2 \leq B_2$$

Table 4: Impulse responses $h(n)$, $g(n)$, $l(n)$, and $k(n)$ for $p=1$ and $d \in \{1,2,3\}$.

	$h(n)$	$d=1$		$d=2$	
n	$l(n)$	$g(n)$	$k(n)$	$g(n)$	$k(n)$
-1	0.25	1	-0.0625	1	-0.0625
0	0.5	-1	-0.3125	-2	-0.375
1	0.25		0.3125	1	-0.0625
2			0.0625		

	$d=3$			
n	$h(n)$	$g(n)$	$l(n)$	$k(n)$
-3			-0.015625	
-2		1	-0.09375	0.00390625
-1	0.25	-3	0.265625	0.04296875
0	0.5	3	0.6875	0.1015625
1	0.25	-1	0.265625	-0.1015625
2			-0.09375	-0.04296875
3			-0.015625	-0.00390625

Table 5: Impulse responses $h(n)$, $g(n)$, $l(n)$, and $k(n)$ for $p=2$ and $d \in \{1,2,3\}$.

		$d=1$			$d=2$		
n	$h(n)$	$g(n)$	$l(n)$	$k(n)$	$g(n)$	$l(n)$	$k(n)$
-2	0.125			-0.015625			-0.015625
-1	0.375	1	0.125	-0.109375	1	0.125	-0.125
0	0.375	-1	0.375	-0.34375	-2	0.375	-0.46875
1	0.125		0.375	0.34375	1	0.375	-0.125
2			0.125	0.109375		0.125	-0.015625
3				0.015625			

	$d=3$			
n	$h(n)$	$g(n)$	$l(n)$	$k(n)$
-4			-0.001953125	0.000244140625
-3			-0.017578125	0.003662109375
-2	0.125	1	-0.0703125	0.0263671875
-1	0.375	-3	0.085937	0.0908203125
0	0.375	3	0.50390625	0.13037109375
1	0.125	-1	0.50390625	-0.13037109375
2			0.0859375	-0.0908203125
3			-0.0703125	-0.0263671875
4			-0.017578125	-0.003662109375
5			-0.001953125	-0.000244140625
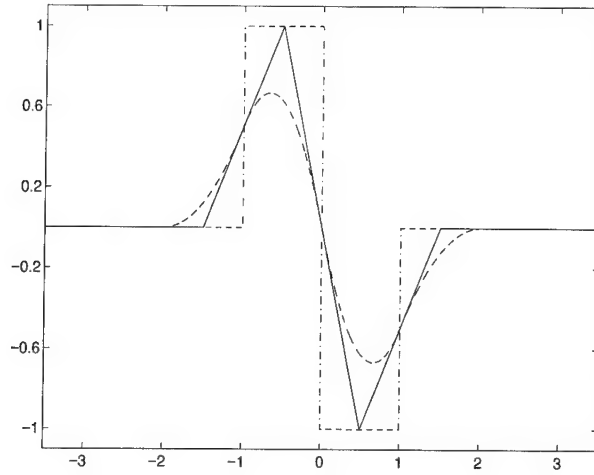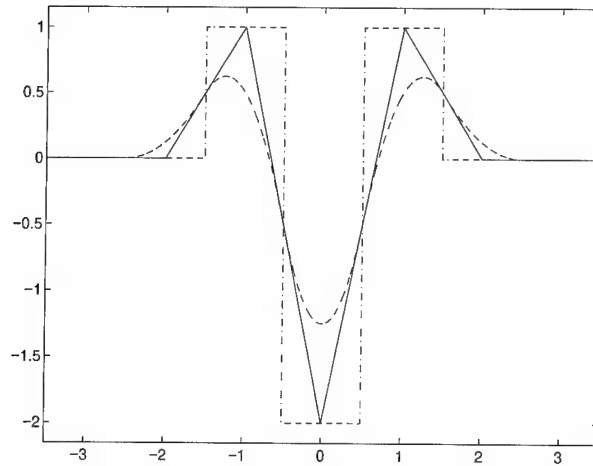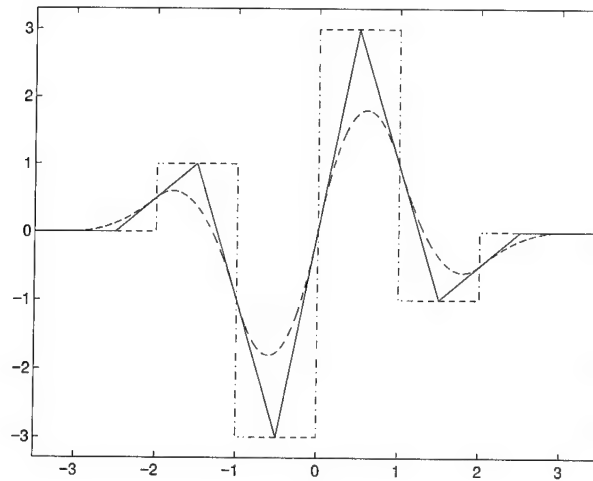
Figure 2: Wavelets (a) $\psi(x) = \frac{d\beta_{p+1}(x)}{dx}$, (b) $\psi(x) = \frac{d^2\beta_{p+2}(x)}{dx^2}$, and (c) $\psi(x) = \frac{d^3\beta_{p+3}(x)}{dx^3}$ for $p=0$ (dashdotted), $p=1$ (solid), and $p=2$ (dashed).

24

is satisfied almost everywhere. If (nonunique) functions $\chi^1(x,y)$ and $\chi^2(x,y)$ are chosen such that their Fourier transforms satisfy

$$\sum_{m=-\infty}^{\infty} \sum_{i=1}^{2} \hat{\psi}^i(2^m\omega_x, 2^m\omega_y)\, \hat{\chi}^i(2^m\omega_x, 2^m\omega_y) = 1,$$

the function $s(x,y)$ may be reconstructed from its dyadic wavelet transform by

$$s(x,y) = \sum_{m=-\infty}^{\infty} \sum_{i=1}^{2} W_m^i s * \chi_m^i(x,y),$$

where $\chi_m^i(x,y) = 2^{-2m}\chi^i(2^{-m}x, 2^{-m}y)$.

However, when processing discrete functions the scale 2^m may no longer vary over all $m \in \mathbf{Z}$. Let the finest scale be normalized to 1 and the coarsest scale set to be 2^M. Let us, similar to [15], introduce a real smoothing function $\phi(x,y)$ such that its Fourier transform satisfies

$$|\hat{\phi}(\omega_x, \omega_y)|^2 = \sum_{m=0}^{\infty} \sum_{i=1}^{2} \hat{\psi}^i(2^m\omega_x, 2^m\omega_y)\, \hat{\chi}^i(2^m\omega_x, 2^m\omega_y). \tag{18}$$

Here, as in one dimension, a finite energy discrete function $(s(n_x, n_y) \in l^2(\mathbf{Z}^2))$ can be written as the uniform sampling of some function smoothed at scale 1: $s(n_x, n_y) = S_0 f(n_x, n_y)$, where $f(x,y) \in L^2(\mathbf{R}^2)$ is not unique, and $S_m f(x,y) = f * \phi_m(x,y)$. This led Mallat and Zhong [15] to a two-dimensional analog of the one-dimensional definition of the discrete dyadic wavelet transform:[2]

$$\left\{ S_{M-1}f(n_x + s, n_y + s), \{W_m^1 f(n_x + s, n_y + s), W_m^2 f(n_x + s, n_y + s)\}_{m \in [0, M-1]} \right\}_{(n_x, n_y) \in \mathbf{Z}^2}.$$

We will use, as in Section 2.1.2, a spline-based initialization procedure.

To implement a multidimensional discrete dyadic wavelet transform within a fast hierarchical digital filtering scheme, the wavelets were chosen to be separable products of one-dimensional functions:

$$\psi^1(x,y) = \psi(x)\,\phi(y), \tag{19}$$

$$\psi^2(x,y) = \psi(y)\,\phi(x), \tag{20}$$

where $\phi(x)$ and $\psi(x)$ were chosen as described in Section 2.1.2 (i.e., $\phi(x) = \beta_p(x)$ and $\hat{\psi}(\omega)$ specified by (7)).

---

[2] As in Section 2.1.2, we put the finest scale of the transform at $m = 0$.

Table 6: Impulse responses $t_1(n)$ for $p \in \{0, 1, 2\}$.

n	p=0	p=1	p=2
-3			0.0078125
-2		0.03125	0.046875
-1	0.125	0.125	0.1171875
0	0.75	0.6875	0.65625
1	0.125	0.125	0.1171875
2		0.03125	0.046875
3			0.0078125

From (19), (20), and (7), we may write

$$\hat{\psi}^1(\omega_x, \omega_y) = G_{-s}(\omega_x) \, \hat{\beta}_p(\omega_x) \hat{\beta}_p(\omega_y), \tag{21}$$

$$\hat{\psi}^2(\omega_x, \omega_y) = G_{-s}(\omega_y) \, \hat{\beta}_p(\omega_x) \hat{\beta}_p(\omega_y), \tag{22}$$

where $G(\omega)$ is given by (14) for $d \in \{1, 2\}$. Choosing

$$\hat{\chi}^1(\omega_x, \omega_y) = K_s(\omega_x) T_1(\omega_y) \hat{\beta}_p(\omega_x) \hat{\beta}_p(\omega_y), \tag{23}$$

$$\hat{\chi}^2(\omega_x, \omega_y) = K_s(\omega_y) T_1(\omega_x) \hat{\beta}_p(\omega_x) \hat{\beta}_p(\omega_y), \tag{24}$$

where $K(\omega)$ and $T_1(\omega)$ are digital filter frequency responses, we may compute (18) for the finest two scales by

$$\sum_{i=1}^{2} \hat{\psi}^i(2\omega_x, 2\omega_y) \, \hat{\chi}^i(2\omega_x, 2\omega_y) = |\hat{\phi}(\omega_x, \omega_y)|^2 - |\hat{\phi}(2\omega_x, 2\omega_y)|^2. \tag{25}$$

Inserting the terms defined by (21), (22), (23), (24), (6), and (10) with $\hat{\phi}(\omega_x, \omega_y) = \hat{\beta}_p(\omega_x) \hat{\beta}_p(\omega_y)$ into (25) results in

$$K(\omega_x) G(\omega_x) T_1(\omega_y) \; + \; K(\omega_y) G(\omega_y) T_1(\omega_x) \; + \; |H(\omega_x)|^2 |H(\omega_y)|^2 \; = \; 1. \tag{26}$$

Equation (26) represents the relation between the frequency responses of the digital filters used to implement a multidimensional discrete dyadic wavelet transform and is a multidimensional analog to (11).

Solving (26) for $T_1(\omega)$ by substituting $K(\omega) G(\omega)$ from (11) yields the closed formula [15]

$$T_1(\omega) = \frac{1}{2} \left(1 + |H(\omega)|^2 \right) \tag{27}$$

In Table 6, we provide the filter coefficients for $T_1(\omega)$ from (27) for $p \in \{0, 1, 2\}$. All other filters from (26) were already specified in Section 2.1.2.

As in the one-dimensional case, a two-dimensional discrete dyadic wavelet transform can be implemented as a fast hierarchical filtering scheme. To derive such an implementation, we,

similar to the one-dimensional case from Section 2.1.2, use the definition of the two-dimensional dyadic wavelet transform (17) and require $\hat{s}(\omega_x, \omega_y) = 0$ for $|\omega_x| > \pi$ or $|\omega_y| > \pi$. Using Shannon's sampling theorem in two dimensions [23], (21), (22), and $m = 0$, we get

$$W_0^1 s(x, y) = \int_{-\infty}^{\infty} \int_{-\infty}^{\infty} \sum_{i_x = -\infty}^{\infty} \sum_{i_y = -\infty}^{\infty} s(i_x, i_y) \operatorname{sinc}(t_x - i_x) \operatorname{sinc}(t_y - i_y) \cdot$$
$$\cdot \sum_{m = -\infty}^{\infty} g_{-s}(m) \beta_p(x - t_x - m) \beta_p(y - t_y) \, dt_x \, dt_y$$

and

$$W_0^2 s(x, y) = \int_{-\infty}^{\infty} \int_{-\infty}^{\infty} \sum_{i_x = -\infty}^{\infty} \sum_{i_y = -\infty}^{\infty} s(i_x, i_y) \operatorname{sinc}(t_x - i_x) \operatorname{sinc}(t_y - i_y) \cdot$$
$$\cdot \beta_p(x - t_x) \sum_{m = -\infty}^{\infty} g_{-s}(m) \beta_p(y - t_y - m) \, dt_x \, dt_y.$$

As in one dimension, we make use of the fact that the cardinal spline functions converge to the sinc function as their order r tends to infinity and write

$$\widehat{W_0^1 s}(\omega_x, \omega_y) \simeq S(\omega_x, \omega_y) B_r^{-1}(\omega_x) B_r^{-1}(\omega_y) \hat{\beta}_{p+r+1}(\omega_x) \hat{\beta}_{p+r+1}(\omega_y) \, G_{-s}(\omega_x)$$

and

$$\widehat{W_0^2 s}(\omega_x, \omega_y) \simeq S(\omega_x, \omega_y) B_r^{-1}(\omega_x) B_r^{-1}(\omega_y) \hat{\beta}_{p+r+1}(\omega_x) \hat{\beta}_{p+r+1}(\omega_y) \, G_{-s}(\omega_y),$$

or for $m \in [0, M)$ and discrete signal processing

$$\mathcal{F}\{W_m^1 s(x, y)|_{x = n_x, y = n_y}\} \simeq S(\omega_x, \omega_y) \, B_r^{-1}(\omega_x) \, B_r^{-1}(\omega_y) \, B_{p+r+1}(\omega_x) \cdot$$
$$\cdot B_{p+r+1}(\omega_y) \, G_{-s}(2^m \omega_x) \prod_{i=0}^{m-1} H_{-s}(2^i \omega_x) H_{-s}(2^i \omega_y) \tag{28}$$

and

$$\mathcal{F}\{W_m^2 s(x, y)|_{x = n_x, y = n_y}\} \simeq S(\omega_x, \omega_y) \, B_r^{-1}(\omega_x) \, B_r^{-1}(\omega_y) \, B_{p+r+1}(\omega_x) \cdot$$
$$\cdot B_{p+r+1}(\omega_y) \, G_{-s}(2^m \omega_y) \prod_{i=0}^{m-1} H_{-s}(2^i \omega_x) H_{-s}(2^i \omega_y). \tag{29}$$

Equations (28) and (29) describe the decomposition part of the filter bank implementation of a two-dimensional discrete dyadic wavelet transform. The reconstruction part can be obtained from (23)–(25) with (6) and (10). The entire filter bank implementation of the

(a)

(b)
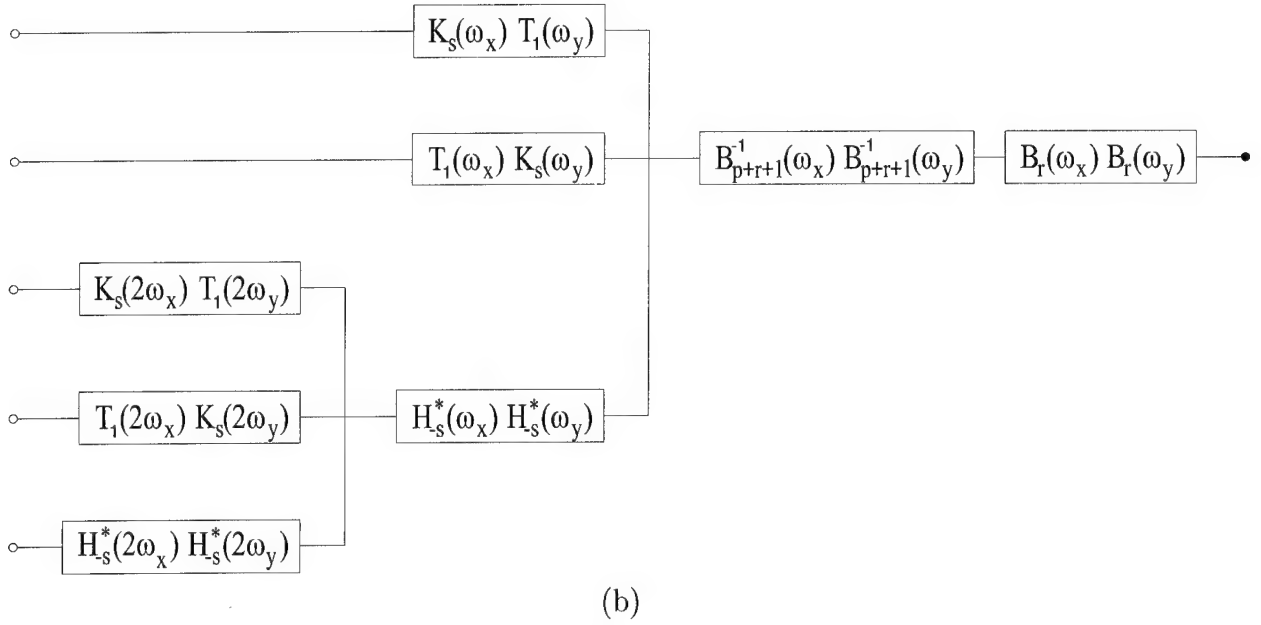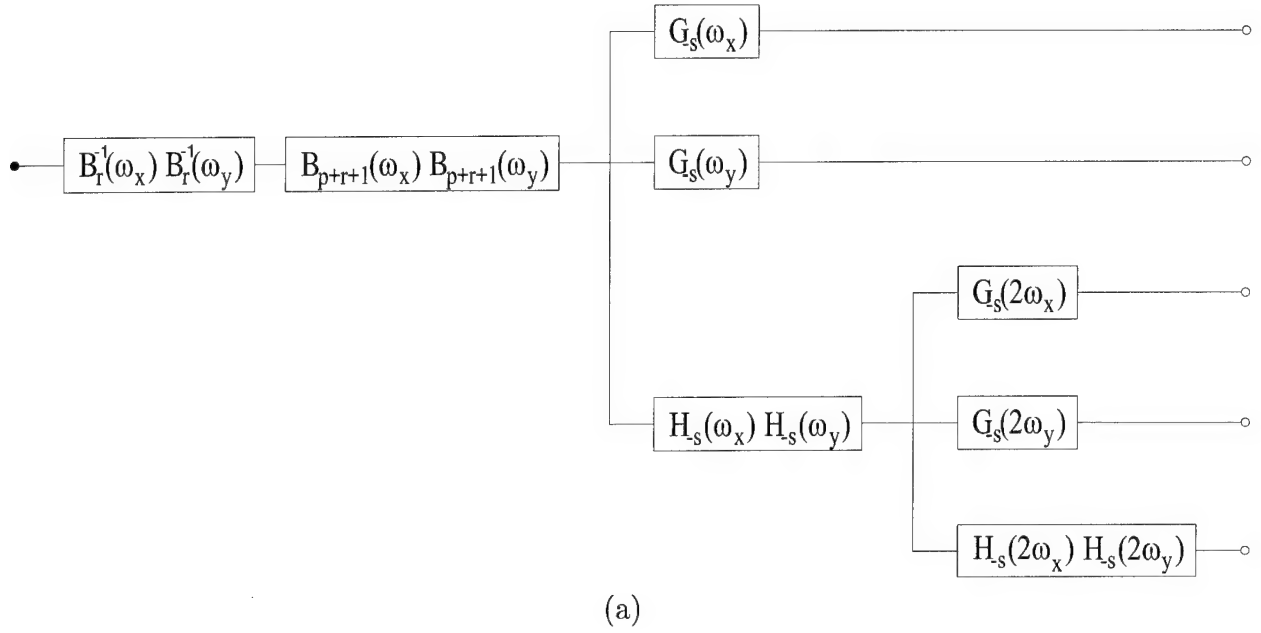
Figure 3: Filter bank implementation of a two-dimensional discrete dyadic wavelet transform (a) decomposition and (b) reconstruction for two levels of analysis. $H_{-s}^{*}(\omega)$ denotes the complex conjugate of $H_{-s}(\omega)$.

transform is shown in Figure 3. Except for the prefiltering and postfiltering, we readily recognize the implementation proposed in [15].

Using the fact that a wavelet $\psi(x)$ is equal to a d-th derivative of a spline function $\beta_{p+d}(x)$, (19) and (20) may be rewritten as

$$\psi^1(x,y) = \frac{\partial^d \vartheta^1(x,y)}{\partial x^d},$$
$$\psi^2(x,y) = \frac{\partial^d \vartheta^2(x,y)}{\partial y^d},$$

where

$$\vartheta^1(x,y) = \beta_{p+d}(x)\,\beta_p(y)$$

and

$$\vartheta^2(x,y) = \beta_p(x)\,\beta_{p+d}(y).$$

Let us denote $\vec{W}_m s(x,y) = (W_m^1 s(x,y), W_m^2 s(x,y))$, $\vec{\nabla} = (\frac{\partial}{\partial x}, \frac{\partial}{\partial y})$, $\triangle = \vec{\nabla}^2 = (\frac{\partial^2}{\partial x^2} + \frac{\partial^2}{\partial y^2})$, and assume that $\vartheta^i(x,y,)$ can be approximated by $\vartheta(x,y)$ for $i, d \in \{1,2\}$.

For $d=1$ it then follows that

$$\vec{W}_m s(x,y) = 2^m \vec{\nabla}(s * \vartheta_m)(x,y). \tag{30}$$

Thus for $d=2$ we can write

$$\sum_{i=1}^{2} W_m^i s(x,y) = 2^{2m} \triangle(s * \vartheta_m)(x,y). \tag{31}$$

With $\vartheta(x,y)$ being a Gaussian, finding local extrema of (30) in the direction of gradient $\vec{\nabla}$ corresponds to the filtering stage of a Canny edge detector [24], and finding zero-crossings of (31) corresponds to the filtering carried out with a Marr-Hildreth edge detector (Laplacian of Gaussian) [25]. (Note that both edge detectors involve postprocessing). Edge detection based on finding local extrema of $\vec{W}_m s(x,y)$ or zero-crossings of $\sum_{i=1}^{2} W_m^i s(x,y)$ is therefore an approximation to the Canny or the Marr-Hildreth edge detector over a range of dyadic scales. The differences stem from the fact that $\vartheta(x,y)$ is neither a Gaussian nor is $\vartheta^i(x,y)$ equal to $\vartheta(x,y)$.

In case of wavelets that are equal to the second derivative of a central B-splines [26, 8], the two-dimensional discrete dyadic wavelet transform decomposition is included in the multiscale spline derivative-based one from our previous report. To realize that, let us restate the filter bank implementation of the multiscale spline derivative-based transform

29
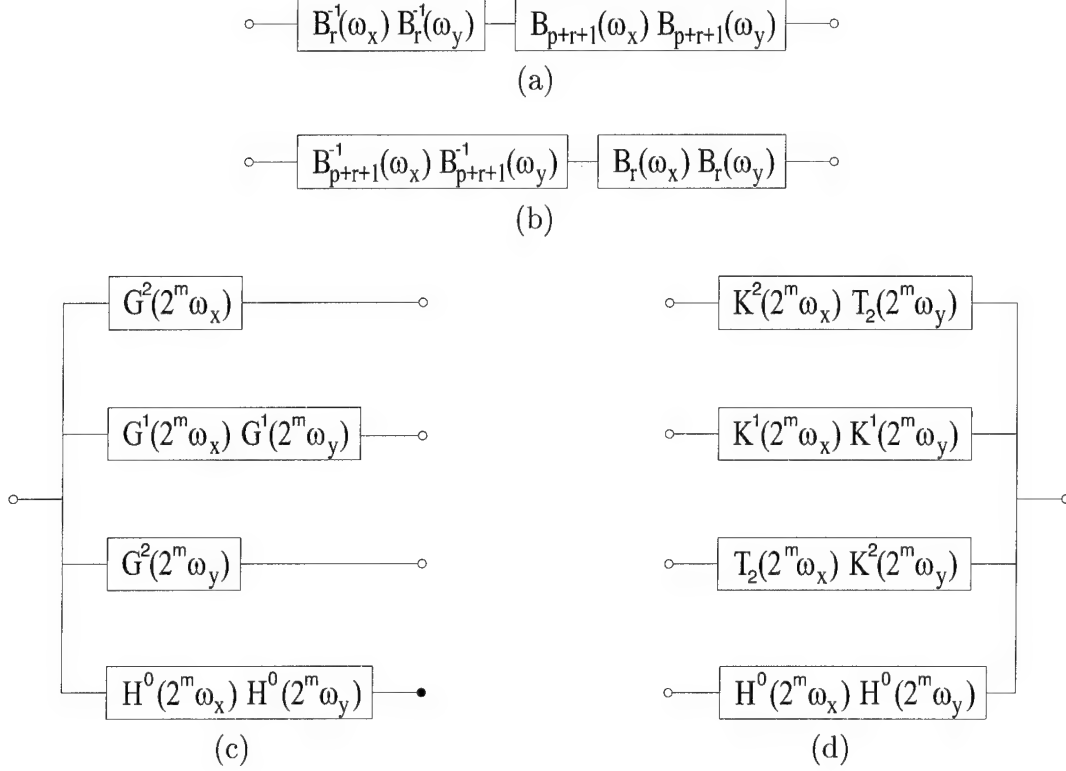
Figure 4: Filter bank implementation of a multiscale spline derivative-based transform with a second derivative wavelet for $m \in [0, M-1]$: (a) Prefiltering, (b) postfiltering, (c) decomposition and (d) reconstruction modules.

for a second derivative wavelet. Figure 4 shows the building blocks of a filter bank with filters specified as

$$
\begin{aligned}
G^d(\omega) &= e^{j\omega\left(\frac{2-d}{2}\right)} \left(2j \sin\left(\frac{\omega}{2}\right)\right)^d, \\
H^0(\omega) &= \left(\cos\left(\frac{\omega}{2}\right)\right)^{2p}, \\
T_2(\omega) &= |H^0(\omega)|^2,
\end{aligned}
\tag{32}
$$

and

$$
K^d(\omega) = \frac{1}{(2j)^d} \left(e^{-j\omega\left(\frac{2-d}{2}\right)} \sin\left(\frac{\omega}{2}\right)\right)^{2-d} \sum_{m=0}^{2p-1} \left(\cos\left(\frac{\omega}{2}\right)\right)^{2m},
$$

where $2p-1$, $p \in \mathbf{N}$, is the order of a central B-spline, and $d \in \{1, 2\}$.

Note that the decomposition from Figure 3 with $d=2$ is included in the one from Figure 4.

2.1.4 Enhancement of Mammographic Features

The goal of the method in this section is to adapt specific wavelet based enhancement schemes for distinct mammographic features, and then combine (fuse) the set of processed

30
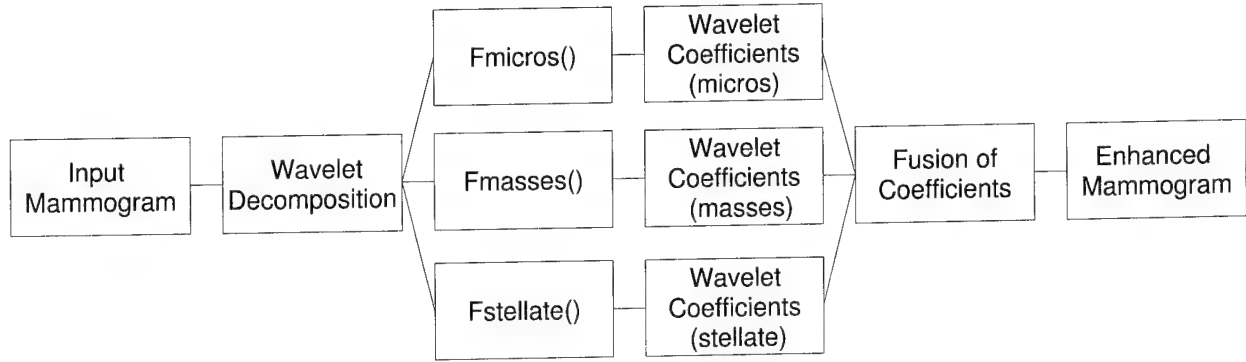
Figure 5: Overview of the algorithm.

images into an enhanced image. The mammographic image is first processed for enhancement of microcalcifications, masses, and stellate lesions. From the resulting enhanced images, the final enhanced image is synthesized by means of image fusion [27]. Figure 5 presents a block scheme of the algorithm.

Since the entire processing is carried out within the wavelet transform framework, both enhancement and fusion are implicit (i.e., performed in the wavelet domain only). The algorithm consists of two major steps: (1) wavelet coefficients are modified distinctly for each type of malignancy; (2) the obtained multiple sets of wavelet coefficients are fused into a single set from which the reconstruction is computed. The devised scheme allows efficient deployment of an enhancement strategy appropriate for clinical screening protocols: enhancement algorithm is first developed for each specific type of feature independently, and the results are then combined using an appropriate fusion strategy. (Note that it is possible to put different weights on features, and exclude certain features from the final result.)

Multiscale spline derivative-based transform with a second derivative of a central B-spline wavelet not only enables the inclusion of the two-dimensional discrete dyadic wavelet transform decomposition as seen in Section 2.1.3, but also allows for incorporation of a variety of methods [7, 8, 28, 14, 9, 11, 12].

For enhancement of microcalcifications, second derivatives along directions of x and y-axis are added to form an approximation to a Laplacian of Gaussian. The obtained coefficients are thresholded, and the original coefficients at the corresponding locations multiplied by a gain factor. Similar enhancement through detection was used by Strickland and Hahn [11, 12]. Within the multiscale spline derivative-based transform framework, it is equally easy to obtain voices at octaves "2.5" and "3.5" employed in [11, 12]: central B-spline properties enable computation of the transform at any integer scale [17].

Enhancement of circumscribed masses is carried out by applying a piecewise linear

31

enhancement function [8] to wavelet coefficients at scales 2^3 through 2^5. The selection of the scale range was based upon the pixel resolution ($116\mu m$) of digitized mammograms in the University of Florida database.

Stellate lesions are contrast enhanced according to the observation that they introduce a distortion into a radial orientation pattern from the nipple to the chest wall [28]. Approximately steerable [29] second derivative wavelets are employed in conjunction with their Hilbert transform pairs for multiscale orientation analysis. The 1-norm of differences between local orientation and average orientation within a sliding window is used as an input to a soft thresholding function at each dyadic scale independently [14].

Figure 6 demonstrates the results of processing using the multiscale analysis contrast enhancement algorithm [9], and using the proposed fusion of enhanced features method. In this example, the fusion of enhanced features emphasizes the appearance of a mass which is surrounded by dense parenchyma of the breast. Our preliminary results suggest that this type of image is more easily interpreted by radiologists compared to images produced via the global multiscale analysis contrast enhancement method [9]. Note also that the multiscale analysis based global contrast enhancement algorithm [9] can readily be incorporated into our method as one of the branches before the fusion module.

The choice of enhancement parameters controls the aggressiveness/subtleness of each resultant enhancement (i.e., the prominence of the targeted features with respect to the surrounding tissue). The structure of the algorithm is also well suited for further refinements: optimizations can be performed for each type of malignancy alone, and separately for the fusion module. The versatility of the new enhancement/fusion paradigm can provide a better viewing environment to facilitate the interpretation of mammograms.

2.1.5   Implementation Details

Finite Impulse Response Filters

Since all two-dimensional filters used in the filter bank implementations of the transforms from Section 2.1.3 are x-y separable, we will begin this section with a detailed description of FIR filter implementations for the one-dimensional discrete dyadic wavelet transform implementation from Figure 1. The extension to two dimensions will then be straightforward.

Let us refer to filters applied at scale 2^m as filters at level $m+1$, and let filters at level 1 (Equations (10), (14) through (16), (27), and (32)) be called "original filters," to distinguish them from their upsampled versions. As an input to the filter bank from Figure 1, we consider a real signal $s(n) \in l^2(\mathbf{Z})$, $n \in [0, N-1]$. Depending on the length of each filter impulse response, filtering an input signal may be computed either by multiplying the
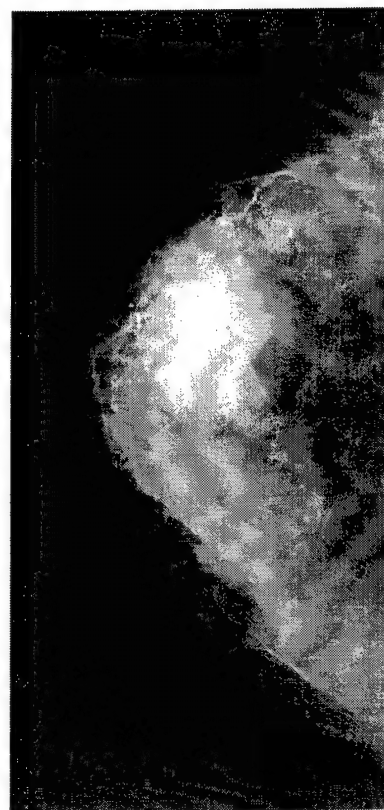
Figure 6: (a) Original mammogram. (b) Contrast enhancement by multiscale analysis [9]. (c) Enhancement obtained by fusion of enhanced features.

discrete Fourier transforms of the two sequences or by circularly convolving $s(n)$ with a filter's impulse response.[3] Of course, such a periodically extended signal may change abruptly at the boundaries causing artifacts. A common remedy for such a problem is realized by constructing a mirror extended signal [30]

$$s_{me}(n) = \begin{cases} s(-n-1) & \text{if } n \in [-N, -1] \\ s(n) & \text{if } n \in [0, N-1], \end{cases} \tag{33}$$

where we chose the signal $s_{me}(n)$ to be supported in $[-N, N-1]$. It will become evident shortly, that mirror extension is particularly elegant in conjunction with symmetric/antisymmetric filters.

Let us first classify symmetric/antisymmetric real even-length signals into four types [31]:

$$\textbf{Type I} \ \ f(n) = f(-n),$$

$$\textbf{Type II} \ \ f(n) = f(-n-1),$$

$$\textbf{Type III} \ \ f(n) = -f(-n),$$

$$\textbf{Type IV} \ \ f(n) = -f(-n-1),$$

where $n \in [-N, N-1]$. Note that for Type I signals the values at $f(0)$ and $f(-N)$ are unique, and that for Type III signals the values at $f(0)$ and $f(-N)$ are equal to zero. Using properties of the Fourier transform, it is easy to show that the convolution of symmetric/antisymmetric real signals results in a symmetric/antisymmetric real signal. If a symmetric/antisymmetric real signal has an even length, then there always exists an integer shift such that the shifted signal belongs to one of the above types.

Now, we are ready to examine the filter bank implementation of a one-dimensional discrete dyadic wavelet transform from Figure 1 with filters given by (10) and (14) through (16) driven by a mirrored signal $s_{me}(n)$ at the input. Let the number of levels M be restricted by

$$M \ \leq \ 1 + \log_2 \frac{N-1}{L_{max}-1}, \tag{34}$$

where L_{max} is the length of the longest original FIR filter impulse response.

Each FIR filter block in the filter bank consists of a filter and a circular shift operator. Equation (34) guarantees that the length of the filter impulse response does not exceed the length of the signal at any block.

Since our input signal $s_{me}(n)$ is of Type II and noninteger shifts at level 1 are rounded to the nearest integer, it follows that a processed signal at any point in the filter bank belongs

---

[3]As is customary in image processing, we use circular, rather than linear, convolution.

to one of the types defined above. This means that filtering a signal of length $2N$ can be reduced to filtering a signal of approximately one half of its length. (For Types I and III, $N + 1$ samples are needed. However, for Type III one needs to store only $N - 1$ values because zero values are always present at the zeroth and $(-N)$-th sample position). Implementation is particularly simple for FIR filters designed with d even and p odd. Filters are of Type I in this case, so the signal at any point of the filter bank will be of Type II. An FIR filter block from the filter bank shown in Figure 1 can therefore be implemented by

$$F_{s,m}u(n) = f(0)u_{II}(n) + \sum_{i=1}^{\frac{L-1}{2}} f(i)[u_{II}(n - 2^m i) + u_{II}(n + 2^m i)], \quad n \in [0, N-1], \quad (35)$$

where

$$u_{II}(n) = \begin{cases} u(-n-1) & \text{if } n \in [-\frac{N}{2}, -1] \\ u(n) & \text{if } n \in [0, N-1] \\ u(2N - n - 1) & \text{if } n \in [N, \frac{3N}{2}], \end{cases} \quad (36)$$

$u(n)$ is an input signal to a block, $f(n)$ is an impulse response of some original filter, L is the length of the filter, and N is the length of an input signal $s(n)$ to the filter bank. Implementation of filters $b_p(n)$ used for prefiltering and postfiltering represents a special case of (35) with $m=0$.

A filter bank with the above implementation of blocks and signal $s(n)$ at the input yields equivalent results as circular convolution for $s_{me}(n)$ as defined by (33). In addition to requiring one half the amount of memory, the computational savings over a circular convolution implementation of blocks are, depending on the original filter length, three to four times fewer multiplications and one half as many additions.

A similar approach can be used for other filters. However, things get slightly more complicated in this case, because the filters are not of the same type and the signal components within the filter bank are of distinct types. As a consequence, an implementation of blocks that use distinct original filters may not be the same, and the implementation of blocks at level 1 may differ from the implementation of blocks at other levels of analysis.

The decomposition blocks at level 1 can be implemented by

$$G_{-s,0}u(n) = \sum_{i=0}^{\frac{L}{2}-1} g(i)[u_{II}(n - i - 1) - u_{II}(n + i)], \quad n \in [1, N-1],$$

for d odd, (35) for d even,

$$H_{-s,0}u(n) = \sum_{i=0}^{\frac{L}{2}-1} h(i)[u_{II}(n - i - 1) + u_{II}(n + i)], \quad n \in [0, N],$$

for p even, and (35) for p odd, where $u_{II}(l)$ is defined by (36), $g(n)$ and $h(n)$ are impulse responses of the filters computed from (14) and (10), respectively, and L is the length of the corresponding impulse response.

The output from a block $G_{-s}(\omega)$ at level 1 is of Type III for d odd and of Type II for d even, while the output from $H_{-s}(\omega)$ at the same level is of Type I for p even and of Type II for p odd.

The decomposition blocks at subsequent levels $m \in [1, M-1]$ can be implemented by

$$G_{-s,m}u(n) = \sum_{i=0}^{\frac{L}{2}-1} g(i)[u_I(n - 2^m(i+s)) - u_I(n + 2^m(i+s))], \quad n \in [1, N-1],$$

for d odd and p even,

$$G_{-s,m}u(n) = \sum_{i=0}^{\frac{L}{2}-1} g(i)[u_{II}(n - 2^m(i+s)) - u_{II}(n + 2^m(i+s))], \quad n \in [0, N-1],$$

for d and p odd,

$$F_{-s,m}u(n) = f(0)u_I(n) + \sum_{i=1}^{\frac{L-1}{2}} f(i)[u_I(n - 2^m i) + u_I(n + 2^m i)], \quad n \in [0, N], \tag{37}$$

with $f(n) = g(n)$ for d and p even,

$$H_{-s,m}u(n) = \sum_{i=0}^{\frac{L}{2}-1} h(i)[u_I(n - 2^m(i+s)) + u_I(n + 2^m(i+s))], \quad n \in [0, N], \tag{38}$$

for p even, and (35) for p odd, where

$$u_I(n) = \begin{cases} u(-n) & \text{if } n \in [-\frac{N}{2}, -1] \\ u(n) & \text{if } n \in [0, N] \\ u(2N - n) & \text{if } n \in [N+1, \frac{3N}{2}]. \end{cases} \tag{39}$$

The outputs from blocks $G_{-s}(2^m\omega)$ are of Type III for d odd and p even, of Type IV for d and p odd, and of Type I for d and p even, whereas the outputs from $H_{-s}(2^m\omega)$ are of Type I for p even and of Type II for p odd.

Next, the reconstruction blocks at level 1 can be implemented by

$$K_{s,0}u(n) = \sum_{i=1}^{\frac{L}{2}} k(i)[u_{III}(n - i + 1) - u_{III}(n + i)], \quad n \in [0, N-1],$$

for d odd, (35) for d even,

$$L_{s,0}u(n) = \sum_{i=1}^{\frac{L}{2}} l(i)[u_I(n - i + 1) + u_I(n + i)], \quad n \in [0, N-1],$$

36

for p even, and (35) for p odd, where

$$u_{III}(n) = \begin{cases} -u(-n) & \text{if } n \in [-\frac{N}{2}, -1] \\ 0 & \text{if } n = 0 \\ u(n) & \text{if } n \in [1, N-1] \\ 0 & \text{if } n = N \\ -u(2N-n) & \text{if } n \in [N+1, \frac{3N}{2}], \end{cases} \tag{40}$$

$u_I(n)$ is as defined by (39) and $k(n)$ is an impulse response of the filter from (16). Note that both outputs from blocks $K_s(\omega)$ and $L_s(\omega)$ are of Type II.

The reconstruction blocks at subsequent levels can be implemented by

$$K_{s,m}u(n) = \sum_{i=0}^{\frac{L}{2}-1} k(i+1)[u_{III}(n - 2^m(i+s)) - u_{III}(n + 2^m(i+s))], \quad n \in [0, N],$$

for d odd and p even, (37) with $f(n) = k(n)$ for d and p even,

$$K_{s,m}u(n) = \sum_{i=0}^{\frac{L}{2}-1} k(i+1)[u_{IV}(n - 2^m(i+s)) - u_{IV}(n + 2^m(i+s))], \quad n \in [0, N-1],$$

for d and p odd,

$$L_{s,m}u(n) = H_{-s,m}u(n),$$

for p even, and (35) for p odd, where $u_{III}(l)$ is given by (40),

$$u_{IV}(n) = \begin{cases} -u(-n-1) & \text{if } n \in [-\frac{N}{2}, -1] \\ u(n) & \text{if } n \in [0, N-1] \\ -u(2N-n-1) & \text{if } n \in [N, \frac{3N}{2}], \end{cases}$$

and $H_{-s,m}u(n)$ is specified by (38). We observe that the outputs from blocks $K_s(2^m\omega)$ and $L_s(2^m\omega)$, $m \in [1, M-1]$, are of Type I for p even, and of Type II for p odd.

When we compare the above implementation of blocks to circular convolution driven by a mirrored signal $s_{me}(n)$ at the input, we observe that approximately twofold less memory space, three to four times fewer multiplications and one half as many additions are required. (For Type I signals an additional sample has to be saved because two values are without a pair).

Until now, we have talked only about the one-dimensional case, whose filter bank implementation is depicted in Figure 1. Two-dimensional transform filter bank implementations (Figures 3 and 4) are not only comprised of x-y separable filters solely, but also use all the filters from Section 2.1.2. Everything presented in this section so far is therefore directly applicable to the two-dimensional case. Filters which have not been

37

treated yet (i.e., $t_1(n)$, $t_2(n)$, and $b_p(n)$) can all be realized by (35) for p odd or $m = 0$ and (37) otherwise ($f(n)$ denotes an impulse response of any of the above mentioned zero-phase filters in this case).

The implementation presented in this section performs all operations in the spatial domain, however, one could also implement the structures shown in Figures 1, 3, and 4 with an input signal $s_{me}(n)$ (Equation (33)) in the frequency domain. For short filter impulse responses, such as those given in Tables 3, 4 and 5, the spatial implementation described in this section is certainly more efficient. For long filter impulse responses, however, filtering is faster if implemented in the frequency domain. Additional details on alternative implementation strategies can be found in [32].

Infinite Impulse Response Filters

Implementation of IIR filters $b_p^{-1}(n)$ which were introduced in Section 2.1.2 is a bit more involved than the one encountered in the previous section. Fortunately, the number of different cases is much smaller here: possible input to $b_p^{-1}(n)$ in filter banks from Figures 1, 3, and 4 is either of Type II or of Type I.[4] We will use ideas and a few results from [20]. Let us first take a closer look at the system function $B_p^{-1}(z)$. This function can be written as a cascade of terms

$$E(z) = \frac{1}{z - \frac{1+\alpha^2}{\alpha} + z^{-1}} = \frac{-\alpha}{(1 - \alpha z^{-1})(1 - \alpha z)}, \tag{41}$$

which can be expressed in a parallel form as

$$E(z) = \frac{-\alpha}{1 - \alpha^2} \left(\frac{1}{1 - \alpha z^{-1}} + \frac{1}{1 - \alpha z} - 1 \right), \tag{42}$$

where α and $\frac{1}{\alpha}$ are poles of the causal and the anticausal filter, respectively.

The impulse response of this term can be written as

$$e(n) = \frac{-\alpha}{1 - \alpha^2} \alpha^{|n|}.$$

We choose to implement $E(z)$ in a cascade form and therefore extract the difference equations from (41):

$$c^+(n) = u(n) + \alpha c^+(n - 1) \quad n = 1, 2, \ldots, N-1, \tag{43}$$

and

$$c(n) = \alpha \left(c(n + 1) - c^+(n) \right) \quad n = N-2, N-3, \ldots, 0, \tag{44}$$

---

[4]Note that symmetry types in this section slightly differ from those used for FIR filters: here, mirror extended signals are periodically repeated, so that they stretch from $-\infty$ to ∞.

38

where $u(n)$ denotes the input to the block, $c^+(n)$ is the output from the causal part, and $c(n)$ stands for the output from the block.

To solve (43) and (44) we need boundary conditions $c^+(0)$ and $c(N-1)$. For filters $b_p^{-1}(n)$ in filter bank implementations from Figures 1, 3, and 4, we derive

$$c^+(0) = \sum_{i=-\infty}^{0} \alpha^{-i} u_{IIp}(i) = u(0) + \sum_{i=0}^{N-1} \frac{\alpha^{i+1} + \alpha^{2N-i}}{1 - \alpha^{2N}} u(i) \simeq u(0) + \sum_{i=0}^{i_0} \alpha^{i+1} u(i), \qquad (45)$$

and, using parallel form (42)

$$c(N-1) = \frac{-\alpha}{1-\alpha^2} (c^+(N-1) + \sum_{i=0}^{N-1} \frac{\alpha^{N-i} + \alpha^{N+1+i}}{1 - \alpha^{2N}} u(i)) \simeq$$

$$\simeq \frac{-\alpha}{1-\alpha^2} (c^+(N-1) + \sum_{i=N-1-i_0}^{N-1} \alpha^{N-i} u(i)), \qquad (46)$$

where

$$u_{IIp}(n) = \begin{cases} u_{II}(n \bmod (2N)) & \text{if } n \geq 0 \\ u_{II}(-(n+1) \bmod (2N)) & \text{if } n < 0, \end{cases}$$

$$u_{II}(n) = \begin{cases} u(n) & \text{if } n \in [0, N-1] \\ u(2N - n - 1) & \text{if } n \in [N, 2N-1], \end{cases}$$

N is the length of an input signal to the filter bank, and $i_0 < N-1$ is selected such that α^{i_0} falls below a predefined precision threshold.

For orders p greater than three, we implement $B_p^{-1}(z)$ as a cascade of terms $E(z)$ with different α's. Note that the output from block $E(z)$ is always of the same type as the input to it.

2.1.6 Summary

We extended the one-dimensional discrete dyadic wavelet transform to two dimensions and showed that in case of wavelets being equal to the second derivative of a central B-spline function, the two-dimensional discrete dyadic wavelet transform decomposition is included in the multiscale spline derivative-based transform decomposition. This attests to the flexibility of the latter transform, which can incorporate a variety of wavelet based mammographic image enhancement methods.

The multiscale spline derivative-based transform was used for a novel image enhancement scheme: the input image was first processed for enhancement of specific mammographic features, and the resultant enhanced images were fused into a final result. The described

scheme represents a synthesis between our early global methods developed for an overall improvement of image quality and the local processing, targeting specific mammographic features.

The employed transform is highly redundant, and efficient implementation is of particular importance. We presented a fast filter bank implementation that takes advantage of filter and signal symmetries. Tests of our method included convincing quantitative evidence in terms of improved visibility and detection of subtle features.

2.2 Detection of Subtle Masses in Mammography via Precision Multiscale Analysis

2.2.1 Introduction

Breast cancer screening by mammography is the most effective method of detecting breast cancer in its earliest, most treatable stage. On average, mammography can detect tumors 1.7 years before a woman can feel a lump via self examination. Tumors as small as an eighth of an inch in diameter can be seen with mammograms while the smallest masses detectable by manual exams are about half an inch across. Early detection is crucial since survival rate has a roughly inverse relationship with the stage of breast cancer at detection, i.e., the more advanced the cancer stage, the lower the survival rate.

Currently, these often dense and complex mammographic images are examined by radiologists as a screening modality. However, this is a tedious and time-consuming process since only one in a thousand images will show features that are of possible concern. Today 10 to 30% percent of all breast cancers are missed with mammography, as currently practiced. We suggest scale-space search algorithms combined with the emerging generation of digital detector technology will go a long way toward reducing false negatives in mammography screening.

Wavelet algorithms have found widespread use in detection applications such as mass detection in mammograms [33, 34, 35, 36, 37]. Wavelet methods are preferred over traditional Fourier analysis because the local nature of wavelets allows an efficient representation of transients by a small number of components. Traditional Fourier transient representations, on the other hand, require a much larger number coefficients in order to prevent sharp discontinuities in the spatial domain from causing ripple artifacts in the frequency domain. Though transients are typically considered to be a phenomena that occurs in time, we can use transient formulation to represent tumors as spatial transients in two-dimensional mammograms. Recent studies have shown that indeed mammographic features are well represented by wavelet coefficients [9, 38].

In wavelet detection theory, Daubechies first pointed out that the wavelet detector should lie in the same spatial neighborhood and in the same frequency band as the feature to be detected [39]. Therefore, it can be argued that the dyadic wavelet transform may not be appropriate for applications where subtle detection is required. That is, sampling the scale space by fixed powers of two may not provide a dense enough sampling such that the wavelet detector lies in the same frequency band defined by the feature. In fact, in this paper we show that the dyadic transforms can fail in mammography applications. In the same spirit, Marco proposed to use an M-band wavelet detector to obtain a denser sampling

of scale space [35]. In this paper, we describe a novel translation-invariant, continuous-scale wavelet detector, with distinct advantages in terms of automated feature detection. Previous continuous wavelet algorithms include Rioul's [32] and Unser's methods [40, 41]. In Rioul's algorithm, Q new mother wavelets ψ^q are defined as $\psi^q(x) \approx 2^{-q/Q}\psi(2^{-q/Q}x)$, where $q = 0, ..., Q-1$ and $\psi^q(x) = \sum_n h^q[n]\phi(x-n)$ in each octave. An octave-by-octave algorithm is applied to compute "Q voices per octave" of multiscale analysis. More recently, Unser developed a fast algorithm to compute the wavelet coefficients for Q voices within each octave, with $O(N)$ complexity per voice. However, since each voice corresponds to similar but distinct mother wavelets, it is not straightforward to map this decomposition to a detection algorithm. In terms of wavelet detector theory, we must search the scale space to somehow find the best scale for a signal. Optimization criterion is complicated by the fact that any change in scale might require a change in the mother wavelet. In this paper, we describe an algorithm to calculate the wavelet coefficients for the same mother wavelet. In our method, a continuous scale wavelet detector is incorporated into a Constant False-Alarm Rate (CFAR) detector to improve performance. A CFAR detector utilizes the statistics of a target and its background to separate the target from its background and is widely used in Automatic Target Recognition applications [42]. We show that such a detector is able to effectively separate a mass from its complex background using the respective statistics of each region.

This chapter is organized as follows. In section 2, we derive a arbitrary scale discrete wavelet decomposition algorithm. Next, in section 3, we describe a arbitrary scale wavelet CFAR detector. In section 4, we show that the best scale to detect a tumor is related to the size of each distinct tumor. Then we show the results of applying our algorithm to difficult mammography cases of breast cancer. The ability to find and process features at an arbitrary scale is shown to have significant advantages over standard dyadic algorithms. Finally, in section 5, we summarize our results.

2.2.2 A Continuous Scale Discrete Wavelet Transform

A wavelet transform is a linear operation that projects a signal onto a set of basis functions, which are dilated versions of a mother wavelet. The mother wavelet is a function $\psi \in L^2$ that satisfies $\int_{-\infty}^{\infty} \frac{|\Psi(\omega)|^2}{|\omega|} d\omega < +\infty$. This requires that the wavelet has sufficient decay, and that $\int_{-\infty}^{\infty} \psi(x)dx = 0$. The continuous wavelet transform of a function at scale a and shifting parameter b is defined as

$$\mathbf{W}f(a,b) = \int_{-\infty}^{\infty} f(x)\psi\left(\frac{b-x}{a}\right) dx.$$

42
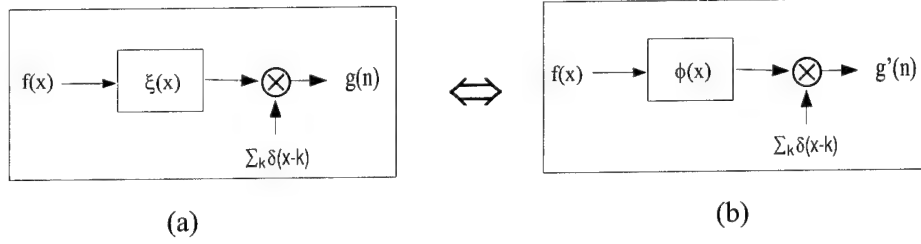
Figure 7: Data acquisition and initial condition: (a) Block diagram of digitization—a continuous signal f(x) is sampled after a low-pass operation, (b) initial condition for subsequent wavelet decomposition.

Of course, it has been shown that a wavelet transform satisfies energy conservation and can be perfectly reconstructed from its wavelet transform coefficients [16, 43]. The Arbitrary Scale Discrete Wavelet Transform (ASDWT) is defined as the CWT sampled along the shifting parameter b,

$$\mathbf{W}f(a,n) = \int_{-\infty}^{\infty} f(x)\psi\left(\frac{n-x}{a}\right) dx. \tag{47}$$

In practice, data is spatially sampled and quantized. Furthermore, we assume that a signal $f(x)$ is sampled at its Nyquist rate f_s so that it may be recovered from its discrete samples. Since $f(x)$ is band-limited, $\mathbf{W}f(a,b)$ is also band-limited, and can be recovered from its samples $\mathbf{W}f(a,n)$.

Scaling Space

The finite resolution of the sampled signal g[n] puts a limit on the finest scale that can be computed. Let us now introduce a compactly supported scaling function $\phi(x)$ that satisfies the following conditions [40] :

1. Riesz basis condition: $A \leq \sum_{k \in \mathcal{Z}} |\Phi(\omega + 2k\pi)|^2 \leq B$, where A and B are strictly positive constants;

2. Order property: $\Phi(0) = 1, \Phi^{(m)}(2k\pi) = 0, k \in \mathcal{Z}, k \neq 0$, for $m = 0, ..., N-1$;

3. Two-scale relation: $\phi\left(\frac{x}{2}\right) = \sum_{k \in \mathcal{Z}} h[k]\phi(x-k)$;

4. Frequency property: $\Phi(\omega) \neq 0$, for $|\omega| \leq \pi$, and $\Phi(\omega)$ should be very small for $|\omega| > \pi$.

Constraint 1 implies that $\phi(x-k)$ is a Riesz basis of the subspace V_ϕ defined by

$$\mathbf{V}_\phi = \{f(x) = \sum_{k \in \mathcal{Z}} c[k]\phi(x-k) \qquad c \in \mathbf{l}_2\} \qquad \text{for } f(x) \in \mathbf{V}_\phi$$

43

and that V_ϕ is a well defined (closed) subspace of $\mathcal{L}_2$ [44]. Property 2 implies that $\phi(x)$ reproduces all polynomials of degree N-1 [45]. Constraint 3 is the well-known two-scale relation. Condition 4 shows that $\phi(x)$ can be an anti-aliasing filter.

Initial Condition

In the traditional DWT analysis literature, it is generally assumed that

$$g[n] = \int_{-\infty}^{\infty} f(x)\phi(n-x)dx. \tag{48}$$

However, in practice, $g[n]$ is the output of a physical acquisition device shown schematically in Fig 7 (a). The impulse response of an acquisition device is $\xi(x)$, where $\xi(x)$ is typically a lowpass filter. The approximation of $\xi(x)$ in V_ϕ space is

$$\xi(x) \approx \tilde{\xi}(x) = \sum_k r[k]\phi(x-k), \tag{49}$$

where r[k] is the projection of $\xi(x)$ onto the scaling space. Let $g'[n] = \int_{-\infty}^{\infty} f(x)\phi(n-x)dx$. The relation between $g'[n]$ and $g[n]$ is

$$
\begin{aligned}
g[n] &= \int_{-\infty}^{\infty} f(x)\xi(n-x)dx \\
&\approx \int_{-\infty}^{\infty} f(x)(\sum_k r[k]\phi(n-x-k))dx \\
&= \sum_k r[k](\int_{-\infty}^{\infty} f(x)\phi(n-x-k)dx) \\
&= \sum_k r[k]g'[k],
\end{aligned} \tag{50}
$$

Therefore, $g'[n]$ satisfies the traditional initial condition and can be calculated from $g[n]$ by

$$g'[n] = \sum_k g[k]r^{-1}(n-k). \tag{51}$$

It is commonly assumed that $\xi(x)$ is an ideal lowpass filter. An ideal lowpass filter may be approximated as a cardinal spline filter [46]. For example, the scaling function is a spline of order $n-1$,

$$\xi(x) \approx \sum_k (b^n)^{-1}[k]\beta(x-k). \tag{52}$$

Therefore, $r^{-1}[k] = b^n[k]$. Notice that Equation (51) is similar to projecting a signal onto a scale space as described in [40] [41], although the theoretical justification for our case is quite different.

ASDWT

A discrete approximation of $f(x)$ at scale a is defined as

$$\mathbf{S}_a^d f[n] = \int_{-\infty}^{\infty} f(x)\phi\left(\frac{n-x}{a}\right)dx. \tag{53}$$

It can be shown from the two-scale relation and Equation (53) that

$$\mathcal{F}\{\mathbf{S}_{2^{j+1}}^d f[n]\} = H(2^j\omega)\mathcal{F}\{\mathbf{S}_{2^j}^d f[n]\}. \tag{54}$$

From the initial condition, $\mathbf{S}_1 f[n] = g'[n]$, where $a = 1$ is the finest scale of analysis. As a increases, $\mathbf{S}_a f[n]$ becomes a coarser representation of $f(x)$. When a goes to infinity, $\mathbf{S}_a f[n]$ approaches a constant equal to the average value of $f(x)$. In practice, the length of $g[n]$ defines the coarsest scale.

When $\Phi(\omega) \neq 0$ for $\omega \in [-\pi, \pi]$, it is straightforward to show that there is one and only one $f(x)$ such that

$$g^c(x) = f(x) * \phi(x). \tag{55}$$

Theorem 1 *Given $g[n]$, for $a > s_0$, if $\tilde{\Psi}_a(\omega)$ is band-limited between $[-\pi, \pi]$, the ASDWT can be calculated by*

$$\mathbf{W}_a f(a, n) = \sum_{k \in \mathcal{Z}} p(a, k)g(n-k), \tag{56}$$

where

$$P^c(a, \omega) = \frac{\tilde{\Psi}_a(\omega)}{\Phi(\omega)} \tag{57}$$

and

$$P^c(a, \omega) = \int_{-\infty}^{\infty} p^c(a, x)e^{-j\omega f_s x}dx.$$

Proof: Note that $\tilde{\psi}_a(x)$ and $p^c(a, x)$ are band-limited at $[-\pi, \pi]$. And $p(a, n) = p^c(a, x)|_{x=n}$. From Equation (57),

$$\tilde{\Psi}_a(\omega) = P^c(a, \omega)\Phi(\omega) \tag{58}$$

$$\tilde{\psi}_a(x) = \int_{-\infty}^{\infty} p^c(a, u)\phi(x-u)du. \tag{59}$$

45

If we substitute Equation (59) into the previous ASDWT definition (Equation (47)), we obtain

$$
\begin{aligned}
\mathbf{W}_a f(a, n) &= \int_{-\infty}^{\infty} f(x) \tilde{\psi}_a(n - x) dx \\
&= \int_{-\infty}^{\infty} f(x) \int_{-\infty}^{\infty} p^c(a, u) \phi(n - x - u) du dx \\
&= \int_{-\infty}^{\infty} (\int_{-\infty}^{\infty} f(x) \phi(n - x - u) dx) p^c(a, u) du \\
&= \int_{-\infty}^{\infty} g^c(n - u) p^c(a, u) du.
\end{aligned} \tag{60}
$$

Since $g^c(x)$ and $p^c(a, x)$ are band-limited to $[-\pi, \pi]$, we need to show that

$$
\int_{-\infty}^{\infty} g^c(n - u) p^c(a, u) du = \sum_{k \in \mathcal{Z}} p(a, k) g(n - k). \tag{61}
$$

A transform to the frequency domain gives

$$
\mathcal{F}\{\int_{-\infty}^{\infty} g^c(n - u) p^c(a, u) du\} = (G^c(\omega) P^c(a, \omega)) * 2\pi \delta_{2\pi}(\omega).
$$

Since $g^c(x)$ and $p^c(a, x)$ are band-limited to $[-\pi, \pi]$,

$$
\begin{aligned}
\mathcal{F} \quad &\{\int_{-\infty}^{\infty} g^c(n - u) p^c(a, u) du\} \\
&= (G^c(\omega) * 2\pi \delta_{2\pi}(\omega))(P^c(a, \omega) * 2\pi \delta_{2\pi}(\omega)) \\
&= G(\omega) P(a, \omega).
\end{aligned}
$$

Therefore, we can claim that Equation (61) is indeed true. Substituting Equation (61) into Equation (60), we obtain

$$
\mathbf{W}_a f(a, n) = \sum_{k \in \mathcal{Z}} p(a, k) g(n - k).
$$

∎

Based on Theorem 1, $p(a, k)$ can be calculated by sampling $\mathbf{IFFT}\left\{\frac{\tilde{\Psi}_a(\omega)}{\Phi(\omega)}\right\}$ as long as $\tilde{\Psi}_a(\omega)$ is band-limited between $[-\pi, \pi]$. Once $p(a, k)$ is available, the sample of CWT of a signal can be calculated[32].

Note that the mother wavelet must be band-limited so that we can obtain wavelet coefficients by discrete wavelet transform using the same mother wavelet. Note that a wavelet $\psi(x)$ is not required to be compact in the frequency domain. However, if $\Psi(\omega)$ is local, then we can select an s_0 such that $\tilde{\Psi}_{s_0}(\omega) = \Psi_{s_0}(\omega) Rect(\omega)$ has an acceptable

approximation error onto the scaling space. The approximation error is defined as the ratio of the energy of $\Psi(a\omega)$ outside $[-\pi, \pi]$ to the total energy. The ratio decreases as s_0 increases.

Next we show that our $\tilde{\psi}_{s_0}(x)$ is also a mother wavelet. Since $\psi(x)$ satisfies the "admissibility condition,"

$$\int_{-\infty}^{\infty} |\omega|^{-1}|\Psi(\omega)|^2 d\omega < \infty.$$

Substituting ω with $s_0\omega$ and multiplying both side of the equation with $Rect(\omega)$, we have

$$\begin{aligned}
\int_{-\pi}^{\pi} |\omega|^{-1}|\Psi(s_0\omega)|^2 d\omega &< \infty \\
\int_{-\infty}^{\infty} |\omega|^{-1}|\tilde{\Psi}(s_0\omega)|^2 d\omega &< \infty.
\end{aligned} \tag{62}$$

Therefore, $\tilde{\psi}_{s_0}(x)$ satisfies the "admissibility condition." Wavelet coefficients at arbitrary scale $a = ss_0$ can be calculated directly from Equation (56).

When little is known about the best scale to detect a certain feature, it is desirable to first search the scale space at a coarse discretization (perhaps dyadically) before carrying out a finer search. Once an s_0 is selected, it may be considered as a "voice" and $P(2^L s_0, \omega)$ can be calculated as [32]

$$P(2^L s_0, \omega) = P(s_0, 2^L \omega)(\prod_{k=0}^{L-1} H(2^k \omega)). \tag{63}$$

Thus, Eq(54), (56) and (63) yield

$$\mathcal{F}\{\mathbf{W}_{2^j s_0} f\} = P(s_0, 2^j \omega)\mathcal{F}\{\mathbf{S}_{2^j} f\}. \tag{64}$$

In this study, the wavelet is a second derivative of a spline of order 5 (n=4, d=2). The scaling function and mother wavelet are given by

$$\Phi(\omega) = \left(\frac{sin\left(\frac{\omega}{2}\right)}{\frac{\omega}{2}}\right)^n, \quad \Psi(\omega) = (j\omega)^d \left(\frac{sin\left(\frac{\omega}{4}\right)}{\frac{\omega}{4}}\right)^{n+d}.$$

and

$$H(\omega) = e^{jx_0\omega} cos^n\left(\frac{\omega}{2}\right), \quad P(s_0, \omega) = e^{jx_1\omega}\frac{j^d 2^{n+2d}}{s_0^n}\frac{sin^{n+d}\left(\frac{s_0\omega}{4}\right)}{sin^n\left(\frac{\omega}{2}\right)}.$$

$x_0 = \frac{1}{2}$ when n is odd and level $L = 0$. Otherwise, $x_0 = 0$. $x_1 = \frac{1}{2}$ when d is odd and level $L = 0$, and $x_1 = 0$.

In next section, we will apply this ASDWT in tumor detection in difficult mammography cases of breast cancer.

2.2.3 A CFAR Wavelet Detector

In this section, we first describe a novel continuous scale wavelet detector. Then we introduce the CFAR detection theory and show that our wavelet detector is also a CFAR detector under certain assumptions. Later, we show the results of applying our algorithm to difficult mammography cases of breast cancer. The ability to find and process features at an arbitrary scale is shown to have significant advantages over standard dyadic algorithms. Finally, we summarize our results.

Wavelet Transient Detector

We pose mass detection in mammograms as a transient signal detection problem. Let's consider hypotheses of the form

$$H_0 : \quad y(x) = n(x),$$
$$H_1 : \quad y(x) = f(x) + n(x).$$

Where x is the location, $y(x)$ is the observed signal, $f(x)$ is the underlying signal to be detected, and $n(x)$ is additive noise. Based on the observation y, it must be decided whether the tumor is present (H_1) or not (H_0).

We assume that a signal $f(x)$ is essentially spatial-localized and band-limited [5] (to spatial-frequency area $[x_{f_1}, x_{f_2}] \times \{[-\omega_{f_2}, -\omega_{f_1}] \cup [\omega_{f_1}, \omega_{f_2}]\}$), as shown in Figure8. Then we project $f(x)$ onto a wavelet basis at scale s_i:

$$W_{s_i} f(b) = \int f(x) \psi_{s_i}(b - x) dx. \tag{65}$$

The advantage of applying the wavelet representation to this detection problem is a result of the well known fact that there are only a few significantly-different-from-zero wavelet coefficients for an essentially spatial-localized and band-limited signal [39]. The spatial-frequency area of a wavelet ψ_{s_i} is shown in Figure 8. As scale s changes, the spatial-frequency area of ψ_s moves vertically. As the shifting parameter b in Equation (65) changes, the spatial-frequency area of ψ_s shifts horizontally. When the spatial-frequency area of $\psi_s(b - x)$ overlaps with that of $f(x)$, wavelet coefficients $W_s f(b)$ may be significantly different from zero. Note that when we project the observed signal $y(x)$ on wavelet base ψ_{s_i}, we filter out the noise that lies outside the passband of ψ_{s_i} and increase the SNR. Therefore, we can consider the process of decomposing an observed signal $y(x)$ onto the best scale s_i as projecting that signal onto a basis to maximize the SNR.

---

[5] We want to detect a mass whose size is in a certain range. In later discussion, we show that the size of a mass is corresponding to a certain scale[frequency]. Therefore, it is reasonable to assume a profile of a mass is spatial-localized and band-limited.
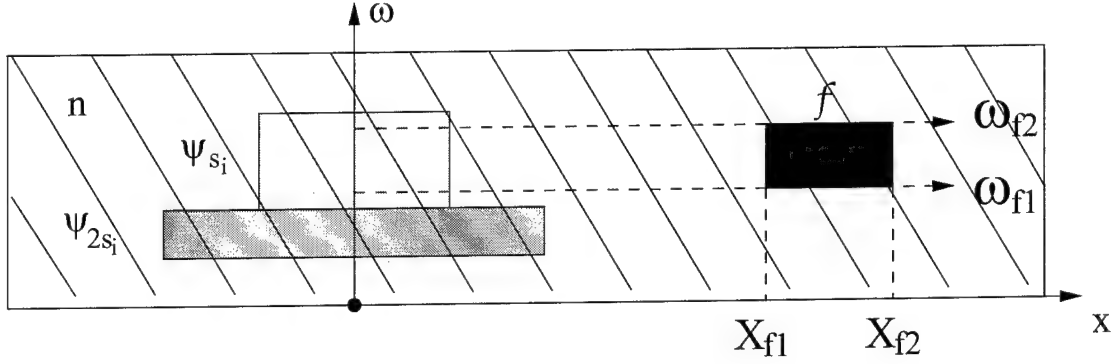
Figure 8: Spatial-frequency plane for f, n and ψ_s.

Mallat has experimentally found that the wavelet coefficients can be modeled with a two-parameter generalized Laplacian distribution [47]:

$$\mathbf{p}(u) = Ce^{(-|u|/\alpha)^\beta}, \tag{66}$$

where the constant C is adjusted in order to have $\int_{-\infty}^{+\infty} \mathbf{p}(u)\,du = 1$. The coefficients α and β are directly related to the first and second moment of the wavelet coefficients, defined as

$$m_1 = \int_{-\infty}^{+\infty} |u|\mathbf{p}(u)\,du \ \text{ and } \ m_2 = \int_{-\infty}^{+\infty} u^2\mathbf{p}(u)\,du.$$

We can compute α and β using

$$\beta = \mathbf{f}^{-1}\left(\frac{m_1^2}{m_2}\right),$$

$$\alpha = \frac{m_2\Gamma(1/\beta)}{\Gamma(3/\beta)},$$

where

$$\mathbf{f}(x) = \frac{\Gamma(2/x)^2}{\Gamma(3/x)\Gamma(1/x)},$$

$$\Gamma(x) = \int_0^\infty u^{x-1}e^{-u}\,du.$$

Therefore, the *pdf* of wavelet coefficients under hypothesis H_0 is $\mathbf{p}_0(u) = C_0 e^{(-|u|/\alpha_0)^{\beta_0}}$. The *pdf* of wavelet coefficients under hypothesis H_1 is $\mathbf{p}_1(u) = C_1 e^{(-|u-m|/\alpha_1)^{\beta_1}}$, and $m = \mathbf{MAX}(W_{s_i}f)$. The "Likelihood Ratio Test" (LRT) becomes

$$\Lambda(u) = log(\mathbf{p}_0(u)) - log(\mathbf{p}_1(u)) \lessgtr_{H_0}^{H_1} \lambda. \tag{67}$$

49

Figure 9: Probability density functions under hypotheses H_0 and H_1.

As in Figure 9, when $\Lambda(u) < \lambda$, $u \in R_0$ and $u < T$. When $\Lambda(u) > \lambda$, $u \in R_1$ and $u > T$. Note that no matter where we set the threshold T, we will occasionally make a wrong decision. When H_0 is true and we choose H_1, we call it "error of the first kind." Its probability Q_0 is

$$Q_0 = \int_T^\infty \mathbf{p}_0(u)\,du,$$

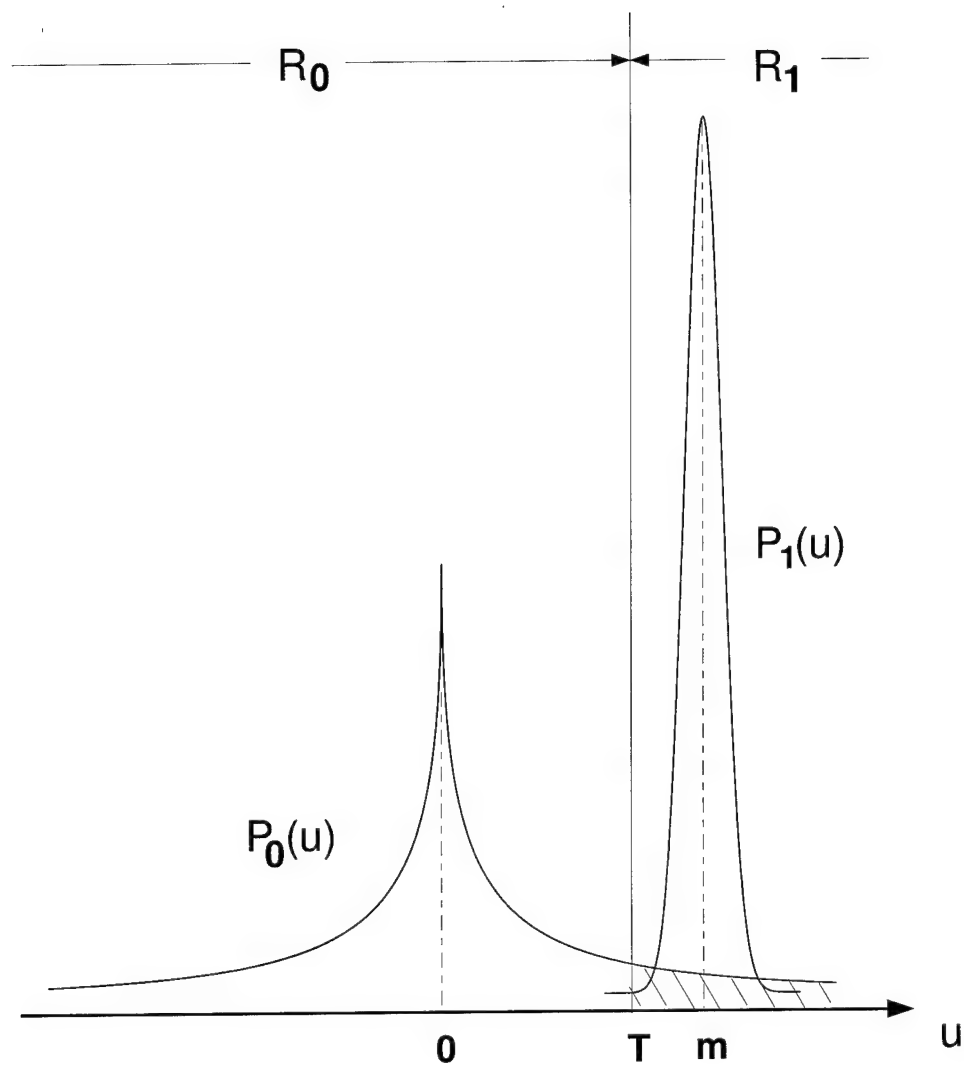it is represented by the area under the curve of $\mathbf{p}_0$ to the right of T (the shadowed area in Figure 9). We also call it a "False alarm." On the other hand, we might choose H_0 when H_1 is true. That is an "error of the second kind." Its probability Q_1 is

$$Q_1 = \int_{-\infty}^T \mathbf{p}_1(u)\,du.$$

Of course, the value of T depends on how much these mistakes cost. It also depends on the prior probability of H_1. For example, if we know that the family of a woman has a history of breast cancer, she is at high risk of getting breast cancer and we should lower the detection threshold T.

After the hypothesis testing, we can utilize the geometric information to further eliminate false alarms. Our ASDWT detector consists of the following procedures:

1. Find the best scale by systematically searching the scale space, from coarse to fine. (The definition of "best scale" is given later.)

2. Choose the maximum ASDWT coefficients from the best scale.

3. Eliminate the wavelet maxima which are less than some threshold. The value of the threshold is determined by the desired false alarm rate.

4. If local curvature analysis of the remaining targets indicates a symmetric bump, the center of the bump is considered to be the site of a potential mass (see discussion below).

Each pixel that is larger than a threshold (determined by the false alarm rate) is a candidate target. Local curvature analysis seeks to verify that each candidate target is a symmetric bump with a single local maximum. Asymmetric bumps are artifacts due to edge effects or extended linear features in the dense tissue. The characteristic star patterns in the figures are created using a simple algorithm that compares each pixel with it neighboring pixels and decides if the pixel is a local maximum in any direction.
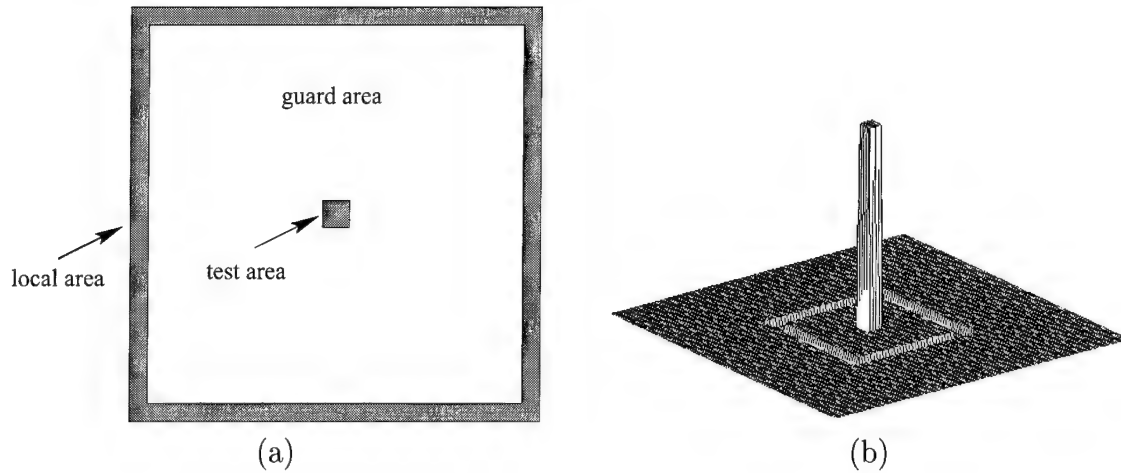
Figure 10: A conventional CFAR detector: (a) Standard interior and exterior regions, (b) 3-D plot of the equivalent filter.

A CFAR Detector

In detection theory, when the prior probabilities of the two hypotheses H_1 and H_2 and the costs associated with each type of error are known, a threshold T should be chosen to minimize the average risk by using the "Bayes criterion." If the prior probabilities are unknown, the "minimax criterion" should be used to select the threshold T. When not only the prior probabilities but also the costs are difficult to estimate, one should select an acceptable false alarm rate and try to maximize the detection rate. That is the "Neyman-Pearson criterion." Goldstein proposed a automatic detection procedure which maintained a Constant False-Alarm Rate (CFAR) [48]. He showed that the false-alarm rate depended on a detection threshold and the number of data used to estimate statistic parameter. Based on a clutter distribution assumption and test statistic theory, he provided a procedure to adjust the detection threshold adaptively in order to keep the false alarm rate constant.

The CFAR detection algorithm is widely used in military Automatic Target Recognition (ATR) applications. A one-parameter CFAR detector is a cell-averaging detector controls the detection threshold for a specific cell (pixel) based on the estimation of a sufficient statistic of the clutter [42]. It works well under the assumption that the background noise is statistically homogeneous. During hypothesis testing, a test pixel x_t is set to be the center of test region R_t. The mean of test region R_t is calculated. Then the clutter (background) intensity mean is estimated in a local region R_c distantly surrounding pixel x_t, which is shown in Figure 10 (a). Their difference is compared to a threshold T_{CFAR} to determine

whether pixel x_t is a target. This one-parameter CFAR detection can be formulated as

$$y = \frac{1}{N_t} \sum_{(i,j) \in R_t} x(i,j) - \frac{1}{N_c} \sum_{(i,j) \in R_c} x(i,j)$$

And

$$y \underset{non-target}{\overset{target}{\lessgtr}} T_{CFAR},$$

where $x(i,j)$ is the intensity of pixel at location (i,j), N_t and N_c are the number of pixels in region R_t and R_c. Note that only the mean information is utilized in this one-parameter CFAR detector. In order to drop the homogeneous requirement, we can adapt a threshold to a local environment. A two-parameter CFAR detector utilizes both first and second order statistics in hypothesis testing, and is given by

$$\mu_c = \frac{1}{N_c} \sum_{(i,j) \in R_c} x(i,j),$$

$$\sigma_c = \sqrt{\frac{1}{N_c - 1} \sum_{(i,j) \in R_c} (x(i,j) - \mu_c)^2},$$

$$y = x_t - \mu_c,$$

$$y \underset{non-target}{\overset{target}{\lessgtr}} \sigma_c T_{CFAR}.$$

From a signal processing perspective, outputs y of a CFAR detector can be obtained by filtering the image with a kernel shown in Figure 10 (b). The abrupt changes in this kernel will cause undesirable ripples outside its main lobe in the frequency domain. We propose to use a wavelet which is a second derivative of a spline of order 5 (n=4, d=2). As shown in Figure 11, this ASDWT detector is a weighted CFAR detector. When calculating the statistics of the test area, the pixels in the center of the testing area are weighed more heavily. While estimating the statistic of the surrounding area, pixels both near the test area and far away from the test area are weighed less heavily. While the shape of our operator resembles the classical center surround operators, it should be remembered that image statistics are gathered in the positive and negative valued regions independently. Therefore, the proposed detector combines a wavelet formulation with the classical theory of CFAR detectors.

Next, we will apply our wavelet CFAR detector for mammographic tumor detection.
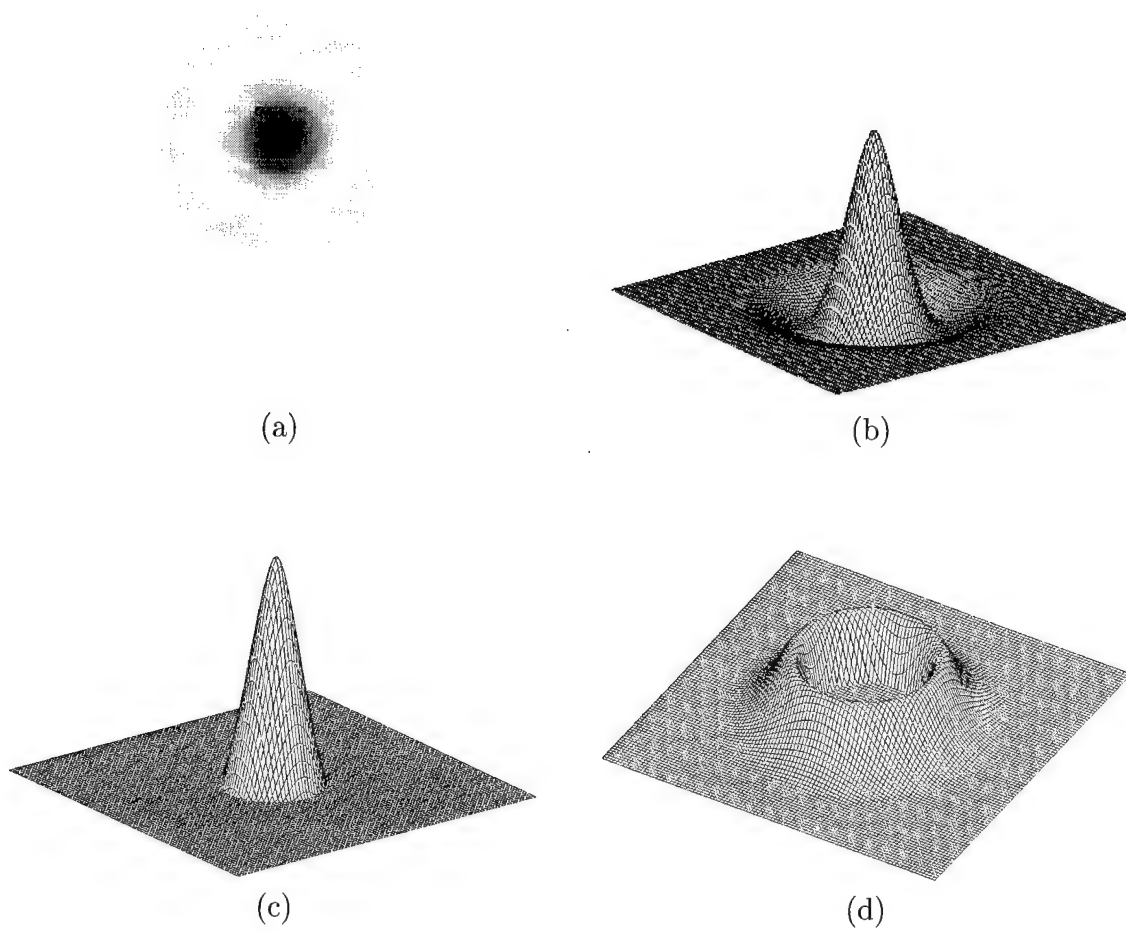
(a)

(b)

(c)

(d)

Figure 11: An ASDWT CFAR detector: (a) Interior and exterior regions, (b) 3D plot of the equivalent filter, (c) the weighted test region, (d) the weighted surrounding neighborhood.

Results of Mammographic CFAR Detector

In this section, we use a digital radiograph of a phantom to demonstrate that continuous scale is necessary. We show that our *pdf* assumption is reasonable. And we apply our detector to actual mammograms obtained from Shands Hospital in Gainesville, FL.

X-ray images of an RMI model 156 phantom (Radiation Measurements Inc., Middleton, WI) were investigated. The RMI phantom contains five masses and six fibrils which mimic two objects of interest in mammography. The radiographic image quality of this phantom, as well as the total number of objects which are deemed to be visible, form a key component of the mammography accreditation program administered by the American College of Radiology (ACR). The RMI phantom is designed so that at least one object (i.e. smallest mass) in each category is not visible, and one object is at the borderline of the visibility threshold [49].

Radiographic images of the RMI phantom were obtained using a Digital Spot Mammography (DSM) system attached to a Lorad Breast Biopsy System (Lorad Corporation, Danbury, CT). Due to the limit of the detector area, only regions containing masses at the right-lower corner were captured (with technique factors of 22 kVp and 16 mAs) as shown in Figure 12(a). The smallest mass in the schematic representation of the insert of the phantom (Figure 12(e)) can not be seen using conventional window and leveling at 12-bit contrast resolution.

First, a wavelet detector at scale 64 was applied. A threshold was chosen such that there are no false alarms. As shown in Figure 12 (c), both the largest mass and the medium-size mass were detected while the smallest mass was missed. Then we reduced the scale of the detector to scale 46.4 and found that all the masses were detected with zero false alarms as shown in Figure 12 (e). When the scale is set to a dyadic power 32, we cannot detect the smallest mass without a false alarm as shown in Figure 12 (f). What is more, the detector cannot even detect the center of the largest mass correctly. When we look at the wavelet coefficients shown in Figure 12 (c), (d) and (e), the smallest mass can be seen at scale 46.4 and is clearly less evident at scale 32 and 64. Since the dyadic wavelet detector failed to detect all masses without false alarms, a more arbitrary and flexible scale of analysis is necessary.

The non-dyadic scale 46.4 in the above paragraph was found by using an estimated range of mass sizes to bracket a search for an effective scale. An effective scale provides the characteristic star pattern in the output. We will further discuss the optimal scale search in next chapter.

Having proved the case using phantoms, we now apply our detector to some real mammograms with dense tissue obtained from Shands Hospital in Gainesville, FL. In this
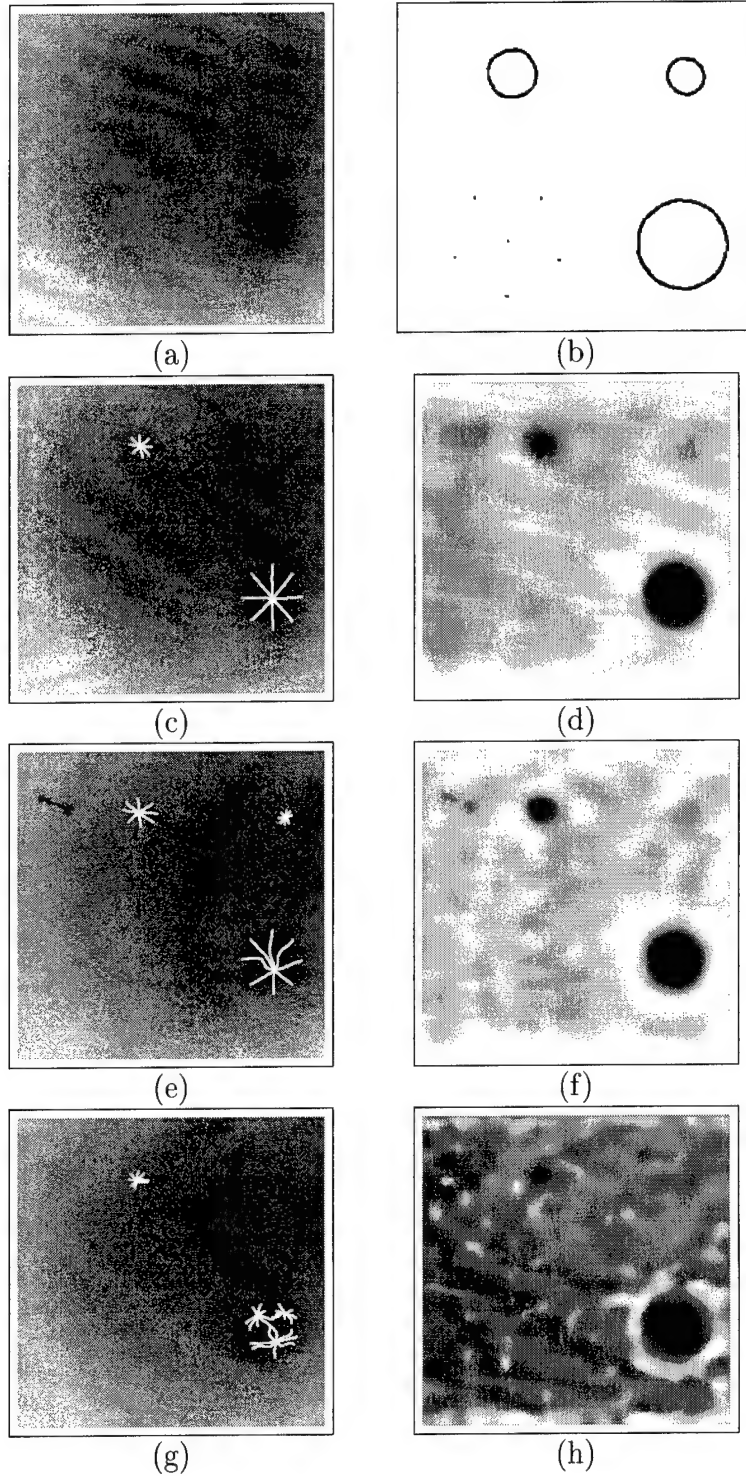
Figure 12: Continuous scale is important. (a) Digital radiograph of the RMI156 phantom. (b) Schematic representation of mammographic features within the phantom. (c) Detector output obtained at scale 64, super-imposed on the phantom image. (d) Wavelet coefficients at scale 64. (e) Detector output obtained at scale 46.4. (f) Wavelet coefficients at scale 46.4. (g) Detector output obtained at scale 32. (h) Wavelet coefficients at scale 32.

56

Case	Shape	Margins	Density	Size	Biopsy	Difficulty
lcc046	Irregular	Indistinct	High	10mm	Malignancy	Mod. Difficult
lml015	Round	Obscured	High	15mm	Malignancy	Difficult
lcc002	Irregular	Spiculated	High	10mm	Malignancy	Difficult
lcc004	Irregular	Spiculated	High	15mm	Malignancy	Difficult

Table 7: Description of mammograms.

preliminary study, we tested our algorithm using cases that a mammography expert regarded as likely to be missed by radiologists. These mammograms contain lesions of varying density as described in Table 7. In figure 13, we show histograms of wavelet representations of mammographic background in case lcc0046 and lml015 and histograms of the corresponding tumor wavelet representations . All those histograms are exponentially decay as what we assume. Because we have a limited number of pixels, the histograms are noisy. In Figure 14, 15, 16 and 17, we show some initial results. All masses (biopsy proven) were correctly detected. The star patterns in each figure are added by the local curvature analysis discussed earlier. All symmetric star pattern indicate possible masses that turned out to be actual masses as verified by biopsy procedures.

In the next section, we will discuss how to select the best scale for tumor detection.

2.2.4   Best Scale Selection

In this section, we describe a method to find the optimal scale to segment a potential mass from its background, using a continuous multiscale analysis. First, a suspicious object is identified, which may or may not contain a lesion. Next, we search the scale space to find the scale at which the contrast of the object is maximum. Finally we will apply this scheme to some real mammograms.

In the next subsection, we will discuss how to identify 1-D image objects.

Relationships between Scale and Objects

Singularities and irregular structure often carry the most important information about an object. For example, the discontinuities in the intensity provide the locations of the object contours, which are particularly meaningful for recognition purposes. The local regularity of images can be characterized by wavelet representations. In this section, we will first introduce the Lipschitz exponents, which is a measure of the local regularity in mathematics. Then we will review the Lipschitz exponents and their characterization with the wavelet transform. Finally, we will explain how to locate an object to find the best scale to detect that object.
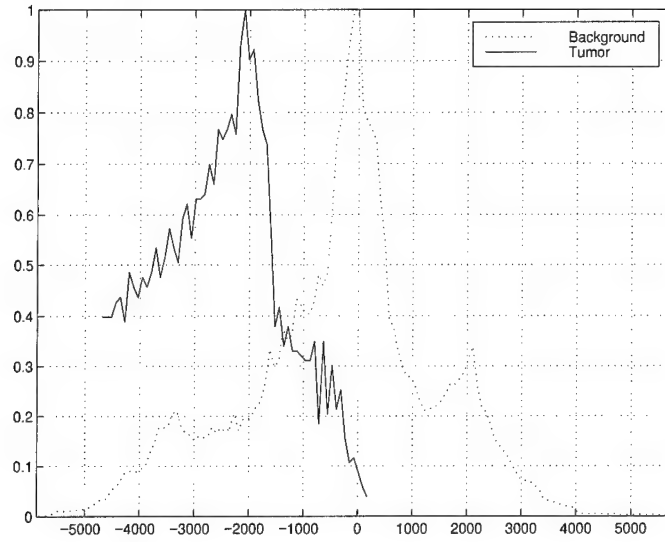
(a)
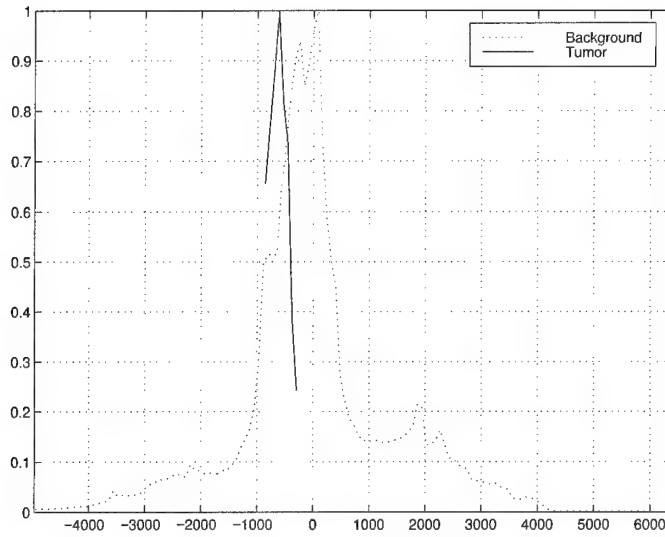
(b)

Figure 13: Normalized histograms of tumor wavelet representation (dotted line) and mammographic background wavelet representation (solid line). (a) Mammogram case lcc046. (b) Mammogram case lml015.

(a)

(b)

(c)

Figure 14: Detection result: (a) Mammogram case lcc046, (b) the maxima of outputs of the wavelet CFAR detector, (c) mass enhanced by window and leveling.

Figure 15: Detection result: (a) Mammogram case lcc004, (b) the maxima of outputs of the wavelet CFAR detector, (c) mass enhanced by window and leveling.

Figure 16: Detection result: (a) Mammogram case lml015, (b) the maxima of outputs of the wavelet CFAR detector, (c) mass enhanced by window and leveling.
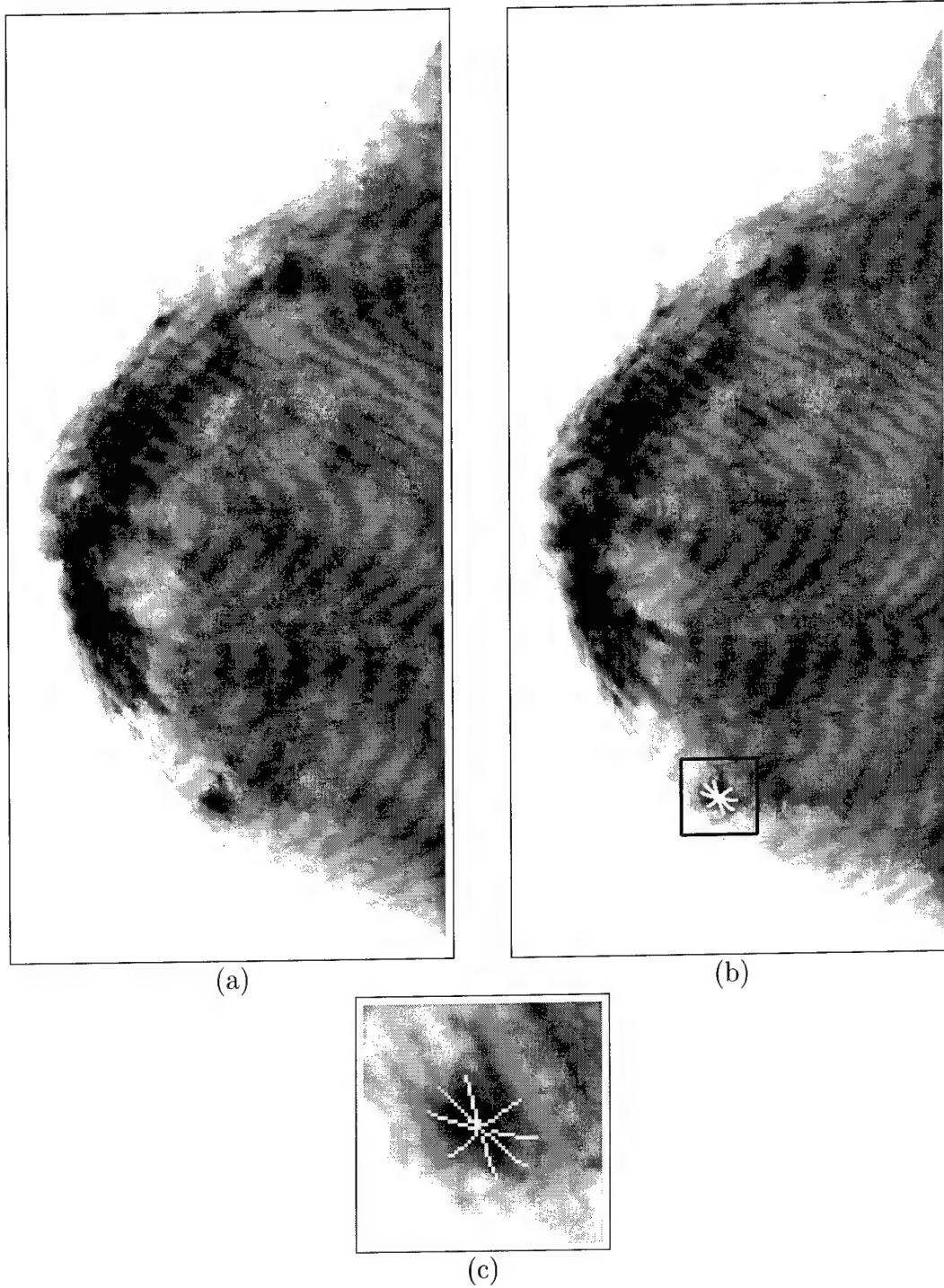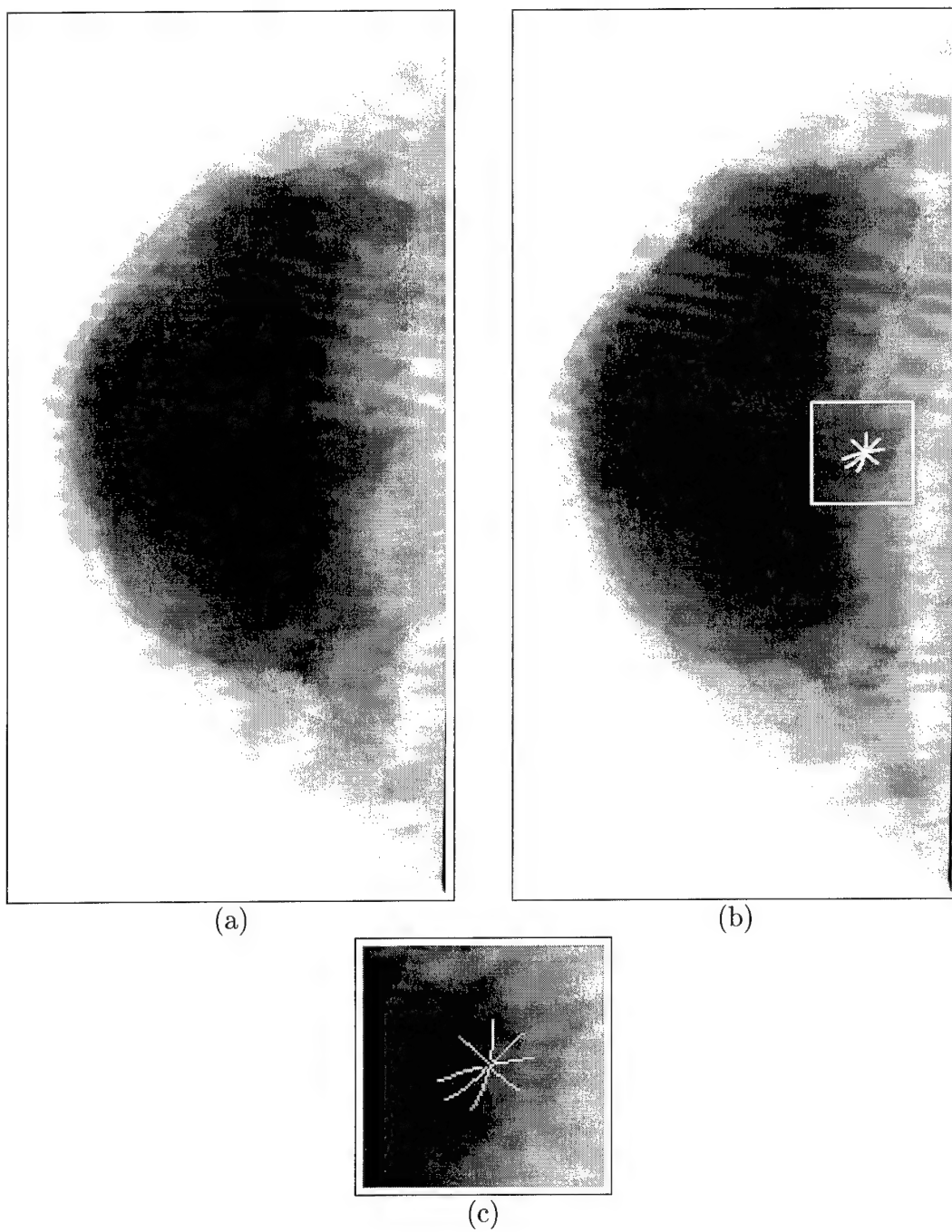
Figure 17: Detection result: (a) Mammogram case lcc002, (b) the maxima of outputs of the wavelet CFAR detector, (c) mass enhanced by window and leveling.
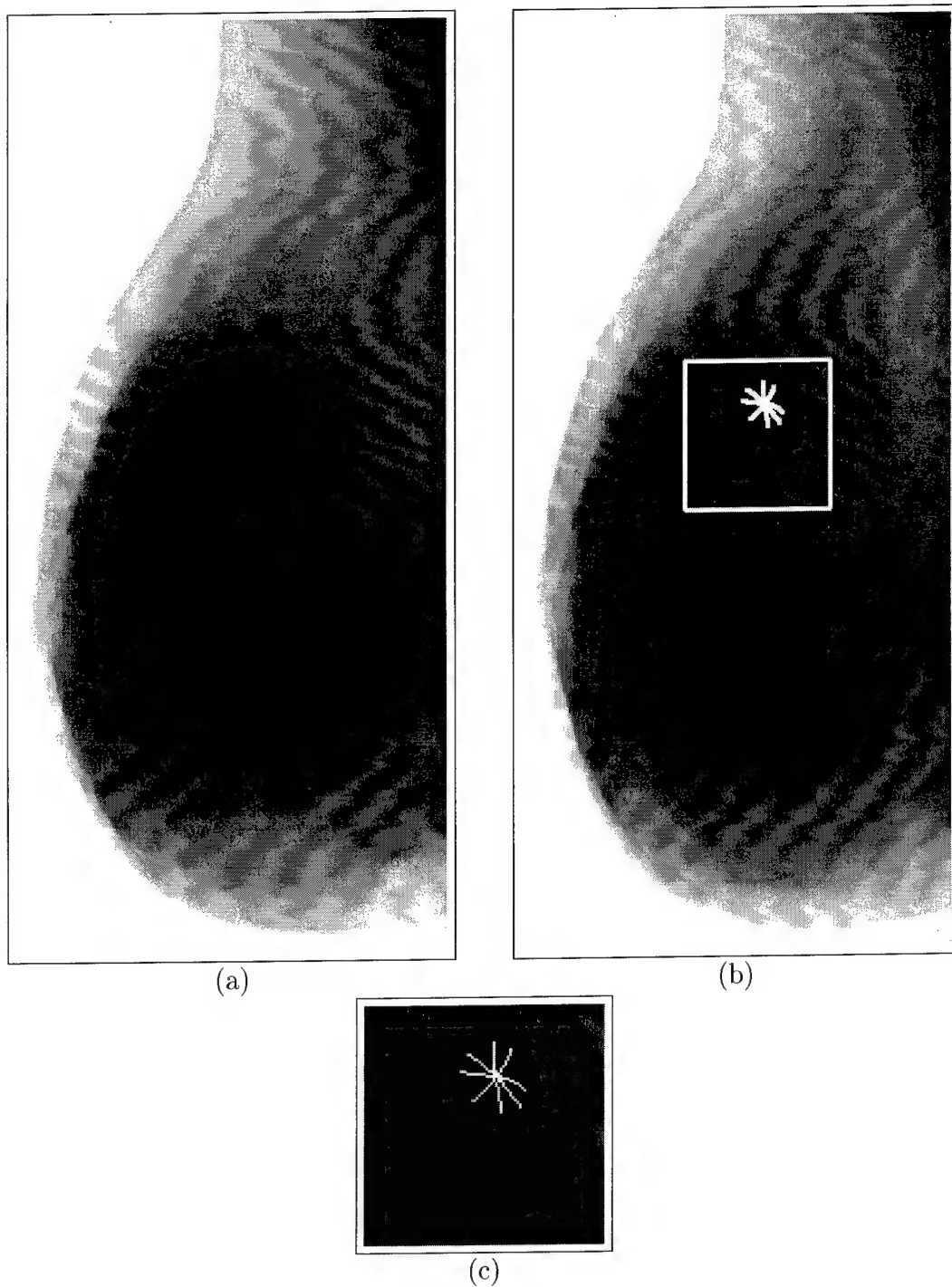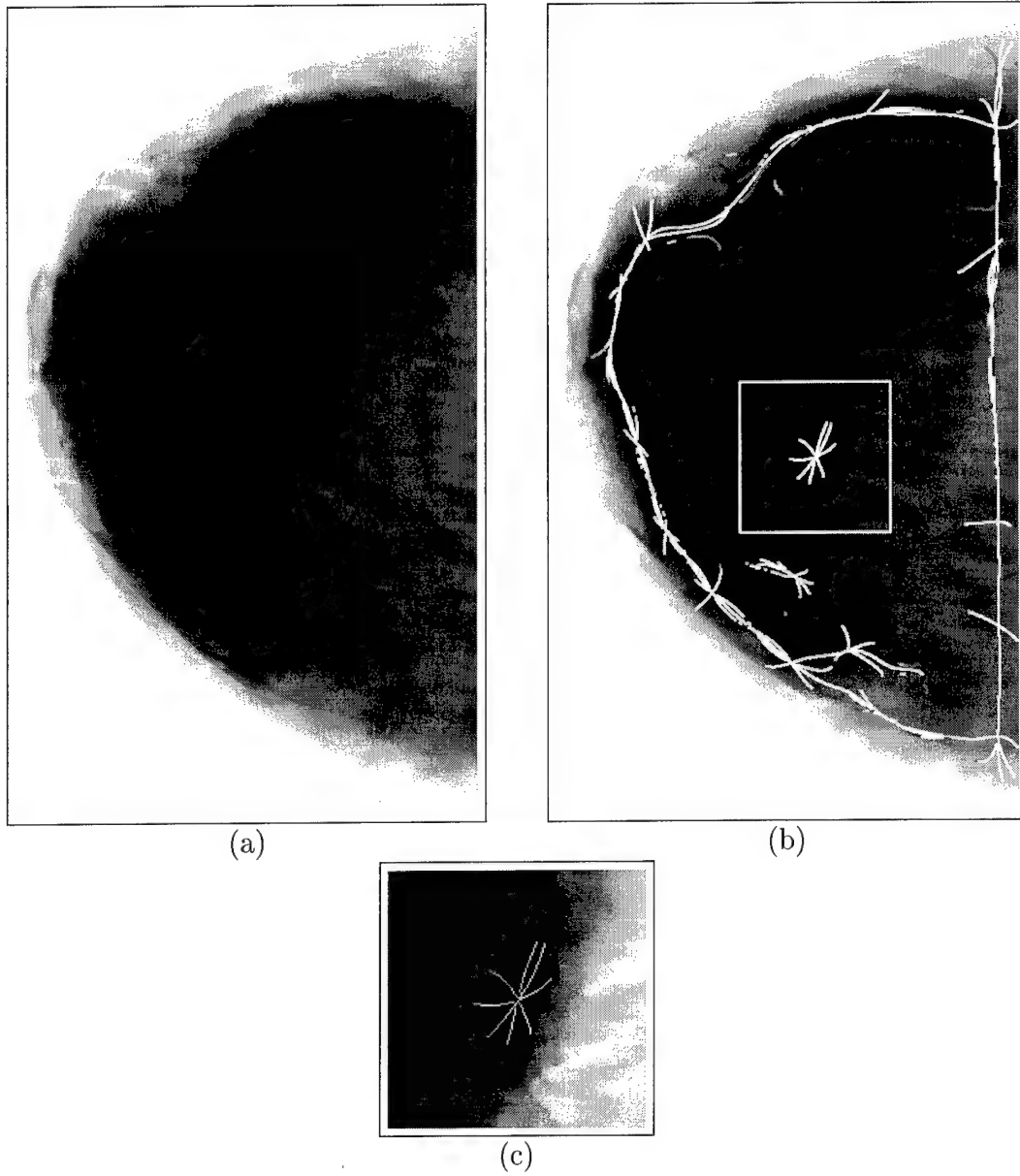
In mathematics. the local regularity is often measured with Lipschitz exponents, which is defined as [50, 15]:

- Let n be a positive integer and $n \leq \alpha \leq n+1$. A function $f(x)$ is said to be Lipschitz α, at x_0, if and only if there exists two constants K and h_0, and a polynomial of order n, $p_n(x)$, such that for $h < h_0$

$$|f(x_0 + h) - P_n(h)| \leq K|h|^\alpha.$$

- Let $0 \leq \alpha \leq 1$. A function $f(x)$ is uniformly Lipschitz α over an interval $]a,b[$ if and only if there exists a constant K such that for any $(x_0, x_1) \in]a, b[^2$

$$|f(x_0) - f(x_1)| \leq K|x_0 - x_1|^\alpha.$$

- We call Lipschitz regularity of $f(x)$ and x_0, the superior bound of all values α such that $f(x)$ is Lipschitz α at x_0.

- We say the a function is singular at x_0, if it is not Lipschitz 1 at x_0.

If $f(x)$ is discontinuous but bounded in the neighborhood of x_0, its uniform Lipschitz $\alpha = 1$. If $f(x)$ is differentiable at x_0, then it is Lipschitz $\alpha = 1$. The larger uniform Lipschitz α is, the more "regular" $f(x)$ at x_0 is. We can measure the Lipschitz exponents from the evolution across scales of the absolute value of the wavelet transform. We suppose a wavelet $\psi(x)$ is continuously differentiable and decays asymptotically as $O(\frac{1}{1+x^2})$. Let $0 < \alpha < 1$. A function is uniformly Lipschitz α over $]a, b[$, the wavelet transform satisfies [50]:

$$log_2|\mathbf{W}_a f(x)| \leq log_2(K) + \alpha log_2(s). \tag{68}$$

Note that a discrete signal is of finite resolution, which we normalize to 1. We cannot compute the wavelet transform at scales smaller than 1. Therefore, if the uniform Lipschitz regularity is positive, Equation 68 implies that the amplitude of the wavelet transform modulus maxima should increase when the scale increase.

We can define the negative Lipschitz exponents for tempered distribution as [50, 15]: *A tempered distribution is uniformly Lipschitz α on $]a, b[$ if and only if its primitive is uniformly Lipschitz $\alpha + 1$ on $]a, b[$.*

For example, the primitive of a Dirac function $\delta(x - x_0)$ is a function which is a step edge at x_0. This step edge is uniformly Lipschitz $\alpha = 0$ in the neighborhood x_0. Hence, a Dirac is thus equal to -1 in the neighborhood of x_0 and its wavelet maxima should decrease as
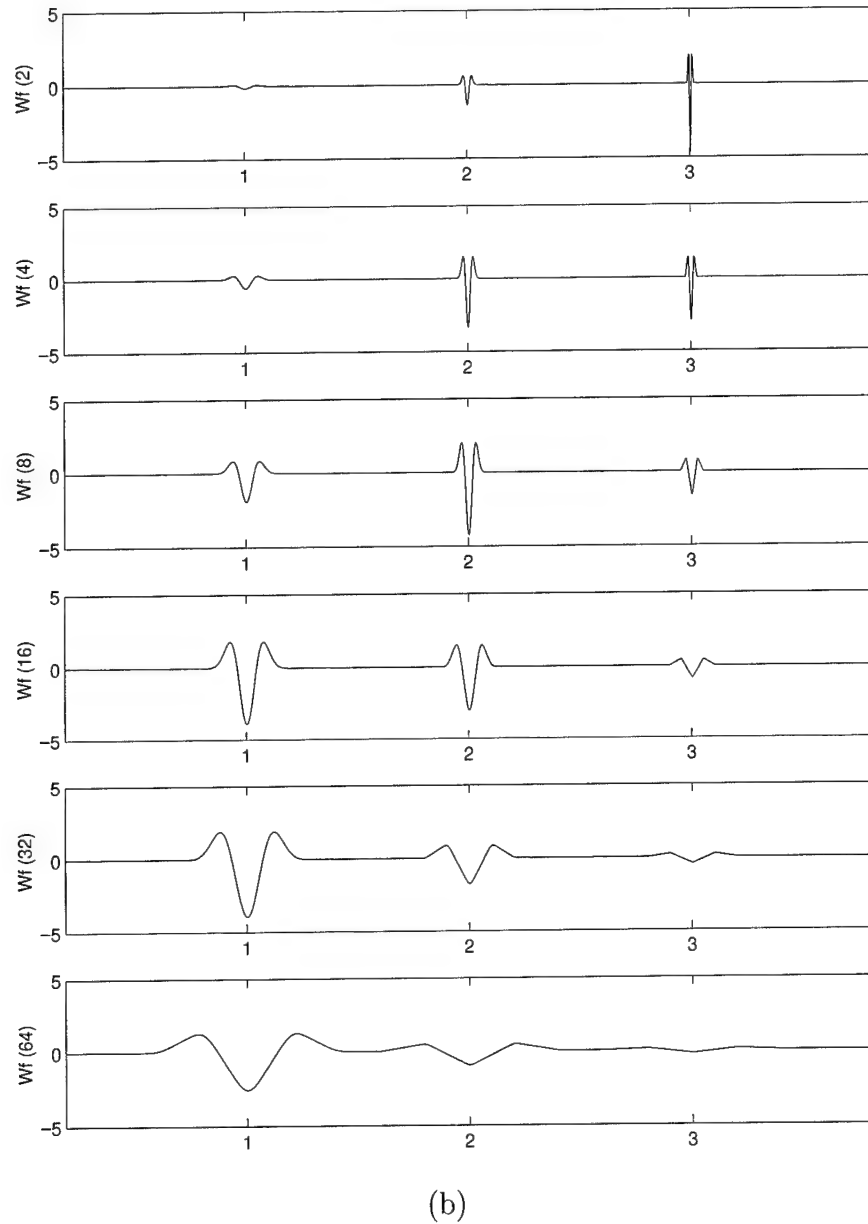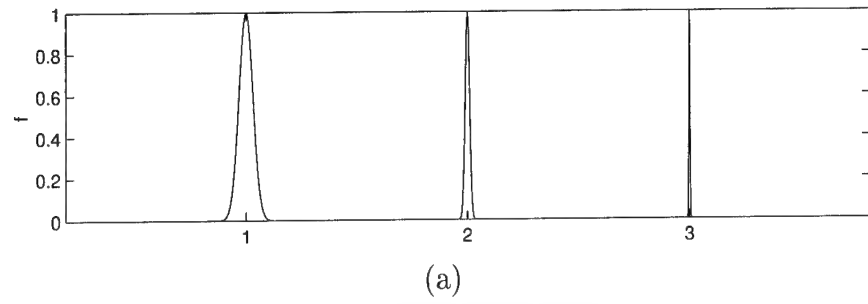
63

Figure 18: An example showing the behavior of wavelet maxima across scales: (a) Three objects with different size (Gaussian bumps with variances 1600, 20, and 1, respectively), (b) the wavelet maxima across scales depends on the size of objects.

the scale increase. This can indeed be verified in Figure 18. Figure 18 (a) shows 3 Gaussian bumps with different variance σ^2, respectively, 1600,20,1. We projected these images on to a second derivative of a cubic spline wavelet at scales 2, 4, 8, 16, 32 and 64. The result is shown in Figure 18 (b). The object at abscissa 3 produces wavelet transform maxima at decrease as the scale increases. Its distribution is locally equal to a Dirac. The wavelet transform maxima of the object at abscissa 2 first increases then decreases as the scale increases. We know that as the scale increases, the size of the neighborhood also increases. When the neighborhood increases to a certain size, the regularity changes. Therefore, the wavelet transform maxima begin to decrease. Therefore, the local maximum across scale is associated with the boundary of an object, while the local maximum across the shifting parameter indicates the location of an object.

The relationship between local maximum across scale and the boundary of an object is further demonstrated in Figure 19. The left-hand side of Figure 19(a) shows three image profiles, containing synthetic bumps of distinct width. We calculated the wavelet transform for each image. At each scale, the maximum of wavelet coefficients across the shifting parameter was found. The relation between scale and the wavelet maximum is shown on the right-hand side of Figure 19(a). Note that there is exactly one scale a^* corresponding to the maximum of wavelet coefficients across both shifting and scale parameters. The value a^* is clearly a function of the size of the feature within the cropped region.

Scale Search for Tumor Detection

In this section, we define a normalized contrast and propose a scheme to find the local maximum of the normalized contrast across scale.

In the previous discussion, we argued that the local maximum across scale is associated with the size of an object, while the local maximum across shifting parameter indicate the location of an object. Since we are targeting tumors of a certain size, we know a priori, the expected range of sizes. We consider the neighborhood of a wavelet transform maxima as a Region Of Interest (ROI). Since our CFAR wavelet detector utilizes the difference between the test region and its surrounding, we would like to maximize the difference between the ROI and its background per unit distance. For a 1-D image, let x_i be a wavelet transform maximum. The normalized contrast is defined as

$$\bar{C} = \frac{1}{2} \left(\mathbf{max}_{j \in (i, \infty)} \left(\frac{x_i - x_j}{j - i} \right) + \mathbf{max}_{j \in (-\infty, i)} \left(\frac{x_i - x_j}{i - j} \right) \right).$$

The normalized contrast for a 2-D image is an average of 8 directional maximal gradients. We would like test this index with a mathematic phantom shown in Figure 20 (a). In Figure 21 (b), we show that the normalized contrast first increases then decreases, and the
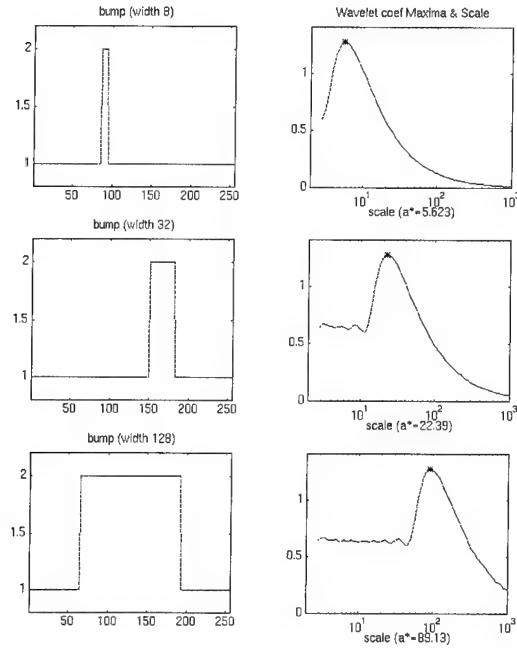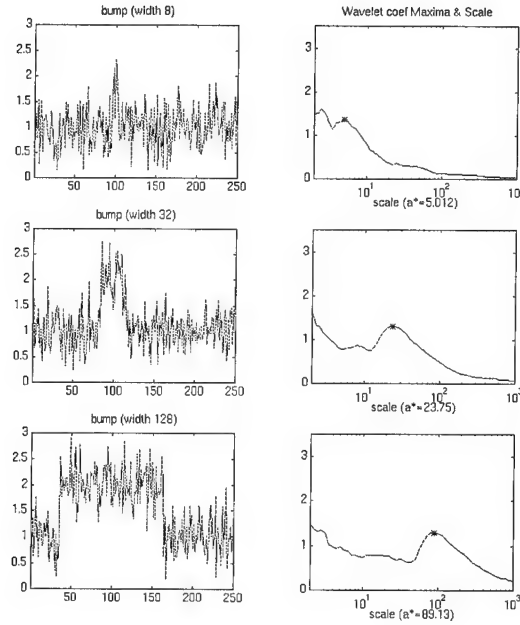
Figure 19: Best scale selection. (a) Left: 1-D pulses of different widths are shown. Right: the maximum of wavelet maxima across scale can be used to determine the width of the pulse. (b) The results in (a) are duplicated with a large amount of simulation noise.

66
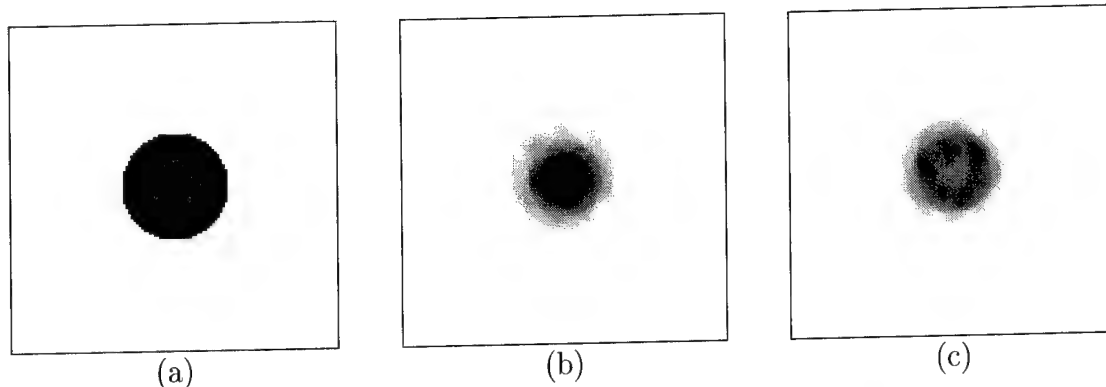
Figure 20: Best scale selection: (a) The ideal phantom, (b) wavelet coefficients at the best scale (34.88), (c) wavelet coefficients at scale 24.

location of this wavelet maxima is at the center of the mass. When the scale becomes small enough, the detector starts to focus on smaller structures, i.e., the boundary of the mass. The wavelet maximum moves toward the edge of the mass as the scale decreases. And the wavelet representation become a ring as shown in 20 (c). The local maximum across the scale is the best scale to detect that mass since the difference of ROI to its background is maximized.

Having proved the case using an ideal phantom, we now apply our scale search scheme to medium size mass in the RMI phantom already shown in 12 (a). Figure 22 shows a similar result to the ideal phantom case. The noise in the RMI radiograph cause some small fluctuation in the Contrast-Scale curve. If stuck at a small local maximum during the search for maximum, i, we use a small force to get away from the small local maxima. Eventually, we will reach the maximum. We also test our algorithm on some real mammograms, shown in Figure 14, 16 and 17. The results are shown in Figure 23, 24 and 25. All these searches find a maximum across the scale. When we use these best scale in our detector, we could use higher the detection threshold than when we randomly pick a scale.

2.2.5 Summary

In this chapter, we derived a novel continuous scale wavelet detector. The importance of arbitrary scale analysis was demonstrated by digital radiographs of a mammography phantom and digitized mammograms. For the first time, wavelets and CFAR detectors were combined into a single formulation. And we demonstrated that this powerful detector was able to detect very subtle masses, which were rated to be almost invisible by radiologist specializing in mammography.

We have put maxima-across-scale scheme [51, 52] under the wavelet framework. We have
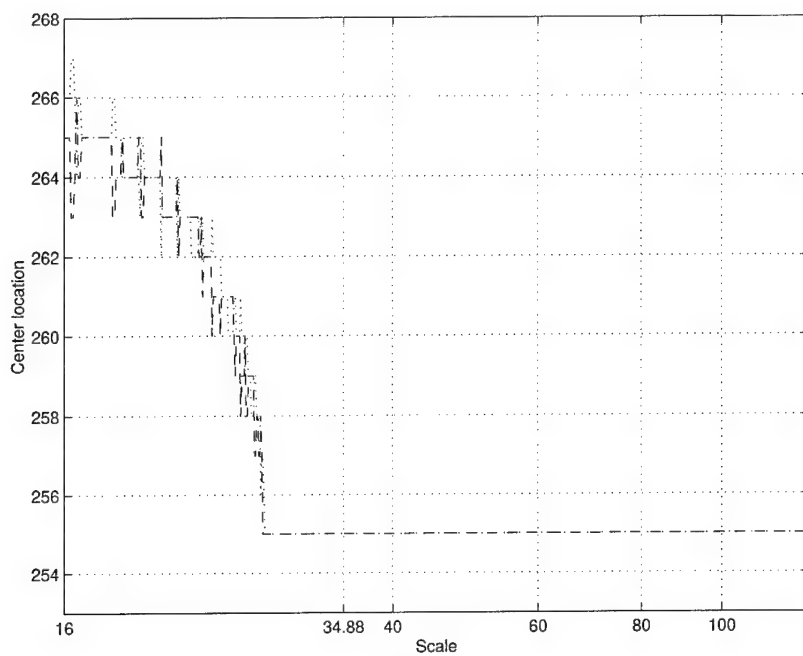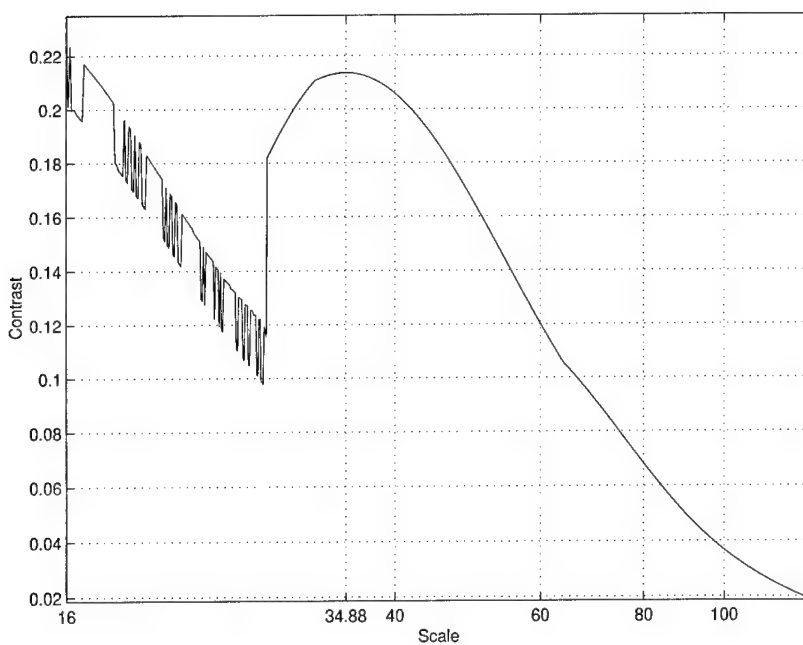
Figure 21: Best scale selection: (a) The location of wavelet maximum, (b) the scale search.

68
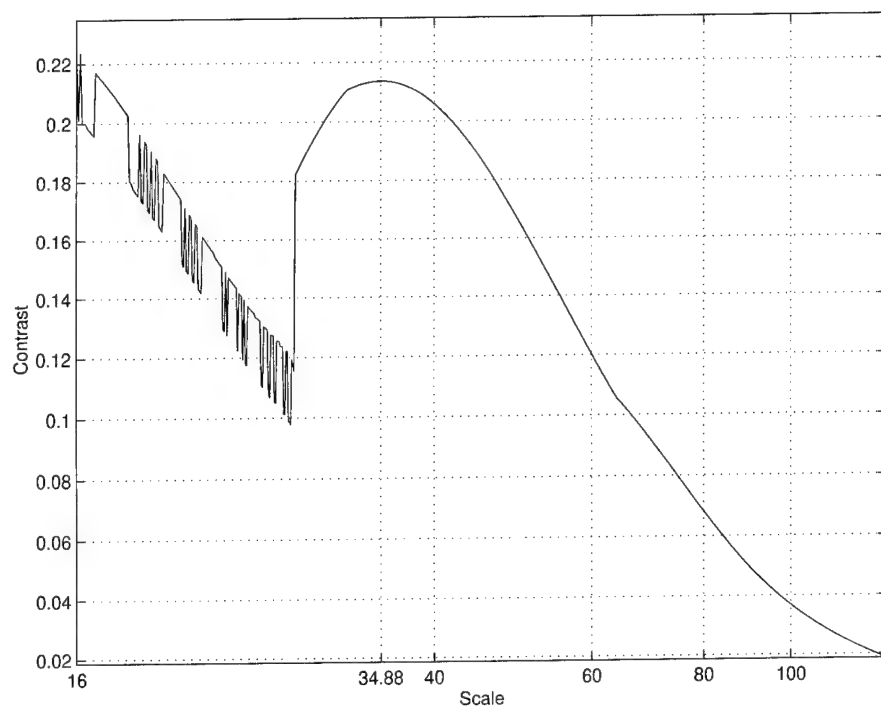
Figure 22: Searching for the best scale: RMI phantom 2216.
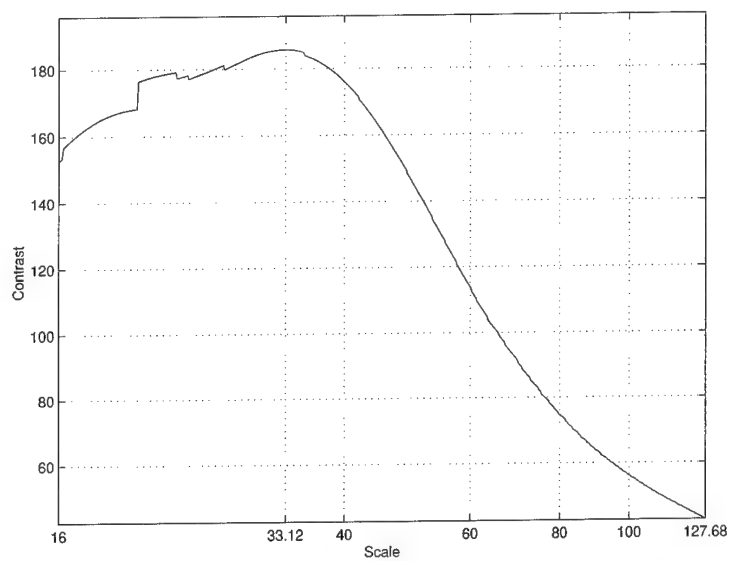
Figure 23: Searching for the best scale: Mammogram case lcc046.

69
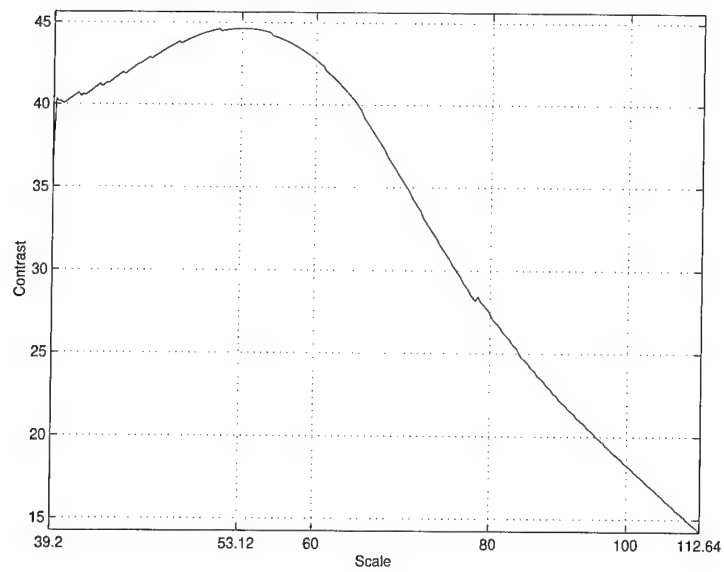
Figure 24: Searching for the best scale: Mammogram case lcc004.
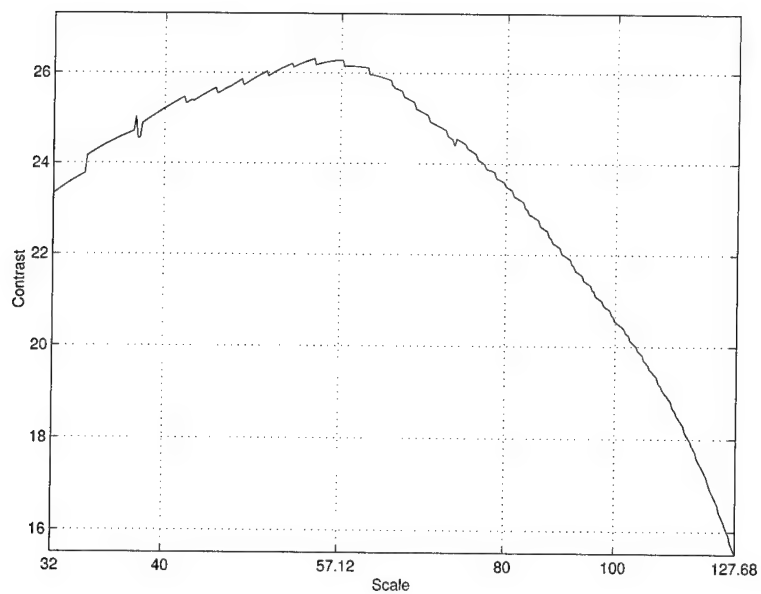
Figure 25: Searching for the best scale: Real mammogram case lcc002.

shown that wavelet maxima across scales can provide the boundary information of an object and also indicate the location of an object. By combining wavelet theory and the geometric knowledge of a tumor, we propose to use a normalized contrast as an index to find the best scale. This method is shown to be effective in the scale selection for tumor detection.

2.3 Coherence of Multiscale Features for Digital Mammogram Enhancement

2.3.1 Introduction

Mammograms can detect tumors that are an eighth of an inch in diameter, while manual examination usually fails to detect tumors smaller than a half-inch. Reliable diagnosis by radiographs of malignant breast disease depends on observing local and distant changes in tissues produced by disease. Of the visual clues of cancer sought by radiologists, the preliminary signs of masses and calcifications are most important [53, 54]. Unfortunately, at the early stages of breast cancer, these signs are very subtle and varied in appearance, making diagnosis difficult and challenging even to specialists [53, 28].

Radiographic signs of cancer are related to tumor mass and its density, size, shape, borders and calcification content. Extraction of these features and enhancement of them can assist radiologists to locate suspicious areas more reliably [55].

Multiscale representations based on wavelets have been carried out for mammographic feature analysis [9, 56, 57]. Laine *et al.* [9] used two overcomplete multiscale representations for contrast enhancement. Mammograms were reconstructed from transform coefficients modified at each level by nonlinear weighting functions. Qian *et al.* [56] introduced tree-structured nonlinear filters for microcalcification cluster detection. An image was enhanced by tree-structured nonlinear filters with fixed parameters and adaptive order statistic filters. Richardson Jr. [57] applied linear and nonlinear filtering approaches to the analysis of mammograms. Here, a linear multiscale decomposition was obtained via a wavelet transform; a nonlinear multiscale decomposition employed a "mean curvature partial differential equation" filter and "weighted majority-minimum range" filter. In addition, Li *et al.* [58] extended a conventional multiresolution wavelet transform into a multiresolution and multiorientation wavelet transform. They applied directional wavelet analysis to capture orientation information within each mammogram.

Freeman and Adelson [29] first proposed the concept of steerable filters and applied it to several problems in the area of computer vision. With a set of "basis filters", one can adaptively steer a filter along any orientation. Hilbert transform pairs were constructed to find a local "oriented energy" measure and dominant orientation.

Kass and Witkin [59] developed an algorithm for estimating the orientation of texture patterns. An orientation pattern was decomposed into a flow field, describing the direction of anisotropy, and a residual pattern obtained by describing the image in a coordinate system built from the flow field. The texture orientation was estimated from Laplacian of Gaussian filters. Rao and Schunck [60] proposed another algorithm based on the gradient

of the Gaussian. Their new algorithm incorporated a more sophisticated scheme for computing the coherence of the flow field.

In this chapter, an enhancement algorithm based on overcomplete multiscale wavelet analysis is described. These redundant representations provide the property of shift invariance which is shown to be advantageous for our analysis. Features were extracted by separable steerable filters. A coherent image and phase information were then generated. A nonlinear function, integrating coherent image and phase information, was applied to the transform coefficients at each level of analysis. An enhanced image was obtained via an inverse wavelet transform of the modified coefficients. The novelty and advantage of this algorithm compared to existing techniques lies in its detection of directional features and the lack of perturbations (artifacts) in processed images.

2.3.2 Background

In this section we briefly describe the mathematical background and fundamental ideas used in subsequent sections.

Wavelet Transforms

Wavelet transforms have become acknowledged as useful tools for many applications in signal processing. A function $\psi(x)$ is said to be a wavelet if and only if its Fourier transform $\hat{\psi}(\xi)$ satisfies the *admissibility condition*

$$C_\psi = \int_{-\infty}^{+\infty} \frac{|\hat{\psi}(\xi)|^2}{|\xi|} d\xi < \infty. \tag{69}$$

This condition implies that

$$\int_{-\infty}^{+\infty} \psi(x) dx = 0. \tag{70}$$

This means that $\psi(x)$ will have at least some oscillations.

Wavelets constitute a family of functions derived from one single function ψ (*mother wavelet*) by dilations and translations

$$\psi_{a,b}(x) = \frac{1}{\sqrt{|a|}} \psi\left(\frac{x-b}{a}\right), \tag{71}$$

where $a \in R^+, b \in R$. The idea of the wavelet transform is to represent any function $f(t)$ as a superposition of wavelets. The continuous wavelet transform is defined as

$$W_f(a,b) = \langle f, \psi_{a,b} \rangle = \frac{1}{\sqrt{|a|}} \int_{-\infty}^{+\infty} f(x) \overline{\psi\left(\frac{x-b}{a}\right)} dx, \tag{72}$$

73

where $\bar{\psi}$ denotes the complex conjugate of ψ. A function can be reconstructed from its wavelet transform by means of the *"resolution of identity"* formula

$$f = \frac{1}{C_\psi} \int_{-\infty}^{+\infty} \int_{-\infty}^{+\infty} \langle f, \psi_{a,b} \rangle \, \psi_{a,b} \frac{dadb}{a^2}. \tag{73}$$

In the application of digital mammography, one prefers to express f as a discrete superposition. Let us discretize the translation and dilation parameters of the wavelet in Equation (71):

$$\psi_{m,n}(x) = a_0^{-\frac{m}{2}} \psi(a_0^{-m} x - nb_0), \tag{74}$$

where $a = a_0^m, b = nb_0 a_0^m$, with $m, n \in Z$, and $a_0 > 1, b_0 \neq 0$. On this discrete grid, the wavelet transform is simply

$$W_f(m,n) = a_0^{-\frac{m}{2}} \int_{-\infty}^{+\infty} f(x)\psi(a_0^{-m}x - nb_0)dx. \tag{75}$$

The original signal can be approximated as linear combinations of the wavelet bases,

$$f(x) \approx \sum_{m,n} W_f(m,n)\psi_{m,n}(x). \tag{76}$$

One popular discretization is to choose $a_0 = 2, b_0 = 1$,

$$\psi_{m,n}(x) = 2^{-\frac{m}{2}} \psi(2^{-m}x - n), \tag{77}$$

which are called *dyadic wavelets*.

Steerable Filters

A function $f(x,y)$ is called "steerable" if it can be expressed as a linear combination of rotated versions of itself. The fundamental idea of steerable filters is to apply "basis filters" which correspond to a fixed set of orientations and interpolate between each discrete response. Thus, one must decide the number of "basis filters" and the corresponding interpolation functions. Let θ_i be the angle of ith basis filter and $k_i(\theta)$ denote an interpolation function. As defined in [29] a steering constraint may be formulated by

$$f^\theta(x,y) = \sum_{i=1}^{M} k_i(\theta) f^{\theta_i}(x,y), \tag{78}$$

where M is the number of basis functions required to steer a function $f^{\theta_i}(x,y)$. Hereafter, it will be more convenient to work in polar coordinates $r = \sqrt{x^2 + y^2}$ and $\phi = \arg(x,y)$. Let f be any function that can be expressed as a Fourier series in polar angle ϕ:

$$f(r,\phi) = \sum_{n=-L}^{L} a_n(r)e^{jn\phi}, \tag{79}$$

where $j = \sqrt{-1}$ and L is the length of the coefficients.

Local Energy

Based on physiological evidence, a local energy operator was first proposed by Morrone and Owens [61]. Rather than considering differential properties, they studied the properties of the Fourier expansion of an intensity function. They demonstrated that the maxima of an energy function are coincident with the points of maximum phase congruency and visual features.

Let $IG(\theta)$ and $IG^H(\theta)$ be the outputs of constituent filter $G(\theta)$ and its quadrature pair $G^H(\theta)$, respectively. The oriented energy function can be expressed by the squared outputs of a quadrature pair of filters steered to an angle θ, that is,

$$E(\theta) = [IG(\theta)]^2 + [IG^H(\theta)]^2. \tag{80}$$

Since $IG(\theta)$ and $IG^H(\theta)$ can be expressed as a sum of basis filter outputs times interpolation functions, following [29], Equation (80) can be simplified to a Fourier series in angular form using substitutions obtained by the trigonometric identity:

$$E(\theta) = a_0 + a_1 \cos(2\theta) + a_2 \sin(2\theta) + [\ higher\ order\ terms \cdots].$$

The lowest frequency terms of this identity were used to approximate the dominant directions A and their associated magnitudes M,

$$A = \arctan[a_1, a_2]/2, \tag{81}$$
$$M = \sqrt{a_1^2 + a_2^2}. \tag{82}$$

Figure 26 shows the oriented energy map of a two-dimensional Gaussian function

$$f(x, y) = e^{-(x^2 + y^2)}.$$

The test function is shown in Figure 26(a). Using a second derivative of Gaussian function and its Hilbert transform to measure oriented energy, we plot the direction and magnitude of each position on a map where the arrow indicates the direction and the length is the magnitude, which is shown in Figure 26(b). The edges were detected at the inflection points of the surface. The magnitudes of the energy function are maxima, therefore the lengths are longer than those of other points of the function.

Note that Figure 26(b) does not show the correct phases in the upper half of the map. All the arrows are pointing outward instead of inward. There is a 180° phase shift. This is because the oriented energy is obtained from the squared outputs of quadrature pairs. We applied a simple algorithm to correct this phase shift. First, we divide the space into 8
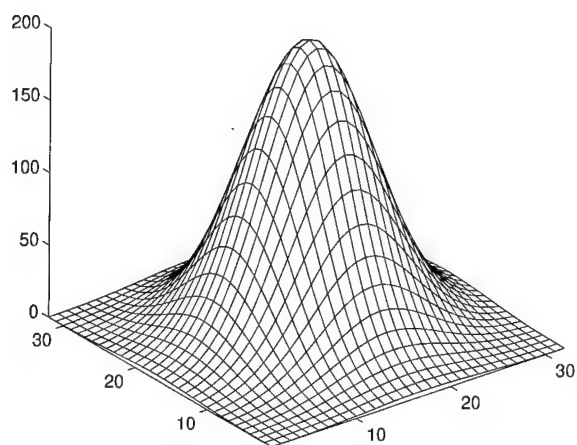
(a) A test function.
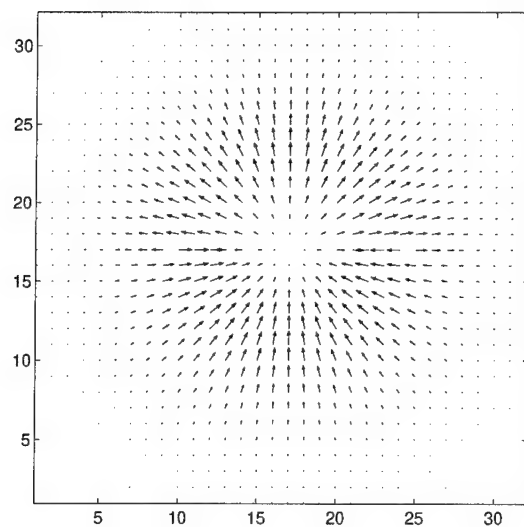
(b) The orientation and magnitude map of a test function.

Figure 26: An example of oriented energy map construction.
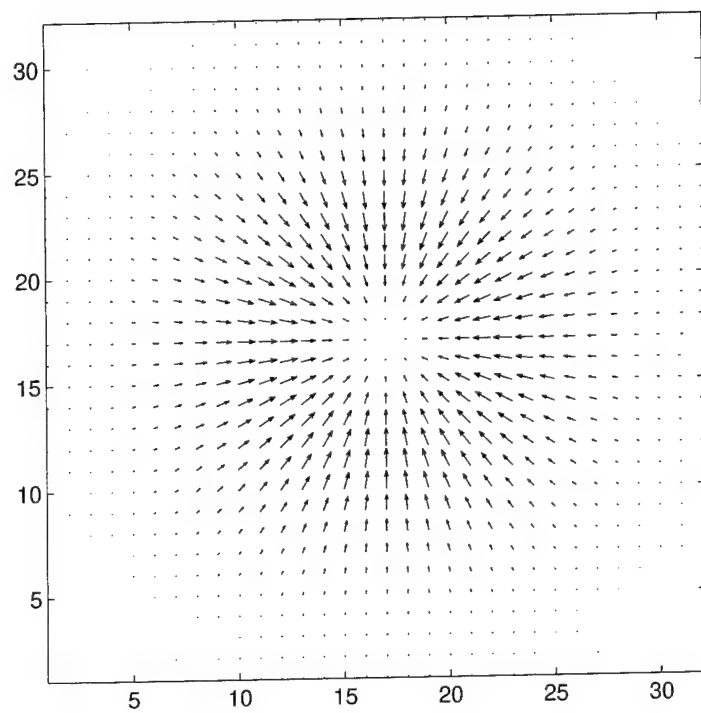
Figure 27: A corrected oriented energy map.

directions and approximate the phase at each point to exactly one of these discrete orientations. Next, the neighbors of each point along the approximated direction are examined. If the intensities along that direction are increasing, the phase is not changed; otherwise, we correct the phase by a 180° shift. A sample corrected oriented energy map is shown in Figure 27.

Measure of Coherence

Texture plays an important role in many machine vision and image processing tasks including surface inspection, scene classification, surface orientation and shape determination [62]. Texture patterns may be characterized by extracting measurements that quantify the nature and directions of patterns. Most breast carcinomas have the appearance of stellate lesions consisting of a central mass surrounded by radiating spicules [53]. The spicules radiate outward in all directions and vary in length. This provides an important cue for the early detection of such lesions.

Much attention has been given to the notion of decomposing an intensity image into intrinsic images to extract meaningful information [63, 64]. Such intrinsic properties represent basic components of the image formation process and therefore can reveal features "hidden" inside an image. The information they provide is beyond the intensity image alone.

Rao and Schunck [60] defined the orientation field of a texture image to consist of two images — an *angle* image and a *coherence* image. The angle image denotes the dominant local orientation at each point while the coherence image represents the degree of anisotropy at each point. They strongly advocated the use of angle and coherence images as *intrinsic* images. In this paper, we investigated the efficiency of these two representations to capture and enhance features of importance to mammography.

2.3.3 Methodology

Our algorithm consists of four steps: (1) construction of an overcomplete multiscale representation, (2) processing via separable steerable filter analysis, (3) computing coherence measures and (4) application of nonlinear operators, as shown in Figure 28 [65]. We next describe each block in the sections below.

(1) Overcomplete Multiscale Representations: Wavelet transforms, owing to their localization characteristics, are powerful tools of analysis for many signal and image processing applications. Multiscale analysis can extract features at distinct scales and provide local information often hidden in an original mammogram. One major drawback of wavelet transforms is their lack of translation invariance [45], making the content of wavelet subbands unstable under the translations of an input signal. In our algorithm, a
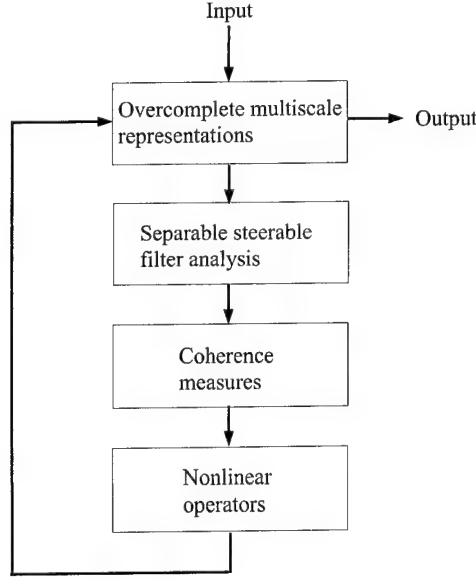
Figure 28: Block diagram of the proposed algorithm.

digitized mammogram was decomposed using a fast wavelet transform algorithm (FWT) [15]. In order to obtain wavelet coefficients at each level without downsampling, an undecimated *"algorithme à trous"* (algorithm with holes) [21, 66] was implemented. In the spatial domain, the redundant representation corresponds to no aliasing.

Let S^0 denote an original image and $D^i f$ be obtained by inserting $2^i - 1$ zeros between every pair of the coefficients representing f. $(D^i f)_x$ and $(D^i f)_y$ stand for carrying out convolution operations with the filter $D^i f$ along x and y directions, respectively. The decomposition and reconstruction equations at level i are as follows:

Decomposition:

$$
\begin{aligned}
S^{i+1} &= S^i * (D^i h)_x * (D^i h)_y, \\
W_x^{i+1} &= S^i * (D^i g)_x, \\
W_y^{i+1} &= S^i * (D^i g)_y.
\end{aligned}
\tag{83}
$$

Reconstruction:

$$
S^i = W_x^{i+1} * (D^i k)_x * (D^i l)_y + W_y^{i+1} * (D^i l)_x * (D^i k)_y + S^{i+1} * (D^i \bar{h})_x * (D^i \bar{h})_y,
\tag{84}
$$

where "$*$" indicates discrete convolution, and $h, g, k,$ and l are filters whose Fourier transforms $(H(\omega), G(\omega), K(\omega),$ and $L(\omega)$, respectively) satisfy [15]

$$
\begin{aligned}
G(\omega)K(\omega) + |H(\omega)|^2 &= 1, \\
L(\omega) &= \frac{1 + |H(\omega)|^2}{2}.
\end{aligned}
\tag{85}
$$

S^i ⟶ $(D^i h)_x$ ⟶ $(D^i h)_y$ ⟶ S^{i+1}

⟶ $(D^i g)_x$ ⟶ W_x^{i+1}

⟶ $(D^i g)_y$ ⟶ W_y^{i+1}

(a)

S^{i+1} ⟶ $(D^i \bar{h})_x$ ⟶ $(D^i \bar{h})_y$ ⊕ ⟶ S^i

W_x^{i+1} ⟶ $(D^i k)_x$ ⟶ $(D^i l)_y$

W_y^{i+1} ⟶ $(D^i l)_x$ ⟶ $(D^i k)_y$

(b)
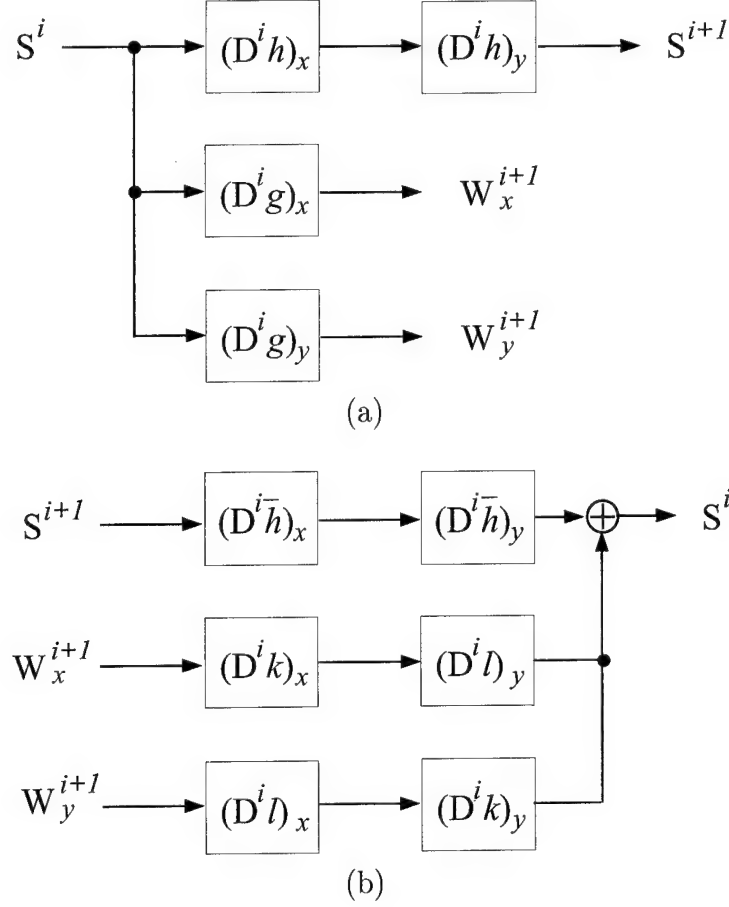
Figure 29: Block diagram of a fast wavelet transform at level i. (a) Decomposition. (b) Reconstruction.

The block diagrams of decomposition and reconstruction operations at level i were shown in Figure 29(a) and (b), respectively.

(2) Separable Steerable Filter Analysis: A filter is called "steerable" if the filter at an arbitrary orientation can be expressed as a linear combination of a set of basis filters, generated from rotations of a single kernel [29]. Steerable filters [29, 67, 68], which can be adaptively adjusted to arbitrary orientation, were used to detect stellate patterns of spicules and locate feature orientations more precisely. As pointed out by [69], the separability property of the filters can speed up computations considerably when convolved with a large image matrix. In our algorithm, we used three basis functions as steerable filters. The x-y separable steerable approximations of filter kernels were generated by Singular Value Decomposition (SVD) [29, 69]. Using a set of separable steerable filters, the magnitude (M^i) and associated dominant directions (A^i) of local energy were determined by the basis functions and their Hilbert transforms [29, 70, 61, 71]. Figure 30 illustrates the detailed procedure of steerable filter processing. We applied separable steerable filters to an

original image S^0 and a low-pass filtered image at each level $S^i, i = 1, \ldots n$, to capture salient multiscale features. Discrete realizations of the three basis functions were applied in our implementation algorithm. An approximation of Hilbert transform of basis function was thereafter obtained.

(3) Coherence Measures: A coherence map is an image showing a local measure of the degree of anisotropy of flow [59, 60]. If the orientations of a texture pattern at any point (x_i, y_i) are coherent, then magnitude and phase information are important and should be emphasized. Conversely, if the orientations are not coherent, the magnitude and phase information can be neglected or attenuated. Kass and Witkin [59] suggested a simple way of measuring strength of coherence by finding the ratio

$$\chi(j, k) = \frac{|W(j, k) J(j, k)|}{(W(j, k) |J(j, k)|)}, \tag{86}$$

where $W(j, k)$ denotes a local weighting function with unit integral, $J(j, k)$ denotes the squared gradient vector at (j, k), and $|\cdot|$ denotes absolute value.

An alternative measure of coherence was proposed by Rao and Schunck [60] and was obtained by weighting the energy with the normalized projection of energy within a specified window $(\mathcal{W})$ onto the central point (j, k) of a window. The coherence measure (C^i) was expressed as

$$C^i(j, k) = M^i(j, k) \frac{\displaystyle\sum_{(m,n)\in\mathcal{W}} |M^i(m, n) \cos(A^i(j, k) - A^i(m, n))|}{\displaystyle\sum_{(m,n)\in\mathcal{W}} M^i(m, n)}, \tag{87}$$

where $M^i(j, k)$ and $A^i(j, k)$ denote energy and phase of point (j, k) at level i, respectively. This coherence measure incorporates the gradient magnitude and hence places more weight on regions that have higher visual contrast. Let us examine more closely how the coherence measure works. Suppose that there is a region somewhere in an image, as shown in Figure 31. Pixel A is on a vertical edge line because its magnitude is maximum along the direction of its phase. (Actually, there is an edge along the vertical direction of pixel A.) The coherence at pixel A is measured inside Window 1 which surrounds pixel A. Since the pixels inside Window 1 have the same phases as pixel A, the coherence of pixel A is equal to the magnitude at this pixel. While the pixels, surrounding pixel B, inside Window 2 point to distinct directions, the projections of these pixels on pixel B will be balanced. The coherence at pixel B is reduced. This pixel can be considered a disturbance.

Experimentally, this method out-performed previous measures applied to similar data [60]. In our algorithm, we implemented this approach to measure each coherence map. In order
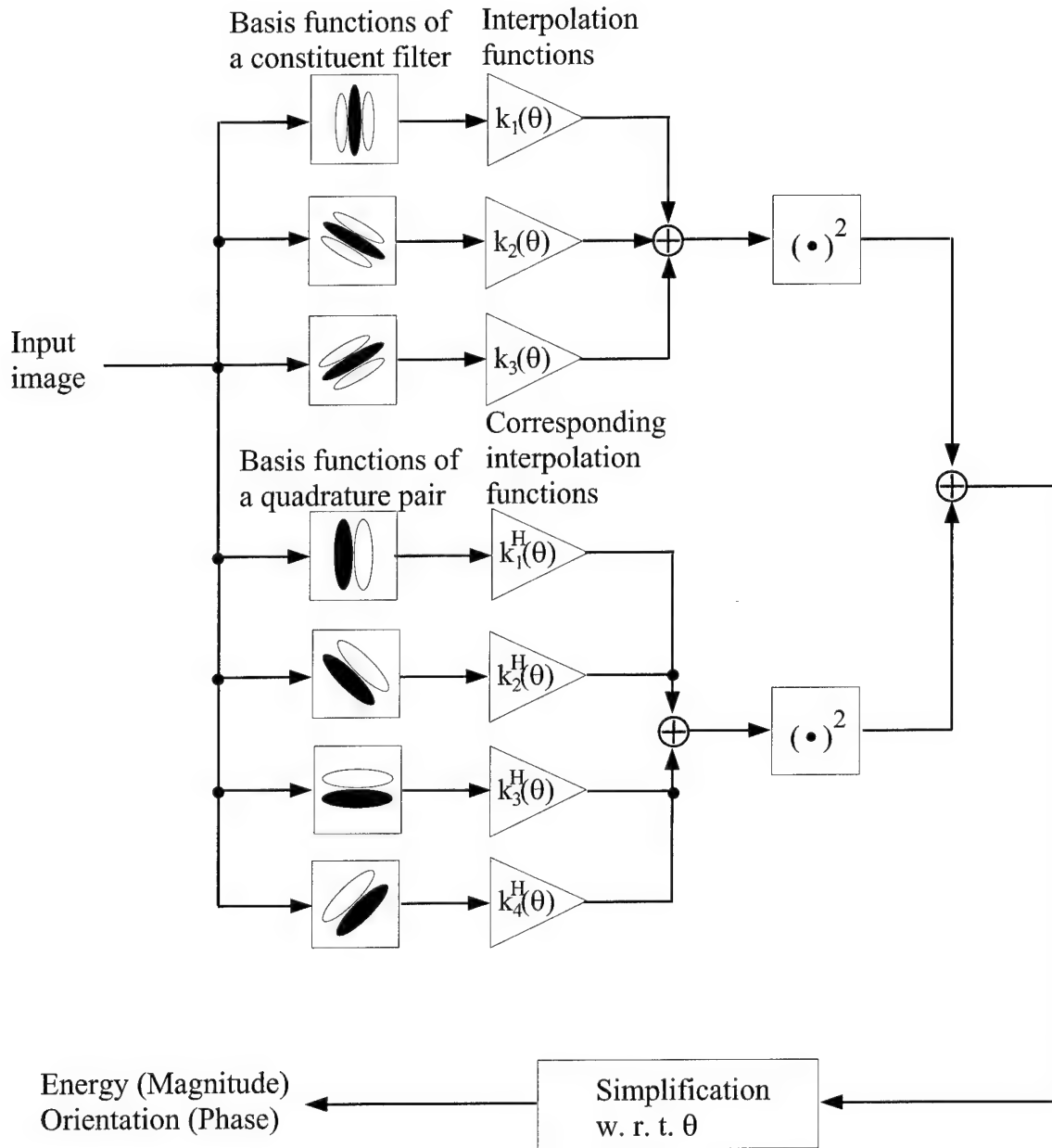
Figure 30: Diagram of steerable filter processing.
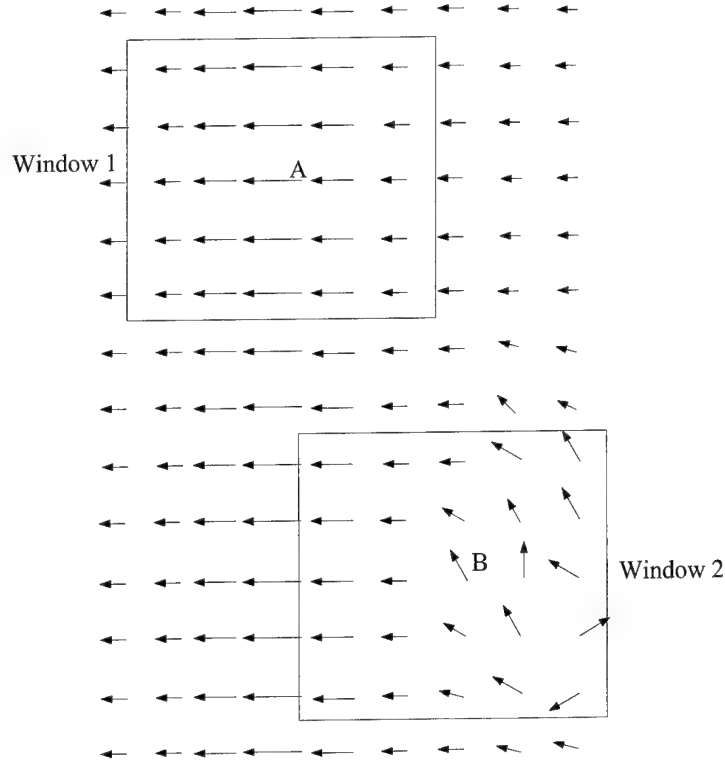
Figure 31: An example showing the effectiveness of coherence measure.

to capture features at each level, we changed the window size at each distinct level. At the finest level, a 5×5 window was used. While for the coarser levels, larger windows (e.g. 7×7 or 9×9) were used. For simplicity of implementation, an odd window size was selected at each level. Figure 32 shows an example of a 5×5 window used to carry out this operation. The measure of coherence C^i was obtained from Equation (87). The combination of coherence and orientation structure was better able to extract the salient features of spiculated lesions. In overview, a schematic diagram of processing Steps 1–3 is shown in Figure 33.

(4) Nonlinear Operators: We have now computed all the information needed complete algorithm. A nonlinear operation is next applied within each level to precisely modify transform coefficients. This operation integrates both coherence map and phase information, as described below:

A. Modification from Coherence Maps:

Let $C^i(j, k)$ denote the coherence measure of point (j, k) at some level i. First, we find the local maxima of the coherence map at each level. These maxima correspond to features in an image and their propagations at distinct levels of analysis. Therefore they are likely locations to "boost" or amplify. We call these maps (C^i_f) *feature maps*. Then the maxima
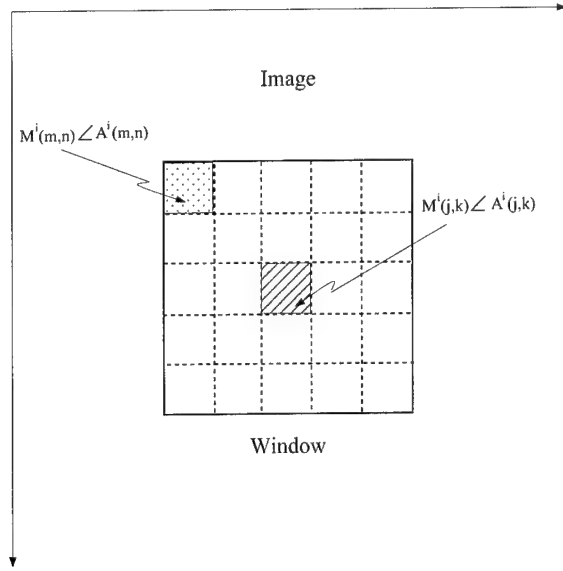
Figure 32: Illustration of measuring the coherence of an image.

or square roots of these maxima are mapped into 256 scales, depending on the threshold value of the scale (S_t^i) at the first level (We will describe how to obtain this value later). That is,

$$
\begin{cases}
255 \dfrac{C_f^i - C_{f,min}^i}{C_{f,max}^i - C_{f,min}^i}, & \text{if } S_t^1 < S_T, \\[2ex]
255 \dfrac{\sqrt{C_f^i} - \sqrt{C_{f,min}^i}}{\sqrt{C_{f,max}^i} - \sqrt{C_{f,min}^i}}, & otherwise,
\end{cases}
$$

where $C_{f,max}^i$ and $C_{f,min}^i$ are maximum and minimum of C_f^i, respectively. S_T is a prespecified threshold value. We compute the square root of the maxima because the difference between the maximal values might be large (especially at the first two levels). This operation prevents most values mapping to a small scale.

We then construct a histogram of square roots of local maxima and accumulate the number of mappings from 1 up to some scale (S_t^i), so that the accumulated number is over 99% of the total local maxima. The corresponding value of that scale is then chosen as the threshold value $(C_{f,t}^i)$ for that level.

Modifications of coherence maps were obtained by a nonlinear function expressed as

$$
C_{mod}^i(j,k) = \begin{cases}
\sqrt{\dfrac{C^i(j,k)}{C_{mean}^i(j,k)}}, & \text{if } C^i(j,k) < C_{f,t}^i(j,k), \\[3ex]
\sqrt{\dfrac{C_{f,t}^i(j,k)}{C_{mean}^i(j,k)}}, & otherwise,
\end{cases}
\tag{88}
$$

where $C_{mean}^i(j,k)$ is the mean value of the figure map at each i-th level. For an image with a black background, the background pixels are not be counted in computing the mean

84

Figure 33: Overview of processing for steps 1–3.

value. The square root values were computed so that we would not over-emphasize large local maxima and ignore the small local maxima.

B. Modification from Phase:

Phase information is important to distinctly characterize oriented texture. Therefore we did not neglect its contribution in the modific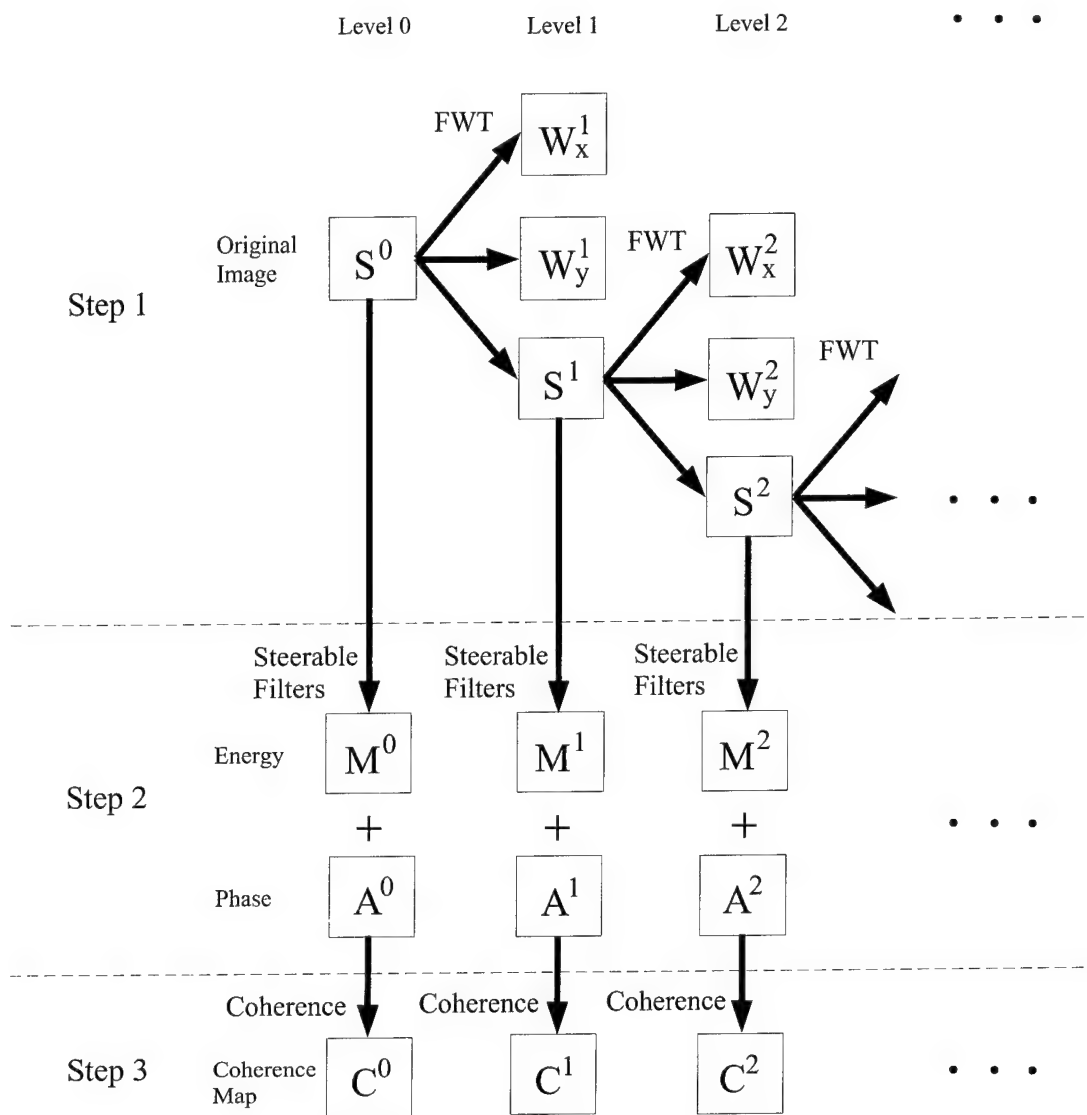ation of coefficients. We applied a sinusoidal weighting to phase information. The detail sub-bands of wavelet coefficients obtained in Step 1 included two components: the component along the x direction and the component along the y direction. The x component was obtained by high-pass filtering along the x direction, hence mostly vertical features within the mammogram were detected. We emphasized the points whose dominant orientations were near 0 and π (with respect to the vertical axis). Thus, the modification from phase information was

$$A^i_{mod}(j,k) = |\cos(A^i(j,k))|. \tag{89}$$

The y component was obtained by high-pass filtering along the y direction, detecting horizontal features. We emphasized the points whose dominant orientations were near $\frac{\pi}{2}$ and $\frac{3\pi}{2}$ (with respect to the vertical axis). Transform coefficients were modified by phase information by

$$A^i_{mod}(j,k) = |\sin(A^i(j,k))|. \tag{90}$$

The modifications from coherence map and phase at level $i-1$ were combined to adjust the wavelet coefficients at level i. The resultant modification was therefore

$$W^i_{mod} = T^{i-1} \cdot C^{i-1}_{mod} \cdot A^{i-1}_{mod} \cdot W^i, \tag{91}$$

where T^i was a constant at each level. A schematic diagram of this nonlinear operator at level i is shown in Figure 34. Finally, the modified coefficients were then used to reconstruct, via an inverse fast wavelet transform, an enhanced visualization of mammographic features.

2.3.4 Experimental Results and Discussion

In this section, we present some examples of processed results. First, we show a one-dimensional example which does not take advantages of oriented information. We perform an overcomplete wavelet transform to the signal and decompose it into five levels. The enhanced signal and the original signal are plotted together in Figure 35 to show the benefit of our algorithm. The transition regions in the original signal are clearly enhanced. Three examples of malignant lesions with distinct radiographic signs of cancer were processed. The images were of matrix size 512×512. For each case, both global and regions of interest (ROI) are shown along with the corresponding enhanced ROI image.
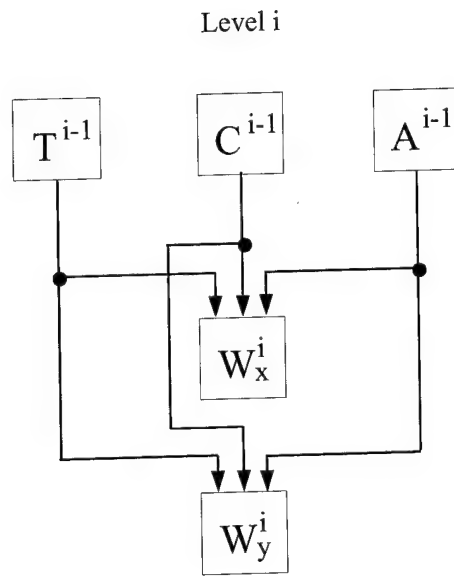
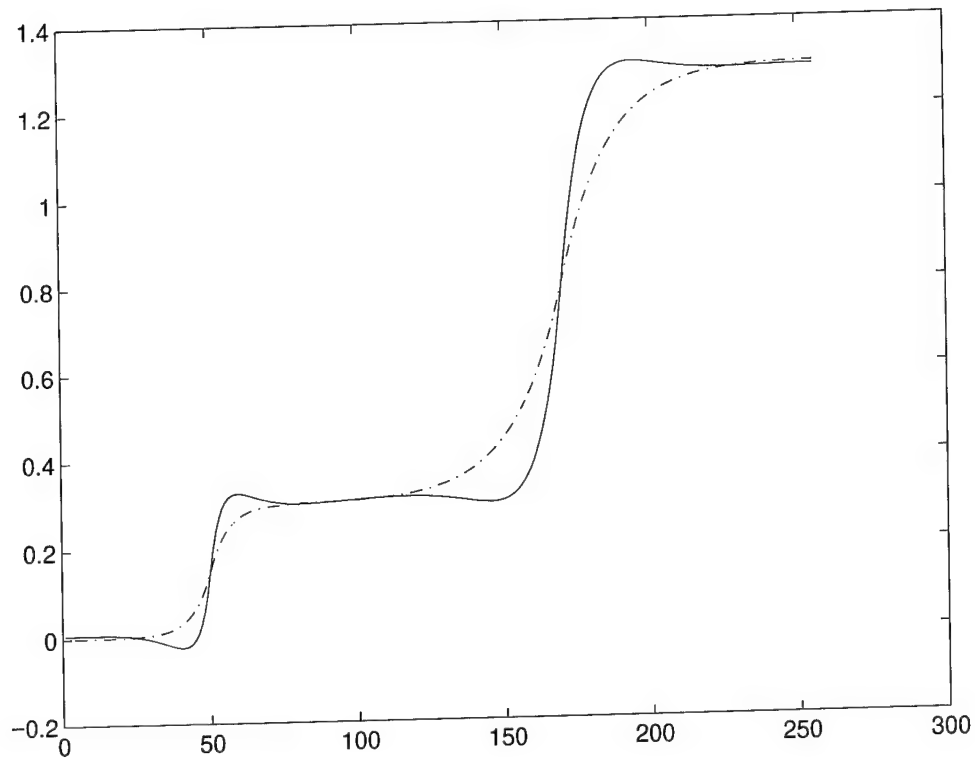Figure 34: A schematic diagram of a nonlinear operator at level i.

Figure 35: Enhanced signal profile (solid line) overlaid with the original signal (dash-dot line).

Microcalcifications

Figure 36 shows a sample mammogram (mam008rml) with microcalcification clusters. The original mammogram is shown in Figure 36(a). Figure 36(b) shows an original suspicious area of the mammogram. After enhancement, clusters of calcifications clearly appear in the center of the image.

Stellate lesions

A mammogram (mam041rml) with a stellate lesion is shown in Figure 37. Figure 37(a) shows the original image. Figure 37(b) presents an original digital radiograph with a partially obscured irregular mass in the center of the image matrix. After applying our algorithm to this image, the enhanced image makes obvious spiculated lesions around the mass. The mass itself was also enhanced, as shown in Figure 37(c). These clear spiculated patterns suggested radiologists that this mass is more likely malignant.

Masses

A mammogram (mam004lcc) with a mass tumor is shown in Figure 38. The craniocaudal view of the left breast shown in Figure 38(b) contains an irregular spiculated mass in retroglandular fat. The enhanced ROC shown in Figure 38(c) better delineates the margins of the mass.

Figures 39(a) and (b) show five levels of wavelet coefficients along the x and y directions, respectively. The corresponding coherence maps are shown in Figure 40(a). Feature maps are shown in Figure 40(b). The histogram of square roots of local maxima are constructed in Figure 40(c) and threshold scales were determined as 24, 32, 81, 109, and 123 for five levels. The wavelet coefficients were then modified prior to reconstruction.

To validate our enhancement techniques, three mathematical models of phantoms were constructed. The models included features of interest in mammographic imaging, such as masses, microcalcifications, and spicular lesions, as shown in Figure 41. These phantoms were blended into a normal mammogram to form an experimented database. Note that the positions of these mathematical models are different in each image. We constructed twenty cases in our testing database. The images were of matrix size 1024×1024.

Many techniques of contrast manipulation and modification have been developed within the field of digital image processing. However, the measurement and evaluation of contrast and contrast changes in arbitrary images are not uniquely defined in the literature [72, 73]. In this paper, we adopt a definition introduced by Morrow *et al.* [10]

$$C_t = \frac{B_0 - B}{B_0 + B}, \tag{92}$$

where B is the mean gray-level value of a particular object in the image (foreground), and
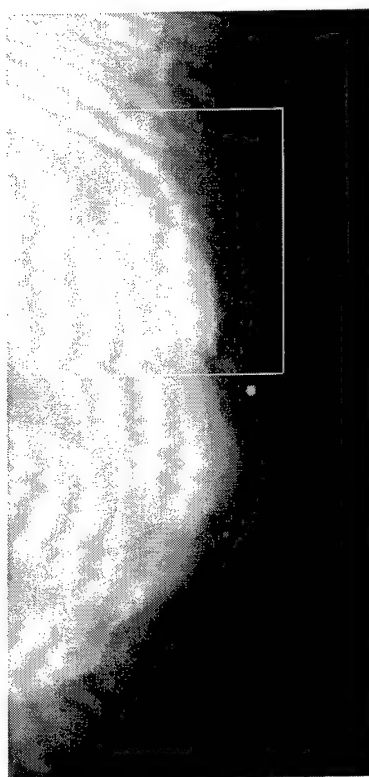
(a)
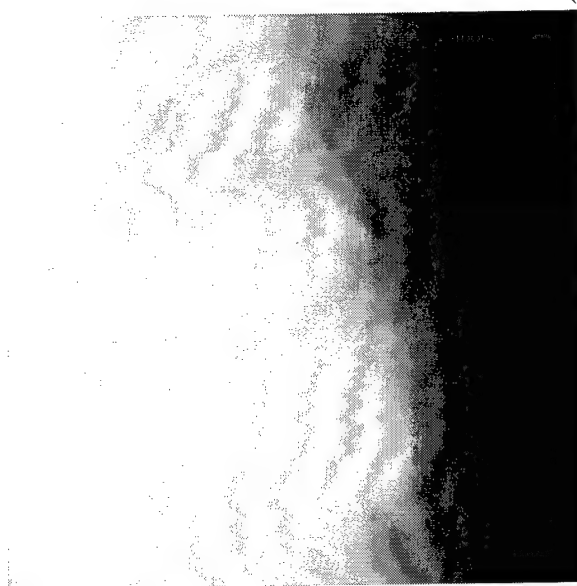
(b)
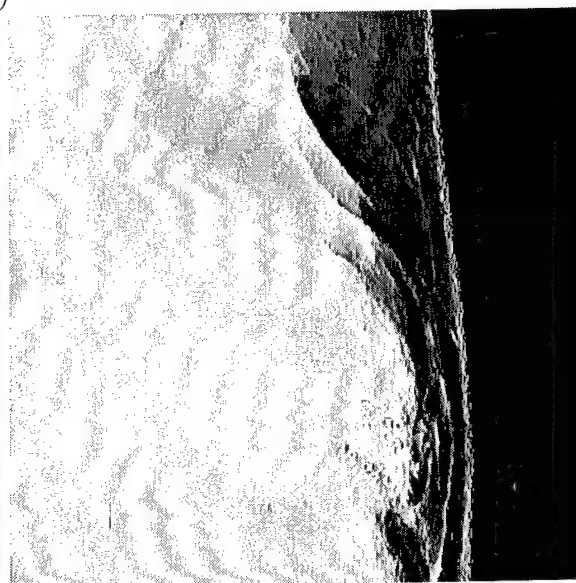
(c)

Figure 36: Mammogram with calcifications: (a) Original mammogram, (b) ROI image, (c) enhanced ROI image.
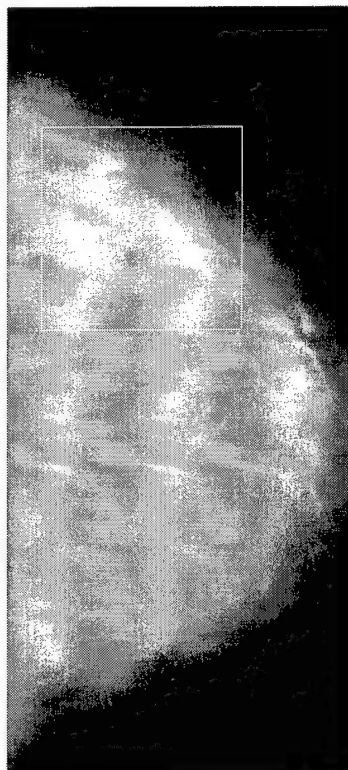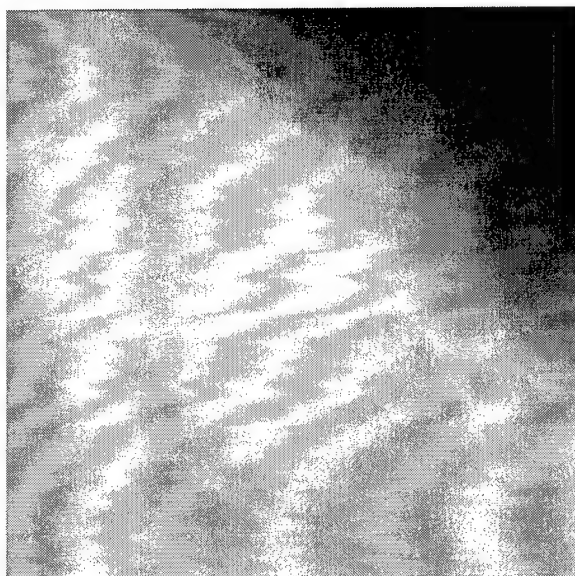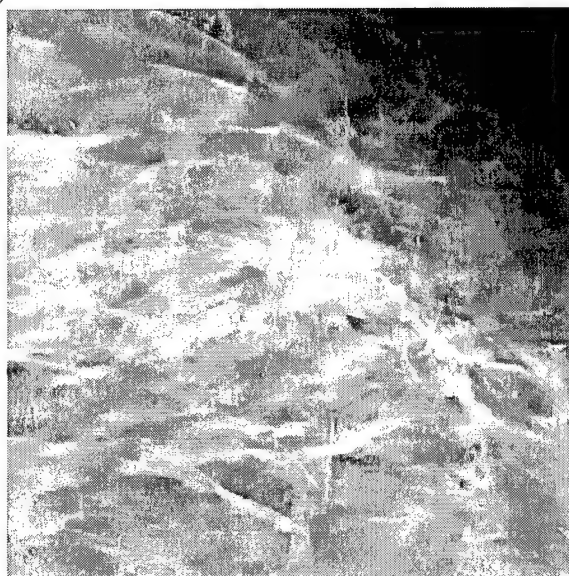
Figure 37: Mammogram with a stellate lesion: (a) Original mammogram, (b) ROI image, (c) enhanced ROI image.
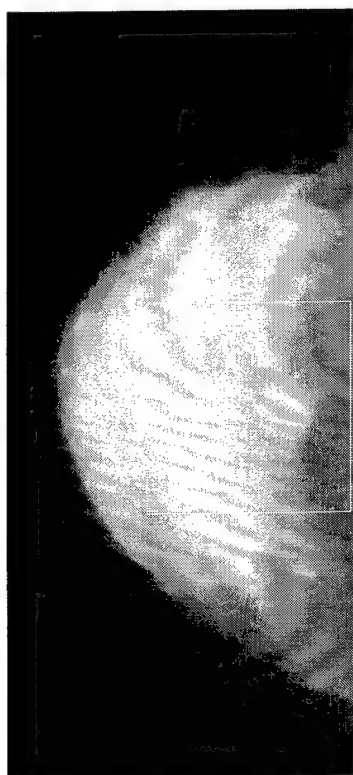
(a)
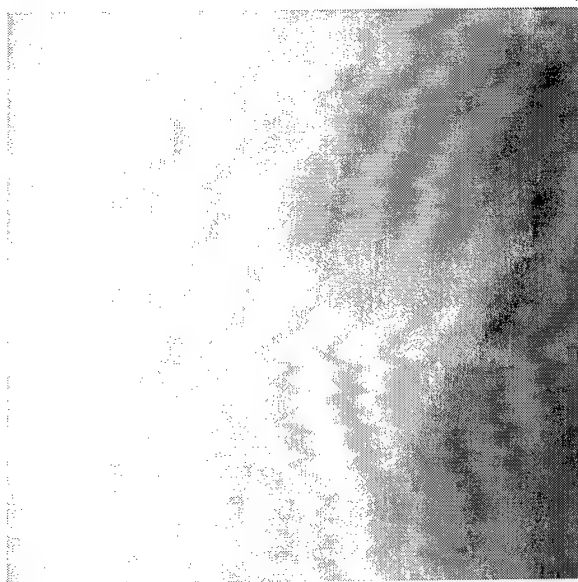
(b)
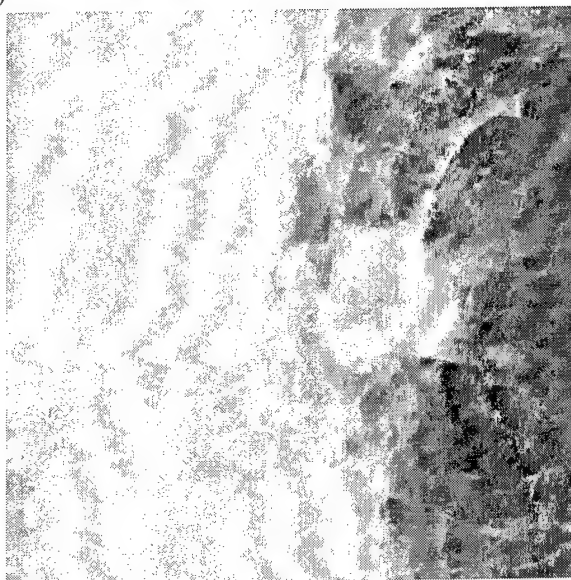
(c)

Figure 38: Mammogram with a mass: (a) Original mammogram, (b) ROI image, (c) enhanced ROI image.

Level 0

Level 1

Level 2

Level 3

Level 4

(a)　　　　　　　　(b)
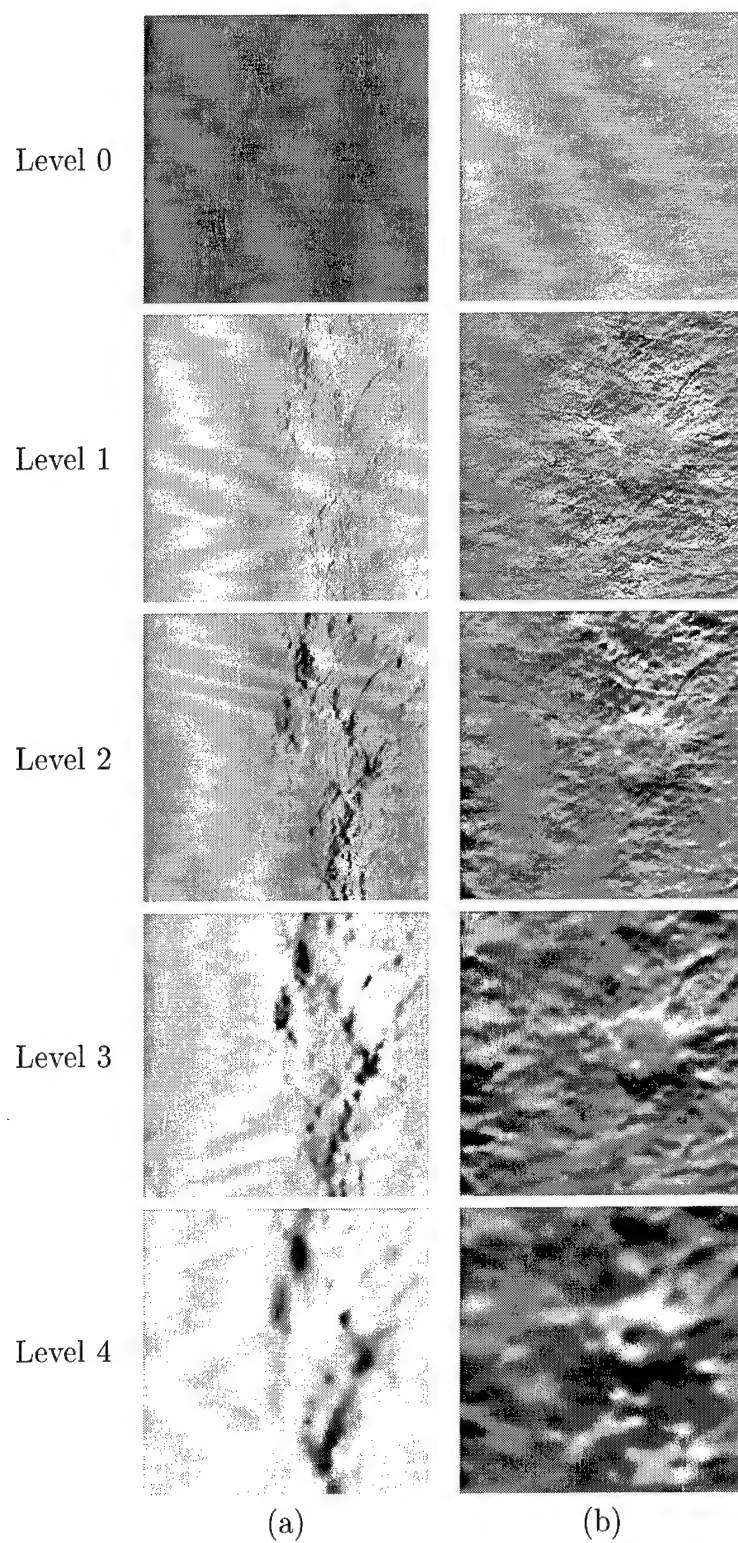
Figure 39: Five levels of wavelet coefficients: (a) x-direction, (b) y-direction.
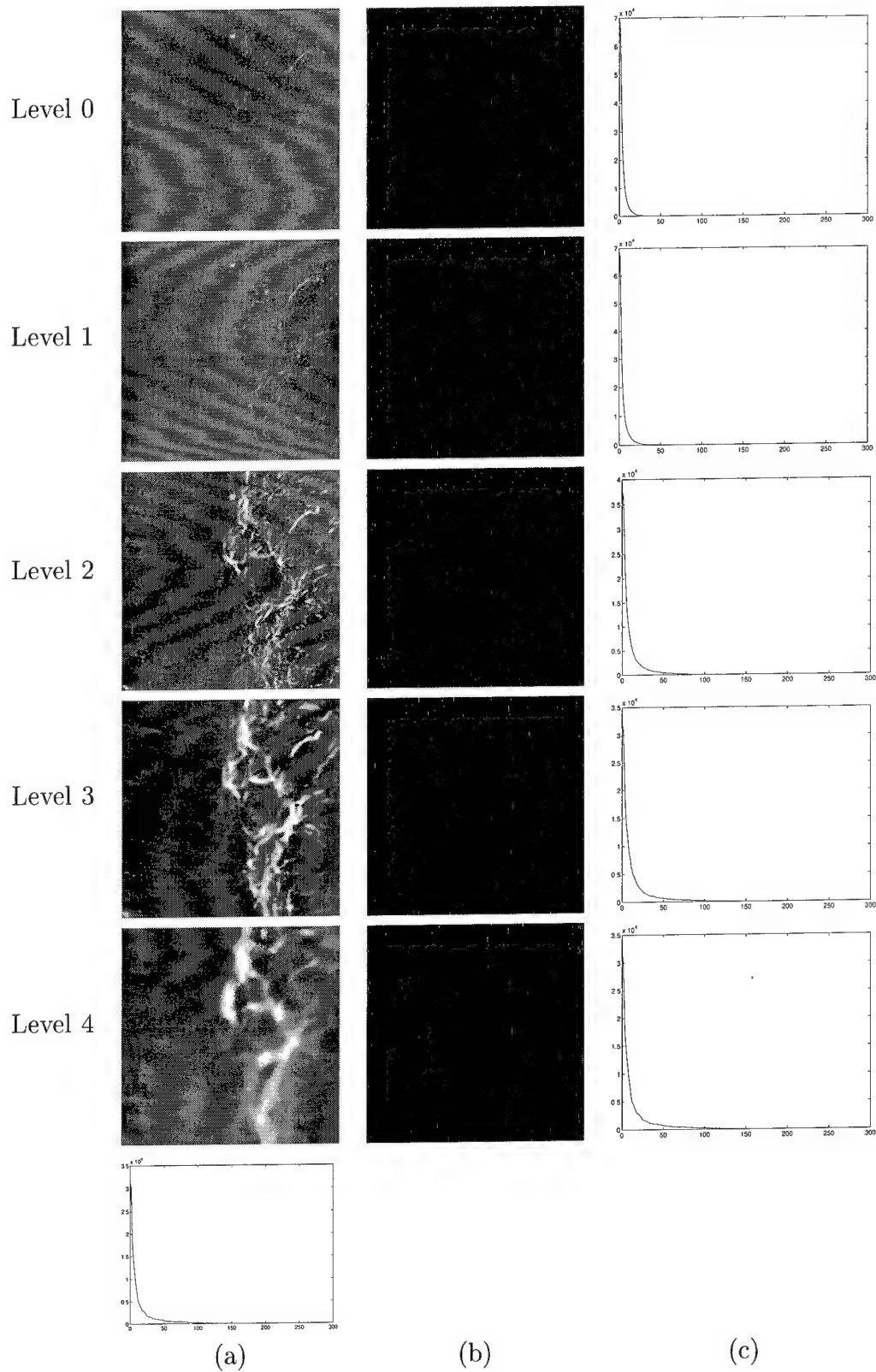
Figure 40: (a) Coherence maps, (b) feature maps, (c) histograms of square roots of local maxima.

93
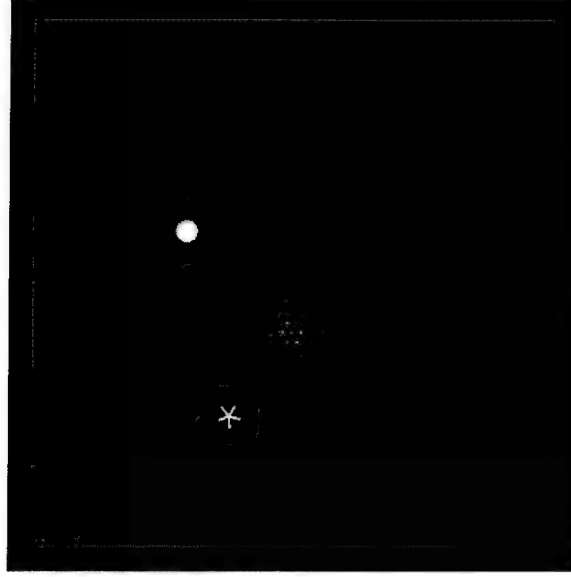
Figure 41: Mathematic phantoms.

B_0 is the mean gray-level value of a surrounding region (background).

Based on this definition, we applied the proposed algorithm to each blended image and computed distinct contrast values. A quantitative measure of contrast improvement was defined by a contrast improvement index (CII) [9, 74]:

$$CII = \frac{C_t^{processed}}{C_t^{original}},$$

where $C_t^{processed}$ and $C_t^{original}$ are the contrast values for a region of interest in the processed and original images, respectively.

We compared our results with those of three existing contrast enhancement techniques: contrast stretching (CS), unsharp masking (UM), and histogram equalization (HE), as shown in Table 8-10. From these results, we observe that the values of CII depend on the image itself, the types of features and the surroundings context of the features. The contrast stretching and unsharp masking methods consistently had a little improvement over the original image, while the histogram equalization approach had varied performance. Our algorithm consistently outperformed these other methods. Note that since masses have larger regions than those of microcalcifications and spicular lesions. Since we emphasized features at edges the mean values of the masses were less improved.

Table 8: Contrast Improvement Index for masses obtained by Contrast Stretching (CS), Unsharp Masking (UM), Histogram Equalization (HE), and proposed Coherent Features (CF) methods.

Case	CS	UM	HE	CF
1	1.2321	1.1538	0.3934	3.4121
2	1.2720	1.1627	0.5430	3.5911
3	1.2453	1.1370	1.1606	4.1997
4	1.2218	1.1109	0.6830	3.5410
5	1.2313	1.1125	0.2755	3.7025
6	1.2590	1.2214	2.3413	4.2358
7	1.2458	1.2080	3.0524	4.9465
8	1.2374	1.0895	0.9045	4.2415
9	1.3271	1.1393	1.7784	6.1136
10	1.2236	1.1569	0.8641	3.9763
11	1.2622	1.0887	1.2967	3.6320
12	1.2485	1.1150	3.7718	5.9985
13	1.2543	1.1119	1.1636	3.1344
14	1.2742	1.1809	2.5198	4.7512
15	1.2332	1.1084	2.0114	3.8008
16	1.2316	1.1533	0.9142	4.1431
17	1.2071	1.1520	0.1207	3.0553
18	1.2233	1.1074	2.4443	3.9690
19	1.2275	1.1273	2.0329	3.1121
20	1.2614	1.1678	1.9330	3.8542

2.3.5 Summary

An enhancement algorithm relying on multiscale wavelet analysis and extracting oriented information at each scale of analysis was investigated. The evolution of wavelet coefficients across scales characterized the local shape of irregular structures. Using oriented information to detect the features proved to be an effective method of enhancing complex and subtle structures of the breast. Steerable filters, rotated at arbitrary orientations reliably found visual cues within each spatial-frequency sub-band of an image. Coherence measure and dominant orientation clearly helped to discriminate features from complex surrounding tissue in mammograms.

Table 9: Contrast Improvement Index for microcalcifications obtained by Contrast Stretching (CS), Unsharp Masking (UM), Histogram Equalization (HE), and proposed Coherent Features (CF) methods.

Case	CS	UM	HE	CF
1	1.2510	2.0225	3.0738	8.0812
2	1.2855	1.9996	1.5135	8.8415
3	1.2811	1.9945	2.1976	9.0558
4	1.2204	1.9953	0.6681	6.1101
5	1.2322	1.9159	0.3781	6.5205
6	1.2703	1.9731	1.3389	7.8585
7	1.2335	1.9508	0.6793	6.5333
8	1.2394	2.0097	1.1124	7.7731
9	1.2636	1.7277	1.7397	6.5394
10	1.2280	2.1050	0.8854	5.8531
11	1.3195	1.7763	1.5760	6.1981
12	1.2354	1.9701	2.0045	6.8729
13	1.2938	2.1740	3.4047	6.1026
14	1.2404	1.9956	0.1757	7.3612
15	1.2840	2.1781	1.0409	5.8868
16	1.2452	1.9345	2.1372	6.6954
17	1.2438	1.9107	0.9802	6.4960
18	1.2246	1.9772	2.3434	6.5619
19	1.2299	1.9302	2.1773	6.3651
20	1.2308	1.9459	1.0755	5.9010

Table 10: Contrast Improvement Index for spicular lesions obtained by Contrast Stretching (CS), Unsharp Masking (UM), Histogram Equalization (HE), and proposed Coherent Features (CF) methods.

Case	CS	UM	HE	CF
1	1.2576	1.5373	3.5718	6.4958
2	1.3016	1.6564	1.5741	8.9896
3	1.2709	1.6748	1.5917	9.0420
4	1.2647	2.1918	2.6259	14.8793
5	1.2397	1.5258	1.0526	6.4616
6	1.2508	1.5366	1.5741	6.4331
7	1.2432	1.5318	2.1020	6.4341
8	1.2837	1.7600	1.1114	11.1680
9	1.3500	1.6194	1.0969	10.5974
10	1.2203	1.6627	0.6285	7.1692
11	1.2498	1.6466	1.7991	7.1298
12	1.2654	1.6334	2.1535	8.9059
13	1.2835	1.6544	1.0977	5.4763
14	1.2495	1.6130	0.6353	7.8101
15	1.2860	1.7091	1.0337	5.3742
16	1.2332	1.6502	1.1970	7.2288
17	1.3066	1.4405	1.6293	6.3881
18	1.2135	1.5815	0.8470	6.2905
19	1.2527	1.5995	3.1518	7.1808
20	1.2478	1.6107	3.3187	6.1226

2.4 A Lifting Algorithm for Overcomplete Wavelet Representations for Interactive Feature Analysis

2.4.1 Introduction

In this section we first review the basic idea behind the lifting scheme introduced by Wim Sweldens [75] [76] as a flexible tool for constructing compactly supported biorthogonal wavelets. We study in Section 2.4.2 the properties of second generation wavelets that emerged from the need of more general basis functions in some applications on general domains. In Section 2.4.3, we review the biorthogonal wavelets and duals to see how they are related each other to satisfy a perfect reconstruction condition in a filter bank coding system. In Section 2.4.4 we describe the mathematical background of the lifting scheme and its definition. We then discuss in Section 2.4.5 the relation between interpolating scaling functions and the lifting scheme. In Section 2.4.6 we show how this lifting scheme can be generalized to construct any wavelet or wavelet transforms with a finite number of lifting steps [77]. Finally, in Section 2.4.7 we introduce an *overcomplete lifting scheme* that can enhance the performance of the wavelet processing via overcomplete representations.

2.4.2 Second Generation Wavelets

Wavelets $\psi_{j,k}$ are traditionally defined by translates and dilates of one particular function, a *mother* wavelet ψ, such that $\psi_{j,k}(x) = \psi(a^j x - k)$. These wavelets are referred to as first generation wavelets. The properties of first generation wavelets are the following: They form a Riesz basis for $\mathbf{L}_2(\mathbf{R})$, so that a function f in $\mathbf{L}_2(\mathbf{R})$ can be represented with the wavelet basis $\{\psi_{j,k}\}$ as

$$f = \sum_{j,k} \gamma_{j,k} \psi_{j,k},$$

where the coefficients $\gamma_{j,k}$ are computed by $\gamma_{j,k} = \langle f, \tilde{\psi}_{j,k} \rangle$. $\tilde{\psi}$ is a dual wavelet of ψ. The wavelets and their duals are well localized in space and frequency. In other words, the wavelets and duals have compact supports, which are smooth, i.e. they decay towards high frequencies, and have vanishing polynomial moments, which decay toward low frequency. Wavelets are also utilized in a framework of multiresolution analysis. Finally, they mostly rely on the Fourier transform as a basic instrumental tool since the operations of the wavelet family defined by translates and dilates become algebraic operations in Fourier space.

On top of the properties of the traditional wavelets, second generation wavelets have emerged from the need of more generalized analyzing functions which are not necessarily translates and dilates of one basis function. Some applications on general domains require

wavelets that are defined on arbitrary, possibly non-smooth, domains of $\mathbf{R^n}$. A special case is the construction of wavelets on bounded domains without introducing end effects near boundaries. We also need wavelets to analyze data on curves, surfaces or manifolds independent of parametrization. There are also problems in real life to analyze irregularly sampled data, which can not be achieved by first generation wavelets and traditional wavelet transform algorithms.

Because of the non-translation invariant property of its basis functions, second generation wavelets can no longer use the Fourier transform as its construction tool. A question arises: How may second generation wavelets be constructed? The lifting scheme introduced by Wim Sweldens [75] [76] provides a profound answer. The scheme was initially introduced as a tool in constructing biorthogonal wavelets. Daubechies and Sweldens [77] later generalized the lifting scheme for the construction of any wavelet by factoring wavelet transforms through finite lifting steps. In the next section we first study the properties of the biorthogonal wavelets and duals which is the first footstone in developing the lifting scheme.

2.4.3 Biorthogonal Wavelets and Duals

The orthogonality property in wavelets imposes a strong limitation in the construction of wavelets. The Haar wavelet is the only real-valued wavelet which is compactly supported, orthogonal and symmetric [78]. The scaling function $\varphi \in \mathbf{L_2}$, and the wavelet function $\psi \in \mathbf{L_2}$ both contribute to a multiscale analysis and must satisfy the refinement relations in the sense that,

$$\varphi(x) = 2\sum_k h_k \varphi(2x-k) ,$$

$$\psi(x) = 2\sum_k g_k \varphi(2x-k) .$$

(2.1)

The set of translated scale functions $\{\varphi(x-k)|k \in Z\}$ form a Riesz basis. The refinement relations are also applicable to their duals: $\tilde{\varphi}$ and $\tilde{\psi}$, with coefficients $\tilde{h}_k$ and $\tilde{g}_k$ respectively, such that

$$\tilde{\varphi}(x) = 2\sum_k \tilde{h}_k \tilde{\varphi}(2x-k) ,$$

$$\tilde{\psi}(x) = 2\sum_k \tilde{g}_k \tilde{\varphi}(2x-k) .$$

(2.2)

These duals also fit into a framework of multiresolution analysis. The duals are biorthogonal to their primals in the sense that,

$$\langle \tilde{\varphi}(x), \psi(x-k) \rangle = \langle \tilde{\psi}(x), \varphi(x-k) \rangle = 0 \,,$$
$$\langle \tilde{\varphi}(x), \varphi(x-k) \rangle = \langle \tilde{\psi}(x), \psi(x-k) \rangle = \delta_k \,. \tag{2.3}$$

The biorthogonality condition (2.3) is equivalent to

$$\sum_k \hat{\tilde{\varphi}}(\omega + 2k\pi) \overline{\hat{\varphi}(\omega + 2k\pi)} = \sum_k \hat{\tilde{\psi}}(\omega + 2k\pi) \overline{\hat{\psi}(\omega + 2k\pi)} = 1,$$
$$\sum_k \hat{\tilde{\psi}}(\omega + 2k\pi) \overline{\hat{\varphi}(\omega + 2k\pi)} = \sum_k \hat{\tilde{\varphi}}(\omega + 2k\pi) \overline{\hat{\psi}(\omega + 2k\pi)} = 0. \tag{2.4}$$

Combining the condition (2.3) or (2.4) and the refinement relation (2.1), we can derive a biorthogonal condition for FIR filters, h, g, $\tilde{h}$, and $\tilde{g}$, as

$$\tilde{h}(\omega)\overline{h(\omega)} + \tilde{h}(\omega + \pi)\overline{h(\omega + \pi)} = 1$$
$$\tilde{g}(\omega)\overline{g(\omega)} + \tilde{g}(\omega + \pi)\overline{g(\omega + \pi)} = 1$$
$$\tilde{g}(\omega)\overline{h(\omega)} + \tilde{g}(\omega + \pi)\overline{h(\omega + \pi)} = 0$$
$$\tilde{h}(\omega)\overline{g(\omega)} + \tilde{h}(\omega + \pi)\overline{g(\omega + \pi)} = 0 \,, \tag{2.5}$$

or equivalently in matrix notation,

$$\begin{bmatrix} \tilde{h}(\omega) & \tilde{h}(\omega + \pi) \\ \tilde{g}(\omega) & \tilde{g}(\omega + \pi) \end{bmatrix} \begin{bmatrix} \overline{h(\omega)} & \overline{g(\omega)} \\ \overline{h(\omega + \pi)} & \overline{g(\omega + \pi)} \end{bmatrix} = \begin{bmatrix} 1 & 0 \\ 0 & 1 \end{bmatrix}. \tag{2.6}$$

Hence, if we denote modulation matrices, $m(\omega)$ and $\tilde{m}(\omega)$, respectively by

$$m(\omega) = \begin{bmatrix} h(\omega) & h(\omega + \pi) \\ g(\omega) & g(\omega + \pi) \end{bmatrix} \quad \text{and} \quad \tilde{m}(\omega) = \begin{bmatrix} \tilde{h}(\omega) & \tilde{h}(\omega + \pi) \\ \tilde{g}(\omega) & \tilde{g}(\omega + \pi) \end{bmatrix} \,,$$

then, the biorthogonality condition (2.6) becomes

$$\forall \omega \in \mathbf{R}, \quad \tilde{m}(\omega)\overline{m^t(\omega)} = I \,. \tag{2.7}$$

By transposing equation (2.6), we see that

$$\overline{h(\omega)}\tilde{h}(\omega) + \overline{g(\omega)}\tilde{g}(\omega) = 1$$
$$\overline{h(\omega)}\tilde{h}(\omega + \pi) + \overline{g(\omega)}\tilde{g}(\omega + \pi) = 0. \tag{2.8}$$

Equation (2.8) can also be driven by a general two channel subband coding scheme shown in Figure 42. A discrete input signal $s(n)$ is decomposed into an approximation signal $a(n)$ and a detail signal $d(n)$. They are defined by
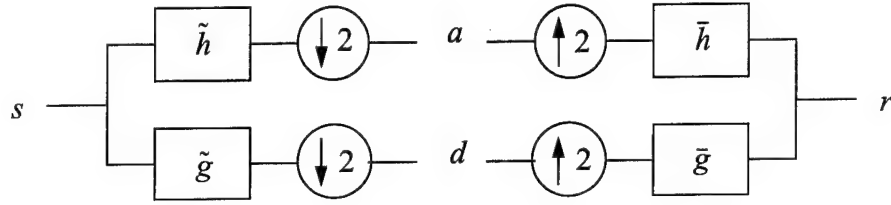
Figure 42. A two channel subband coding scheme.

$$a(2\omega) = \frac{1}{2}(\tilde{h}(\omega)s(\omega) + \tilde{h}(\omega + \pi)s(\omega + \pi)),$$

$$d(2\omega) = \frac{1}{2}(\tilde{g}(\omega)s(\omega) + \tilde{g}(\omega + \pi)s(\omega + \pi)).$$

(2.9)

The reconstructed signal in the frequency domain can be written by

$$r(\omega) = \alpha(\omega)s(\omega) + \beta(\omega)s(\omega + \pi),$$

(2.10)

where

$$\alpha(\omega) = \overline{h(\omega)}\tilde{h}(\omega) + \overline{g(\omega)}\tilde{g}(\omega),$$

$$\beta(\omega) = \overline{h(\omega)}\tilde{h}(\omega + \pi) + \overline{g(\omega)}\tilde{g}(\omega + \pi).$$

(2.11)

In order to achieve perfect reconstruction in the subband coding system, we keep only the linear shift-invariant (LSI) system response appearing in the first term of equation (2.10) and cancel out the system aliasing in the second term of equation (2.10). From $\alpha(\omega) = 1$ and $\beta(\omega) = 0$, we can derive equation (2.8).

By applying Cramer's rule to (2.8), we observe that

$$\tilde{h}(\omega) = \frac{\overline{g(\omega + \pi)}}{D_m(\omega)}, \quad \text{and} \quad \tilde{g}(\omega) = -\frac{\overline{h(\omega + \pi)}}{D_m(\omega)},$$

(2.12)

where $D_m(\omega) = \det m(\omega)$. In the case of finite filters, we need to restrict $D_m(\omega)$ to be a monomial, and we choose

$$D_m(\omega) = -e^{-i\omega}.$$

(2.13)

By applying equation (2.13) to equations (2.12) and (2.8), we have

101

$$\tilde{g}(\omega) = -e^{-i\omega}\overline{h(\omega + \pi)} \quad \text{and} \quad g(\omega) = -e^{-i\omega}\overline{\tilde{h}(\omega + \pi)}, \tag{2.14}$$

and equation (2.8) becomes

$$\overline{h(\omega)}\tilde{h}(\omega) + \overline{h(\omega + \pi)}\tilde{h}(\omega + \pi) = 1. \tag{2.15}$$

The filters satisfying equation (2.15) are called conjugate filters.

After finding the conjugate filters, we can construct a scaling function. By the refinement relation (2.1), the Fourier transform of the scaling function is then defined by

$$\hat{\varphi}(\omega) = H\left(\frac{\omega}{2}\right)\hat{\varphi}\left(\frac{\omega}{2}\right), \tag{2.16}$$

where H is the Fourier transform of the finite filter h, in other words

$$H(\omega) = \sum_{n=-\infty}^{\infty} h(n)e^{-in\omega}.$$

Since $\hat{\varphi}(0) = 1$, infinite iterations of (2.16) with a conjugate filter H satisfying (2.15) yields the limiting scaling function

$$\hat{\varphi}(\omega) = \prod_{j=1}^{\infty} H(2^{-j}\omega). \tag{2.17}$$

A similar statement holds for the dual scaling function $\tilde{\varphi}$ and its associated dual filter $\tilde{H}$. Since the properties of the filter H determine the properties of the scaling function such as the smoothness and its asymtotic decay at infinity, we do not need the scaling function itself in many applications, rather we directly work with the finite filter H.

Figure 43 shows the limiting process to make the Daubechies's four tab scaling function. Each figure shown in Figure 43 shows scaling functions without iteration, after one iteration, after ·two iterations and after fifteen iterations, respectively, from top to bottom. Figure 44 displays a graph of mean square errors involved in the limiting steps to make the Daubecies's four tap scaling function. The limiting process makes little difference after fifteen iterations (RMS $< 2.24e^{-16}$).

As pointed out in [79], useful analyzing properties such as oscillations, and moments can be concentrated on the $\tilde{\psi}$ whereas the synthesis properties such as regularity are determined by ψ. $\tilde{\psi}$ and ψ can have very different regularity properties, however in practice, ψ is much more regular than $\tilde{\psi}$ [16]. In other words, analyzing dual wavelets have more vanishing moments than synthesizing wavelets.
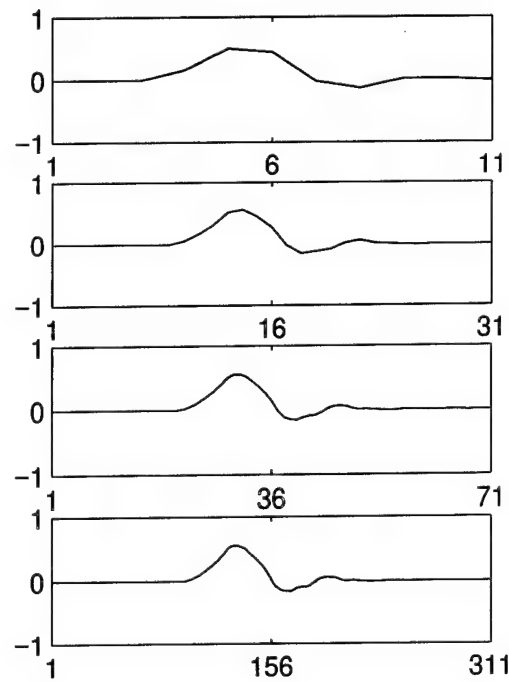
Figure 43. Graph showing the limiting process to make the Daubechies tap 4 scaling function. From top to bottom, scaling functions without iteration, after one iteration, after two iterations, and after fifteen iterations, respectively.
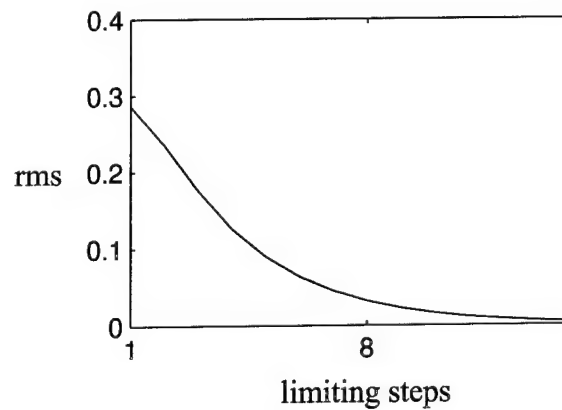

Figure 44. Graph of root mean square errors involved in the limiting steps to make the Daubechies tap 4 scaling function shown in Figure 43.

2.4.4 Lifting Scheme

We recall the Vetterli-Herley lemma [80] which defines a complete characterization of filters, $\tilde{h}$ and $\tilde{h}^{old}$, biorthogonal to a given filter, h. The two dual filters $\tilde{h}$ and $\tilde{h}^{old}$ are biorthogonal to h in the sense of (2.15), and are related by

$$\tilde{h}(\omega) = \tilde{h}^{old} + e^{-i\omega}\overline{h(\omega + \pi)s(2\omega)}, \qquad (2.18)$$

where $s(\omega)$ is a trigonometric polynomial. In other words, if one of the dual filters is biorthogonal to h, and they are related through (2.18), the other dual is biorthogonal to h as well [75]. By combining the biorthogonal condition for basis functions (2.4) and (2.18), we can show the following relation for the associated FIR filters. From an initial set of finite biorthogonal filters $\{h, \tilde{h}^{old}, g^{old}, \tilde{g}\}$, a new set of finite biorthogonal filters can be found by

$$\tilde{h}(\omega) = \tilde{h}^{old}(\omega) + \tilde{g}(\omega)\overline{s(2\omega)}$$
$$g(\omega) = g^{old}(\omega) - h(\omega)s(2\omega). \qquad (2.19)$$

This is called *lifting* and this operation leads to the lifting scheme. Primal and dual basis functions with lifting are then given by:

$$\varphi(x) = \varphi^{old}(x)$$
$$\tilde{\varphi}(x) = 2\sum_k \tilde{h}_k^{old} \tilde{\varphi}(2x-k) + \sum_k s_{-k}\tilde{\psi}(x-k)$$
$$\psi(x) = \psi^{old}(x) - \sum_k s_k\varphi(x-k) \qquad (2.20)$$
$$\tilde{\psi}(x) = 2\sum_k \tilde{g}_k^{old} \tilde{\varphi}(2x-k).$$

There are several facts notable in (2.20). The scaling function does not change after lifting. The wavelet after lifting uses the scaling function at the same level. The wavelet construction formula tells us that the property of the wavelet after lifting is mostly determined by the property of the trigonometric polynomial s. The dual wavelet also changes. However since the changes in the dual wavelets are from the changes in the dual scaling functions, the changes of the dual wavelet are not meaningful by themselves. To summarize, the lifting algorithm contributes to some fundamental and meaningful changes in the wavelet and the dual scaling functions through s which defines the true power of the lifting scheme. In other words, a multiresolution analysis can be achieved by starting from a simple basis function and building a more performant one with desirable properties.

We can also define a dual lifting from an initial set of filters $\{h^{old}, \tilde{h}, g, \tilde{g}^{old}\}$ and a dual

lifting polynomial $\tilde{s}$ such that

$$h(\omega) = h^{old}(\omega) + g(\omega)\overline{\tilde{s}(2\omega)}$$

$$\tilde{g}(\omega) = \tilde{g}^{old}(\omega) - \tilde{h}(\omega)\tilde{s}(2\omega) .$$

(2.21)

The dual lifting scheme is thus defined by simply toggling the tildes in (2.20) as

$$\tilde{\varphi}(x) = \tilde{\varphi}^{old}(x)$$

$$\varphi(x) = 2\sum_k h_k^{old} \varphi(2x-k) + \sum_k \tilde{s}_{-k}\psi(x-k)$$

$$\tilde{\psi}(x) = \tilde{\psi}^{old}(x) - \sum_k \tilde{s}_k \tilde{\varphi}(x-k)$$

$$\psi(x) = 2\sum_k g_k^{old}\varphi(2x-k) .$$

(2.22)

By alternating the primal and dual lifting scheme, one can come up with a multiresolution analysis geared for specific properties. This so-called *cakewalk* algorithm leads to a canonical form of the wavelet transform shown in Figure 45. Here the filters followed by successive subsampling define the *Lazy* wavelet transform which simply splits an original signal into odd and even subsets. The dual lifting predicts wavelet coefficients with the help of the scaling function coefficients based upon the correlation present in the finer signal. The primal lifting then updates the scaling function coefficients using the previously predicted wavelet coefficients to remove possible aliasing resulting from downsampling.

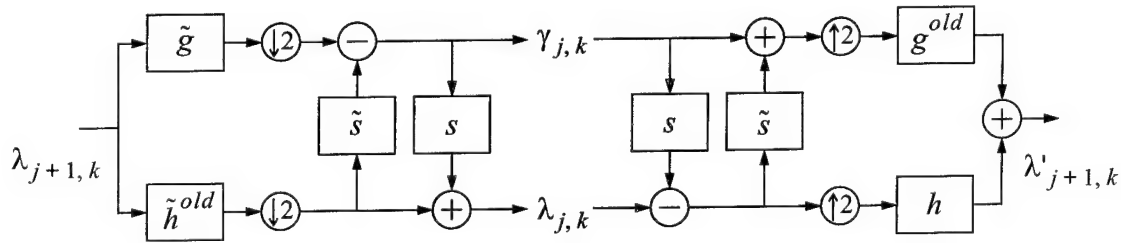Based upon the formulae of the primal and dual lifting schemes, a fast forward and inverse

Figure 45. A 1-D discrete wavelet transform with lifting polynomials.

wavelet transform can thus be formulated as

FORWARD TRANSFORM

(I) $\lambda_{j,l} = \sqrt{2}\sum_k \tilde{h}^{old}_{k-2l}\lambda_{j+1,k}$ and $\gamma_{j,l} = \sqrt{2}\sum_k \tilde{g}_{k-2l}\lambda_{j+1,k}$,

(II) $\gamma_{j,l} = \gamma_{j,l} - \sum_{k}^{N-1} \tilde{s}_{l-k}\lambda_{j,k}$

(III) $\lambda_{j,l} = \lambda_{j,l} + \sum_{k}^{\tilde{N}-1} s_{l-k}\gamma_{j,k}$

INVERSE TRANSFORM

(I) $\lambda_{j,l} = \lambda_{j,l} - \sum_{k}^{\tilde{N}-1} s_{l-k}\gamma_{j,k}$

(II) $\gamma_{j,l} = \gamma_{j,l} + \sum_{k}^{N-1} \tilde{s}_{l-k}\lambda_{j,k}$

(III) $\lambda_{j+1,k} = \sqrt{2}\sum_l h_{k-2l}\lambda_{j,l} + \sqrt{2}\sum_l g^{old}_{k-2l}\gamma_{j,l}$.

Here N and $\tilde{N}$ are the orders of the primal and dual lifting polynomials defined as s and $\tilde{s}$ respectively.

Now we can define a canonical implementation structure of the lifting scheme with three stages: *split*, *predict* and *update*, which is well described in the *cakewalk* algorithm shown in Figure 45. A simpler version of the forward wavelet transform with lifting is shown in Figure 46. The split process splits the input data $\{\lambda_{j+1}\}$ into two smaller subsets $\{\lambda_j\}$ and $\{\gamma_j\}$. From the perfect reconstruction property in the polyphase representation, the most trivial subsets are even and odd samples. This is often referred to as the *Lazy* wavelet transform [75] as described earlier. In the second stage *Predict*, we try to use the $\{\lambda_j\}$ subset to predict the $\{\gamma_j\}$ subset based on the correlation present in the original data. The $\{\lambda_j\}$ subset is then *lifted* with the help of the wavelet coefficients $\{\gamma_j\}$. The idea is to find a better $\{\lambda_j\}$ so that a certain scalar quantity $Q()$, such as the mean is preserved, $Q(\lambda_{j+1}) = Q(\lambda_j)$. These aspects lead to the following forward wavelet transform:
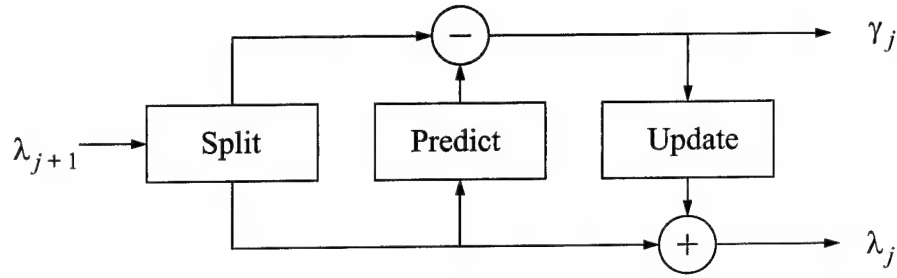
Figure 46. Canonical structure in implementing 1-D discrete forward wavelet transform with lifting.

$$\text{For } j = -1 \text{ downto} - n: \begin{cases} \{\lambda_j, \gamma_j\} = Split(\lambda_{j+1}) \\ \gamma_j = \gamma_j - \mathcal{P}(\lambda_j) \\ \lambda_j = \lambda_j + \mathcal{U}(\gamma_j), \end{cases}$$

where $\mathcal{P}$ and $\mathcal{U}$ are prediction and update operators, respectively. The inverse transform is immediately driven by reversing the operations and toggling the signs:

$$\text{For } j = -n \text{ upto} - 1: \begin{cases} \lambda_j = \lambda_j - \mathcal{U}(\gamma_j) \\ \gamma_j = \gamma_j + \mathcal{P}(\lambda_j) \\ \lambda_{j+1} = Join(\lambda_j, \gamma_j). \end{cases}$$

Figure 47 shows the wavelet representation with lifting after level 1 decomposition. The wavelet transform presented here in fact is the ($N = 2$, $\tilde{N} = 2$) biorthogonal wavelet transform of Cohen-Daubechies-Feauveau [79].

2.4.5 Interpolating Scaling Functions and Associated Wavelets

Sweldens [75] [76] [81] showed that the lifting scheme described in the previous section is connected with interpolating scaling functions. The use of interpolating scaling functions in multiresolution analysis has been studied by several authors [82] [83]. The main advantage of the interpolating scaling function is that the coefficients λ_k in a function expansion

$$f(x) = \sum_k \lambda_k \varphi(x-k)$$

can be easily obtained from $\lambda_k = f(k)$ since the interpolating scaling function is defined as
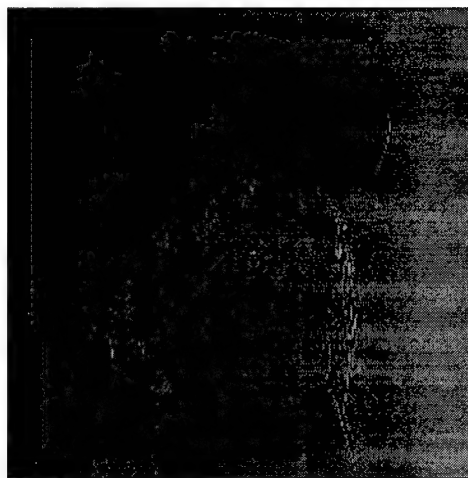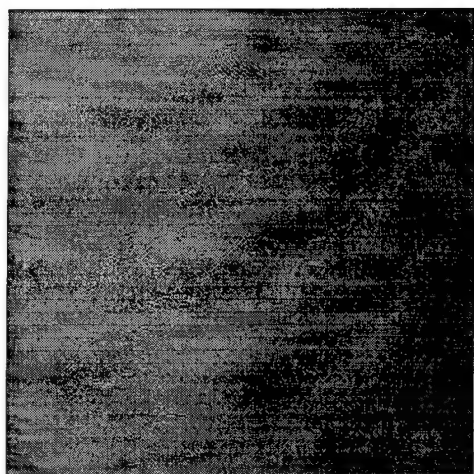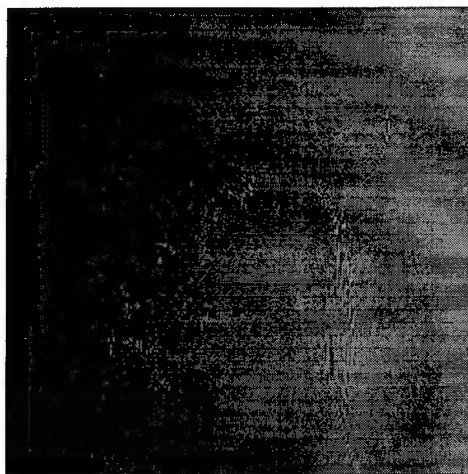
Figure 47. Wavelet representation with lifting after level 1 decomposition. (a), (b), (c) and (d) show DC component, wavelet coefficients processed in the vertical direction, in the horizontal direction and in the diagonal direction, respectively.

$\varphi(k) = \delta_k$ for all $k \in \mathbf{Z}$. By combining the definition of the interpolating scaling function and the refinement relation (2.1), we get $h_{2k} = \delta_k/2$ which becomes

$$h(\omega) + h(\omega + \pi) = 1. \tag{2.23}$$

Filters satisfying (2.23) is called interpolating filters. *à-trous* filters are the interpolating filters which are used to compute coefficients of a continuous wavelet transform [84] [66].

There have been several approaches to compute interpolating scaling functions. Here we briefly discuss one proposed by Deslauriers and Dubuc [82]: *interpolating subdivision*, which is connected to our *Overcomplete Lifting Scheme*. The interpolating subdivision is formally defined as follows. We first construct a polynomial P of degree N-1 so that $P(x_{j,k+l}) = \lambda_{j,k+l}$ for $-D + 1 \le l \le D$, where $N = 2D$. We then calculate coefficients on the next finer level as the value of this polynomial by $\lambda_{j+1,2k+1} = P(x_{j+1,2k+1})$. Figure 48 shows the scaling functions with interpolating subdivision of order 2, 4, 6, and 8 from top to bottom.

These interpolating scaling functions have compact supports, and are symmetric, so that a $\varphi(x)$ is zero outside the interval $[-N + 1, N - 1]$. The subdivision interpolating scaling functions and their translates reproduce polynomials up to degree $N - 1$. They also satisfy the
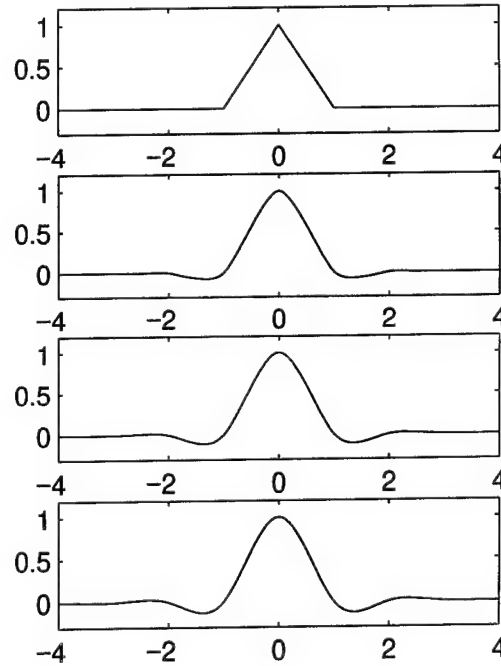
Figure 48. Interpolating scaling functions resulted from the interpolating subdivision of order 2, 4, 6 and 8 from top to bottom.

refinement equation (2.1), which is critical in defining a multiresolution analysis. Since the order of the reproduced polynomials is invariant within an interval, the resulting scaling functions are well adapted on an interval of finite signal without extensions such as zero padding, periodization or reflection. Figure 49 shows an example of cubic ($N=4$) scaling functions changing their shapes to accommodate themselves near the left boundary without degrading the regularity. The interpolation properties previously described are still preserved well on the boundary for this scaling function.

Table 2-1 lists the lifting coefficients needed for the interpolating subdivision scheme which are computed from *Neville*'s algorithm. Table 2-1(a), (b), (c) and (d) show the filter coefficients for $N=2$, $N=4$, $N=6$ and $N=8$, respectively. Each lists all coefficients to compute values at every possible location newly introduced as a middle point at the next finer level.

By filling in the refinement relation in the interpolating case, we see that
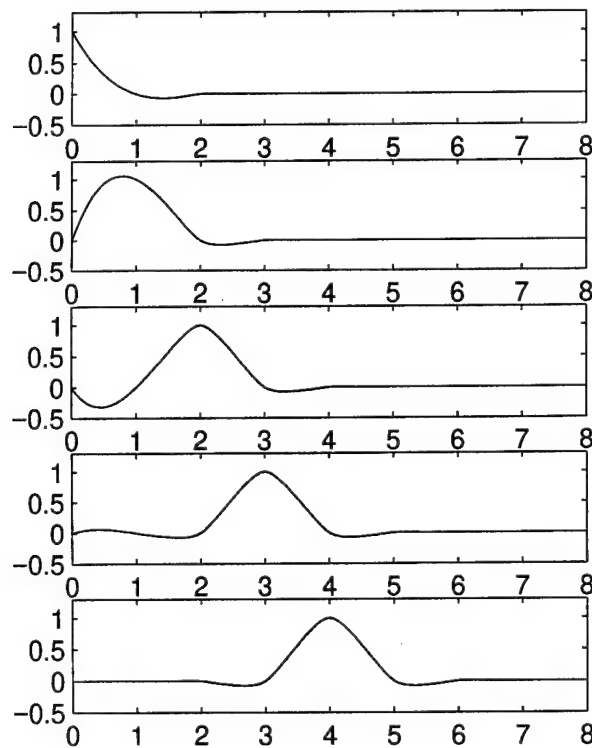
Figure 49. The cubic ($N=4$) interpolating scaling functions at k = 1, 2, 3, 4, and 5 (top to bottom) who change their shapes to alleviate boundary effects.

# of $\lambda's$ on (left, right)	Lifting Coefficients ($N = 2$)
(0, 2)	(-0.5, 1,5)
(1, 1)	(0.5, 0.5)
(2, 0)	(1.5, -0.5)

(a)

# of $\lambda's$ on (left, right)	Lifting Coefficients ($N = 4$)
(0, 4)	(2.1875, -2.1875, 1.3125, -0.3125)
(1,3)	(0.3125, 0.9375, -0.3125, 0.0625)
(2, 2)	(-0.0625, 0.5625, 0.5625, -0.0625)
(3, 1)	(0.0625, -0.3125, 0.9375, 0.3125)
(4, 0)	(-0.3125, 1.3125, -2.1875, 2.1875)

(b)

# of $\lambda's$ on (left, right)	Lifting Coefficients ($N = 6$)
(0, 6)	(2.7070, -4.5117, 5.4141, -3.8672, 1.5039, -0.2461)
(1,5)	(0.2461, 1.2305, -0.8203, 0.4922, -0.1758, 0.0273)
(2, 4)	(-0.0273, 0.4102, 0.8203, -0.2734, 0.0820, -0.0117)
(3, 3)	(0.0117, -0.0977, 0.5859, 0.5859, -0.0977, 0.0117)
(4, 2)	(-0.0117, 0.0820, -0.2734, 0.8203, 0.4102, -0.0273)
(5, 1)	(0.0273, -0.1758, 0.4922, -0.8203, 1.2305, 0.2461)
(6, 0)	(-0.2461, 1.5039, -3.8672, 5.4141, -4.5117, 2.7070)

(c)

# of $\lambda's$ on (left, right)	Lifting Coefficients ($N = 8$)
(0, 8)	(3.1421, -7.3315, 13.1968, -15.7104, 12.2192, -5.9985, 1.6919, -0.2095)
(1, 7)	(0.2095, 1.4663, -1.4663, 1.4663, -1.0474, 0.4888, -0.1333, 0.0161)
(2, 6)	(-0.0161, 0.3384, 1.0151, -0.5640, 0.3384, -0.1450, 0.0376, -0.0044)
(3, 5)	(0.0044, -0.0513, 0.4614, 0.7690, -0.2563, 0.0923, -0.0220, 0.0024)
(4, 4)	(-0.0024, 0.0239, -0.1196, 0.5981, 0.5981, -0.1196, 0.0239, -0.0024)
(5, 3)	(0.0024, -0.0220, 0.0923, -0.2563, 0.7690, 0.4614, -0.0513, 0.0044)
(6, 2)	(-0.0044, 0.0376, -0.1450, 0.3384, -0.5640, 1.0151, 0.3384, -0.0161)
(7, 1)	(0.0161, -0.1333, 0.4888, -1.0474, 1.4663, -1.4663, 1.4663, 0.2095)
(8, 0)	(-0.2095, 1.6919, -5.9985, 12.2192, -15.7104, 13.1968, -7.3315, 3.1421)

(d)

Table 2-1. Lifting coefficients based on the number of $\lambda's$ on its left and right. (a), (b), (c) and (d) show the filter coefficients for $N = 2$, $N = 4$, $N = 6$ and $N = 8$, respectively.

$$\delta_{k, k'} = \varphi_{j, k}(x_{j, k'}) = \sum_l h_{j, k, l} \varphi_{j+1, l}(x_{j+1, 2k'}) = h_{j, k, 2k'},$$

which can be written as

$$\varphi_{j, k} = \varphi_{j+1, 2k} + \sum_m h_{j, k, 2m+1} \varphi_{j+1, 2m+1}.$$

An approximation $A_j f$ from a finer one $A_{j+1} f$ is then built by simple subsampling, $\lambda_{j, k} = \lambda_{j+1, 2k}$, followed by one step subdivision on A_j:

$$A_j f = \sum_k \lambda_{j, k} \varphi_{j, k} = \sum_k \lambda_{j+1, 2k} \varphi_{j+1, 2k} + \sum_k \sum_m \lambda_{j, k} h_{j, k, 2m+1} \varphi_{j+1, 2m+1}$$

The detail, $A_{j+1} - A_j$, consists only of functions of the form $\varphi_{j+1, 2m+1}$. Thus the wavelets are given by $\psi_{j, m} = \varphi_{j+1, 2m+1}$. However, a necessary condition for the wavelets to form a Riesz basis is that the dual vanishing moment $\tilde{N}$ is at least one. A new wavelet with $\tilde{N}$ is then formulated by following with lifting scheme:

$$\psi_{j, m} = \varphi_{j+1, 2m+1} - \sum_{l=0}^{\tilde{N}-1} s_{j, m}^l \varphi_{j, m+l},$$

where the lifting coefficients $s_{j, m}^l$ are chosen so that

$$\int \psi_{j, m}(x) = 0, \int x \psi_{j, m}(x) = 0, \quad \dots \dots, \int x^{\tilde{N}-1} \psi_{j, m}(x) = 0.$$

In other words, the new wavelet is composed of the old wavelet, a subsampled scaling function located at odd indices, and its immediate neighboring scaling functions at the same scale j. Figure 50 shows wavelets with two dual vanishing moments, i.e. $\tilde{N} = 2$, associated with interpolating scaling functions the order of the subdivision of which are 2, 4, 6, and 8 from top to bottom. Figure 51 shows a wavelet accommodating the left boundary. The cubic ($N = 4$) scaling function was used to construct this wavelet with $\tilde{N} = 2$ vanishing moments.

2.4.6 Generalized Lifting Scheme

We have seen in the previous sections that there are many advantages of the lifting such as an in-place implementation of the fast wavelet transform, no need for the Fourier transform, easiness of the inverse transform, capability of custom-design of wavelets and adaptiveness of wavelet transforms. However the lifting scheme discussed was used in constructing biorthogonal wavelets. However can the lifting be used in constructing any wavelets or wavelet transforms with
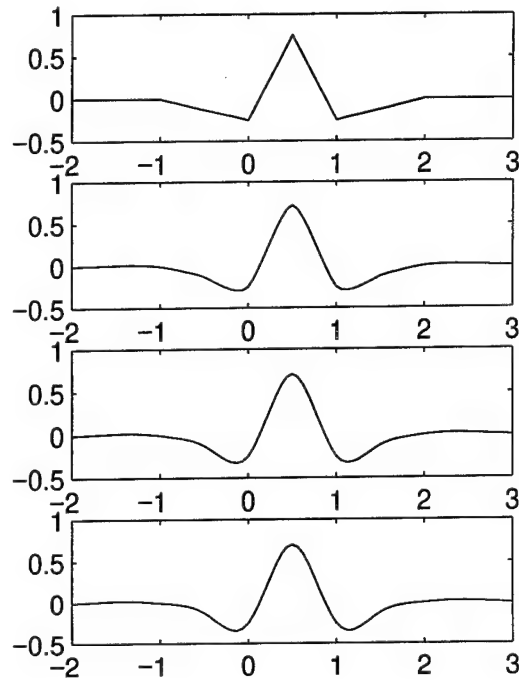
Figure 50. Wavelets with two dual vanishing moments ($\tilde{N} = 2$) associated with interpolating scaling functions whose orders of the subdivision are 2, 4, 6, and 8 from top to bottom.

finite filters? Daubechies and Sweldens addressed the generality of the lifting by connecting the Euclidean algorithm to a subband transform in the z-domain [77].

The z-transform of a FIR filter h is a Laurent polynomial $H(z)$ given by

$$H(z) = \sum_{k=a}^{b} h_k z^{-k}$$

where a and b are respectively the lower and upper bound of the support of the filter h. The degree of the Laurent polynomial $H(z)$ is given by $|H(z)| = b - a$, so that a polynomial Cz^l has zero degree and is a monomial, where C is a non-zero constant and l is an integer. A Laurent polynomial is invertible if and only if it is a monomial.

The monomial constraint plays a key role in finding a modulation matrix or a polyphase matrix in a filter bank coding system. Figure 52 shows a discrete wavelet transform in z-domain. The conditions for perfect reconstruction are given by

113
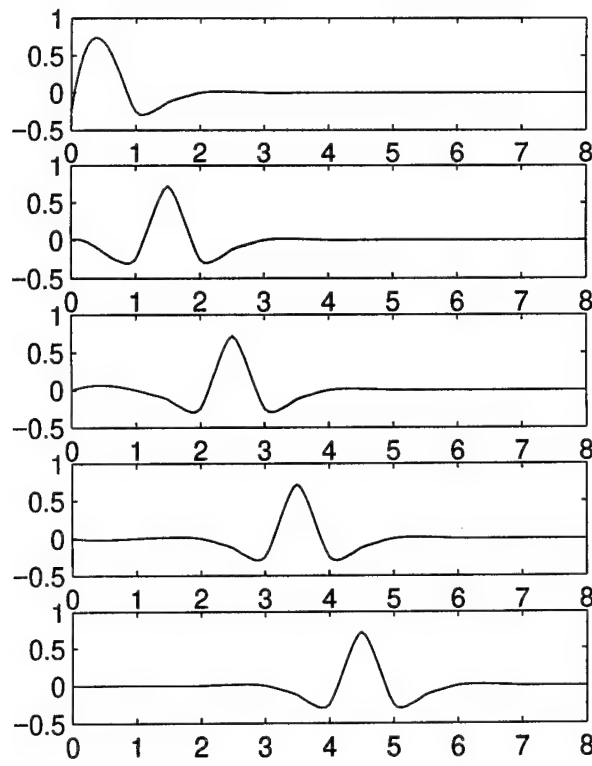
Figure 51. Wavelets accommodating the left boundary. Here, $N = 4$ and $\tilde{N} = 2$.
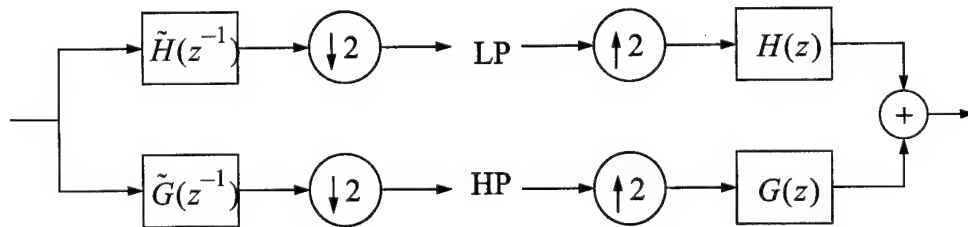
Figure 52. Discrete wavelet transform in z-domain.

$$H(z)\tilde{H}(z^{-1}) + G(z)\tilde{G}(z^{-1}) = 2,$$

$$H(z)\tilde{H}(-z^{-1}) + G(z)\tilde{G}(-z^{-1}) = 0.$$

(2.24)

The modulation matrices $M(z)$ and $\tilde{M}(z)$ are defined as

$$M(z) = \begin{bmatrix} H(z) & H(-z) \\ G(z) & G(-z) \end{bmatrix}, \quad \tilde{M}(z) = \begin{bmatrix} \tilde{H}(z) & \tilde{H}(-z) \\ \tilde{G}(z) & \tilde{G}(-z) \end{bmatrix}.$$

(2.25)

By using these modulation matrices, the perfect reconstruction condition (2.24) can be written as

$$\tilde{M}(-z^{-1})^t M(z) = 2I,$$

(2.26)

where I is the 2 by 2 identity matrix.

We can simplify the perfect reconstruction in the filter bank structure using a polyphase representation which provides an efficient and convenient tool. The polyphase implementation works on different phases separately. The input is separated into even and odd phases followed by subsampling. Then the separate phases of the filters act in parallel on the separate phases of the input. Figure 53 shows a polyphase representation of the wavelet transform shown in Figure 52. The polyphase representation of a filter H is given as $H(z) = H_e(z^2) + z^{-1}H_o(z^2)$, where H_e and H_o contain respectively the even and odd coefficients. If we denote the polyphase matrix $P(z)$ as

$$P(z) = \begin{bmatrix} H_e(z) & G_e(z) \\ H_o(z) & G_o(z) \end{bmatrix},$$

(2.27)

then the relation between the modulation matrix (2.25) and the polyphase matrix (2.27) becomes

Figure 53. Polyphase representation of the wavelet transform.

$$P(z^2) = \frac{1}{2}\begin{bmatrix} 1 & 1 \\ z & -z \end{bmatrix} M^t(z) = \frac{1}{2}\left(M(z)\begin{bmatrix} 1 & z \\ 1 & -z \end{bmatrix} \right)^t. \tag{2.28}$$

Now the perfect reconstruction property with modulation matrices (2.26) can be written in polyphase matrices as

$$P(z)\tilde{P}(z^{-1})^t = I. \tag{2.29}$$

From the invertible property of Laurent polynomials and (2.29), the determinant of $P(z)$ must be a monomial in z so that $P(z) = Cz^l$. In 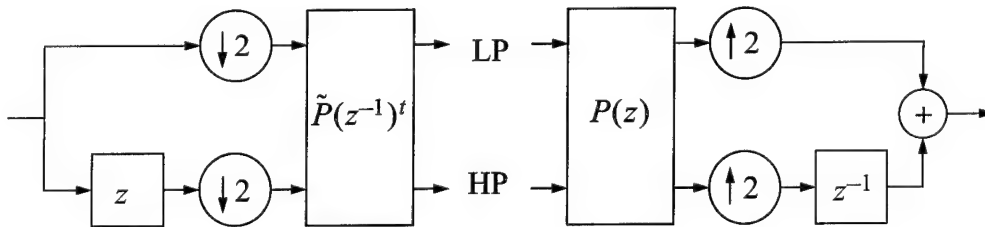other words, finding FIR filters for a wavelet transform becomes finding a polyphase matrix $P(z)$ with the determinant one. By combining this monomial property and (2.29), the dual polyphase matrix $\tilde{P}(z)$ is given as

$$\tilde{P}(z) = \begin{bmatrix} G_o(z^{-1}) & -H_o(z^{-1}) \\ -G_e(z^{-1}) & H_e(z^{-1}) \end{bmatrix}.$$

The most trivial case of the polyphase matrix satisfying the condition of perfect reconstruction is $P(z) = I$ which implies $H(z) = \tilde{H}(z) = 1$ and $G(z) = \tilde{G}(z) = z^{-1}$. The transform with $P(z) = I$ is often referred as the *Lazy* wavelet transform since it does nothing but separating the input into even and odd subsets.

Using the polyphase structure, the lifting given in (2.19) at page 104 can be written in z-domain as

$$\begin{aligned} \tilde{H}(z) &= \tilde{H}^{old}(z) + \overline{G(z)}S(z^{-2}) \\ G(z) &= G^{old}(z) - H(z)S(z^2), \end{aligned} \tag{2.30}$$

and the dual lifting in (2.21) at page 105 as

$$\begin{aligned} H(z) &= H^{old}(z) + \overline{G(z)}\tilde{S}(z^{-2}) \\ \tilde{G}(z) &= \tilde{G}^{old}(z) - \tilde{H}(z)\tilde{S}(z^2). \end{aligned} \tag{2.31}$$

There are two *noble identities* for a decimator and interpolator. In most applications a decimator is preceded by a bandlimiting filter $H(z)$ to avoid aliasing. An interpolation filter, on the other hand, is followed by an interpolator to eliminate imaging effect. Figure 54 shows equivalent identity systems. In Figure 54(a), we have a decimator followed by a transfer function $F(z)$. This cascade is equivalent to the one in the right provided $F(z)$ is a rational transfer function, i.e. a ratio of polynomials in z^{-1}. In Figure 54(b), we show that the two cascades in the left and right are equivalent for a interpolator. Based on the property of the noble identities with $M = 2$ and $L = 2$, the polyphase components of $H(z)S(z^2)$ are $H_e(z)S(z)$ for even and

116

$H_o(z)S(z)$ for odd. The new polyphase matrix after primal lifting is thus given by

$$P(z) = P^{old}(z) \begin{bmatrix} 1 & -S(z) \\ 0 & 1 \end{bmatrix}, \tag{2.32}$$

and the dual polyphase matrix by

$$\tilde{P}(z) = \tilde{P}^{old}(z) \begin{bmatrix} 1 & 0 \\ S(z^{-1}) & 1 \end{bmatrix}. \tag{2.33}$$

Similarly, the new polyphase matrix after dual lifting is given as

$$P(z) = P^{old}(z) \begin{bmatrix} 1 & 0 \\ \tilde{S}(z) & 1 \end{bmatrix}, \tag{2.34}$$

and the dual polyphase matrix as

$$\tilde{P}(z) = \tilde{P}^{old}(z) \begin{bmatrix} 1 & -\tilde{S}(z^{-1}) \\ 0 & 1 \end{bmatrix}. \tag{2.35}$$

The Euclidean algorithm developed to find the greatest common devisor (GCD) of two natural numbers can be extended to find a GCD of two Laurent polynomials [77]. In other words, two Laurent polynomials $A(z)$ and $B(z)$ are presented as

$$\begin{bmatrix} A(z) \\ B(z) \end{bmatrix} = \prod_{i=1}^{n} \begin{bmatrix} Q_i(z) & 1 \\ 1 & 0 \end{bmatrix} \begin{bmatrix} A_n(z) \\ 0 \end{bmatrix} \tag{2.36}$$

(a)

(b)
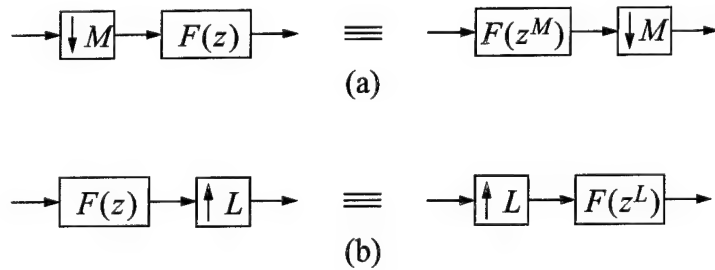
Figure 54. Noble identities for multirate systems. Identity systems for (a) a decimator and (b) an interpolator.

where $A_n(z)$ is the GCD, n is the smallest number for which $B_n(z) = 0$, and $Q_i(z) = A_{i-1}(z)/B_{i-1}(z)$. Here if $A_n(z)$ is a monomial, then $A(z)$ and $B(z)$ are relatively prime. We can always choose the quotients $Q_i(z)$ so that the GCD $A_n(z)$ is a constant.

By applying the Euclidean algorithm to polyphase matrices, we can factor any pair of complementary filters $(H(z), G(z))$ into lifting steps. A filter pair $(H(z), G(z))$ is defined to be *complementary* if the determinant of the corresponding polyphase matrix $P(z)$ is one. The polyphase matrix can be given as

$$P(z) = \left(\prod_{i=1}^{m} \begin{bmatrix} 1 & -S_i(z) \\ 0 & 1 \end{bmatrix} \begin{bmatrix} 1 & 0 \\ \tilde{S}_i(z) & 1 \end{bmatrix} \right) \begin{bmatrix} K & 0 \\ 0 & \dfrac{1}{K} \end{bmatrix}, \tag{2.37}$$

and the dual polyphase matrix as

$$\tilde{P}(z) = \left(\prod_{i=1}^{m} \begin{bmatrix} 1 & 0 \\ S_i(z^{-1}) & 1 \end{bmatrix} \begin{bmatrix} 1 & -\tilde{S}_i(z^{-1}) \\ 0 & 1 \end{bmatrix} \right) \begin{bmatrix} \dfrac{1}{K} & 0 \\ 0 & K \end{bmatrix}. \tag{2.38}$$

Here K is a non-zero constant, and $m = \dfrac{n}{2} + 1$. The polyphase matrix for analysis filter bank $\tilde{P}(z^{-1})^t$ is thus written as

$$\tilde{P}(z^{-1})^t = \begin{bmatrix} \dfrac{1}{K} & 0 \\ 0 & K \end{bmatrix} \left(\prod_{i=m}^{1} \begin{bmatrix} 1 & 0 \\ -\tilde{S}_i(z) & 1 \end{bmatrix} \begin{bmatrix} 1 & S_i(z) \\ 0 & 1 \end{bmatrix} \right). \tag{2.39}$$

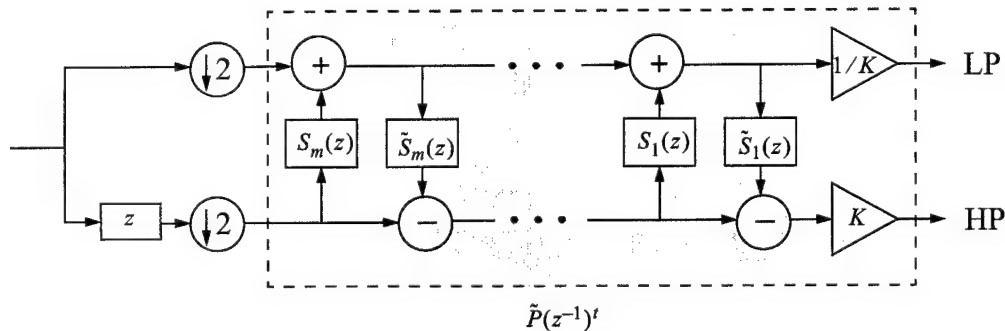Figure 55 shows the forward wavelet transform using the dual polyphase matrix with finite

Figure 55. Forward wavelet transform using a dual polyphase matrix $\tilde{P}(z^{-1})^t$ with finite number of lifting steps.

118
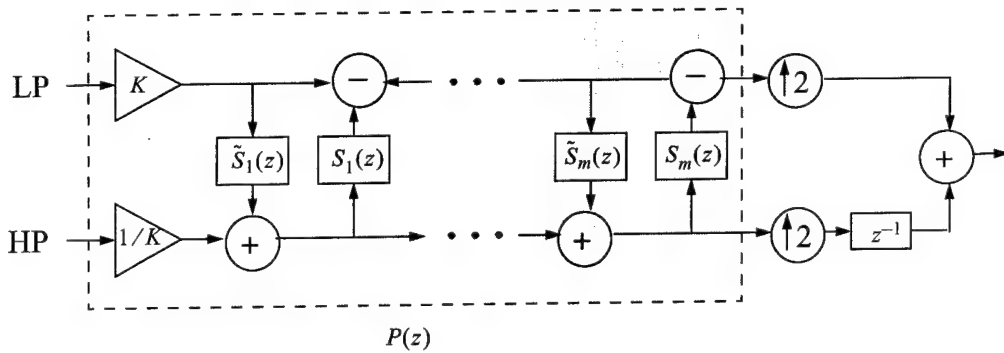
Figure 56. Inverse wavelet transform using the polyphase matrix $P(z)$ with finite number of lifting steps.

lifting steps given in (2.39). Figure 56 represents the finite steps of the inverse wavelet transform using the polyphase matrix representation in (2.37).

Every wavelet or wavelet transform can thus be obtained with a factorization of the polyphase matrix representation of the filter bank by means of Euclidean algorithm.

2.4.7 Overcomplete lifting scheme

In this section we propose an *overcomplete lifting scheme* which provides a framework for multiscale analysis with overcomplete wavelet representations. As described in the previous chapter, the lifting scheme is a flexible tool for constructing compactly supported second generation wavelets which are not necessarily translates and dilates of one *mother* wavelet [75]. We have seen that the lifting scheme uses a simple basis function and builds a more performant one with desirable properties. Flexibility afforded by the lifting scheme allows basis functions to change their shapes near the boundaries without degrading regularities. The lifting scheme also provides faster processing by making optimal use of similarities between high and low pass filters. The lifting algorithm was originally introduced to construct biorthogonal wavelets associated with interpolating scaling functions. Daubechies and Sweldens later generalized it to construct *any* wavelets with a finite number of lifting steps [77].

The lifting scheme utilizes a classical two-channel filter bank as a framework for multiresolution analysis. However this traditional framework is not translation invariant [15]. Representations with a translation-invariant characteristic are highly desirable for feature analysis. Mallat and Zhong introduced an adaptive sampling based upon local maxima as an

overcomplete wavelet representation [15].

In this section we address the following question: Can the lifting scheme be used as a framework for overcomplete wavelet representations with feature analysis in mind? Our work addresses this question by investigating each stage of the multiscale analysis described in [75]. We use a *smoothing Lazy* wavelet in the *split* stage which does not subsample, but smooths an input image so that the low-pass channel contains some redundant information. We then show that the following *predict* and *update* stages, based upon specific properties, indeed lead to a useful multiresolution analysis.

We showed how the (primal) lifting equation (2.20) and the dual lifting equation (2.22) were driven and how they can be embedded in a framework for a multiscale analysis which is implemented in the filter bank coding system shown in Figure 45. This computational structure was simplified later in a semantic form in Figure 46. Here the filters followed by successive subsampling was defined as the *Lazy* wavelet transform which simply *splits* an original signal into odd and even subsets. The dual lifting *predicted* wavelet coefficients with the help of the scaling function coefficients based upon the correlation present in the finer signal. The primal lifting then *updated* the scaling function coefficients using the previously predicted wavelet coefficients to remove possible aliasing resulted from the downsampling.

For overcomplete representations, we introduce a *smoothing lazy wavelet* in the split stage which does not downsample the input image so that $\lambda_{j+1, k} = \lambda_{j, l} = \gamma_{j, m}$. Here we choose the indices so that $j \in J$, $l \in K(j)$, $k \in K(j+1)$, and $m \in M(j)$ where $M(j) = K(j+1) \setminus K(j)$. We then smooth $\lambda_{j, k}$ using a smoothing filter, which is often a Gaussian [15]. This new splitting methodology in the filter bank scheme is then followed by the decorrelation of wavelet coefficients using the dual lifting. Since the new *split* operation does not use downsampling to make distinct subsets $\{\lambda_{j, l}\}$ and $\{\gamma_{j, l}\}$, there is no aliasing. The primal lifting introduced to compensate for the aliasing by preserving energy between two contiguous approximations needs no longer exist. The new forward and inverse wavelet transform algorithm for overcomplete representations can thus be formulated as

FORWARD TRANSFORM

$$\text{Split: } \lambda_{j, l} = \sqrt{2} \sum_{k} \tilde{h}_{k-2l} \lambda_{j+1, k} \ , \ \gamma_{j, m} = \lambda_{j+1, k}$$

$$\text{Dual Lifting: } \gamma_{j, m} = \gamma_{j, m} - \sum_{n=0}^{N-1} \tilde{s}_n \lambda_{j, m-2n} \tag{2.40}$$

120

INVERSE TRANSFORM

$$\text{Inverse Dual Lifting: } \gamma_{j,m} = \gamma_{j,m} + \sum_{n=0}^{N-1} \tilde{s}_n \lambda_{j,m-2n} \qquad (2.41)$$

$$\text{Join: } \lambda_{j+1,k} = \lambda_{j,l} + \gamma_{j,m}$$

where $K(j+1)$, $L(j)$ and $M(j)$ are index sets such that $|K(j+1)| = |M(j)| = |K(j)|$, $\{k \mid k \in K(j+1)\}$, $\{l \mid l \in L(j)\}$ and $m \mid m \in M(j)$. $\tilde{N}$ and N are primal and dual vanishing moments, respectively. Figure 57 shows an undecimated version of two channel analysis/ synthesis filter bank with the newly proposed *overcomplete lifting scheme*. By iterating this scheme through the low-pass channel, we can achieve the 1-D discrete wavelet transform for overcomplete multiscale representations.

In the previous section we discussed how interpolating scaling functions are related to the lifting scheme through the interpolating subdivision proposed by Deslauriers and Dubuc [82]. Here we use the same mechanism, but the approach is different. Instead of refining samples by filling each middle point between two contiguous samples at a finer level using subdivision with a constant spatial support, we keep the size of the samples constant throughout the decomposition, but change the support of the filter associated with the interpolating scaling function.

Figure 58 illustrates how to compute the wavelet coefficients with a cubic dual lifting polynomial ($N = 4$). In this figure, we show how the samples at the next analyzing level are related to the samples at the finer level using two points one of which is near the left boundary, and other
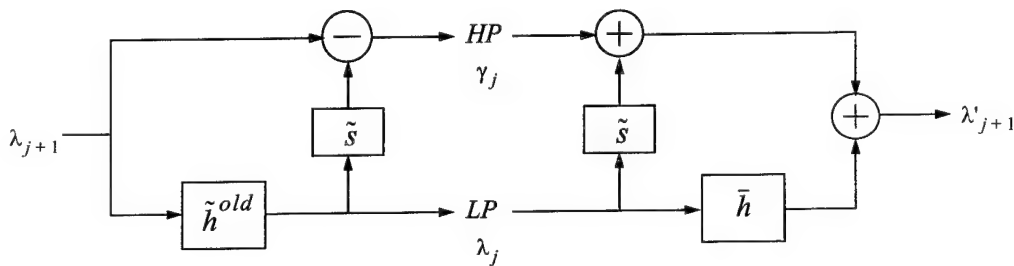
Figure 57. Undecimated version of a two channel filter bank with the proposed *overcomplete lifting*.

$$\{\lambda_{j,k}\}$$

$$\{\gamma_{j,m}\}$$

$$\{\lambda'_{j,l}\} \text{ where } \lambda' = \sum_{n=0}^{3} \tilde{s}_n \lambda_{j,m,n}$$
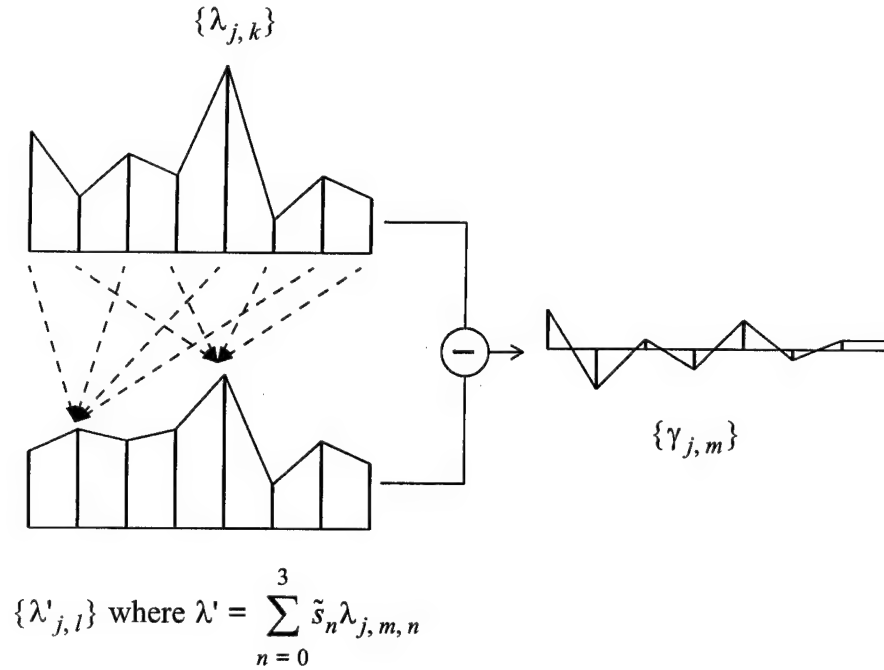
Figure 58. Forward wavelet transform to extract detail information as failures to be cubic.

not. The predicted wavelet coefficients contain the amount by which the coarser approximation locally fails to be cubic. Here the dual lifting coefficients $\tilde{s} = \{-0.0625, 0.5625, 0.5625, -0.0625\}$. The coefficients are adjusted near the boundaries of the finite input signal to avoid boundary effects. For $N = 6$, $\tilde{s} = \{0.0117, -0.0977, 0.5859, 0.5859, -0.0977, 0.0117\}$ and $\tilde{s} = \{-0.0024, 0.0239, -0.1196, 0.5981, 0.5981, -0.1196, 0.0239, -0.0024\}$ for $N = 8$.

For images, 2D masks can be used. Figure 59(a) is a mask for $N = 4$ which is used for regions which are not affected by the boundaries. Figure 59(b) is for the pixel (0, 0) of an image.

$$
\begin{bmatrix}
0.0039 & -0.0352 & -0.0352 & 0.0039 \\
-0.0352 & \boxed{0.3164} & 0.3164 & -0.0352 \\
-0.0352 & 0.3164 & 0.3164 & -0.0352 \\
0.0039 & -0.0352 & -0.0352 & 0.0039
\end{bmatrix}
$$

(a)

$$
\begin{bmatrix}
\boxed{4.7852} & -4.7852 & 2.8711 & -0.6836 \\
-4.7852 & 4.7852 & -2.8711 & 0.6836 \\
2.8711 & -2.8711 & 1.7227 & -0.4102 \\
-0.6836 & 0.6836 & -0.4102 & 0.0977
\end{bmatrix}
$$

(b)

Figure 59. Examples of 2-D masks of dual lifting coefficients for $N = 4$. (a) A mask for regions which are not affected by the boundaries. (b) A mask for the point (0, 0) of an input image. Rectangles indicate points that are modified by masking operations.

The proposed algorithm has been applied to a mammogram of size 512 by 512. We used a cubic spline-based filter for H described in [15] for the smoothing lazy wavelet transform. For the dual lifting, we applied a cubic polynomial with coefficients $\tilde{s} = \{-0.0625, 0.5625, 0.5625, -0.0625\}$. Figure 60 shows wavelet representations for three levels of analysis. We used the wavelet coefficients to reconstruct an image with an error on the order of 11.3dB. Since the lifting scheme can speed up wavelet processing by a factor of two [76] and convolution using a *block algorithm* can further reduce processing time by two-fold within each analyzing level [85], the proposed algorithm can achieve an overall speedup of 4 over the standard overcomplete wavelet transform where an FFT is the basic implementation tool. As pointed out in [85], the FFT method performs best when the filter length is long (over 16 taps). These results suggest that our approach for computing overcomplete wavelet representations with compactly supported lifting filters, compared to existing algorithms, is significantly more efficient.

2.4.8 Summary

We have shown that the lifting algorithm works well in more general domain since wavelets computed from lifting change shape near boundaries without degrading regularity. This property alleviates boundary artifacts which appear in existing algorithms. Thus our algorithm provides a robust way of computing wavelet coefficients of mammograms for arbitrary domains (ROI).

We have shown an approach for computing overcomplete wavelet representations with compactly supported lifting filters. The *Overcomplete Lifting Scheme* performed more efficiently than traditional (existing) methods. This algorithm will provide the computational speed up, needed to carry out methods of multiscale enhancement processing interactively, on diagnostic electronic display systems in the future.

Original Mammogram   Reconstructed Mammogram
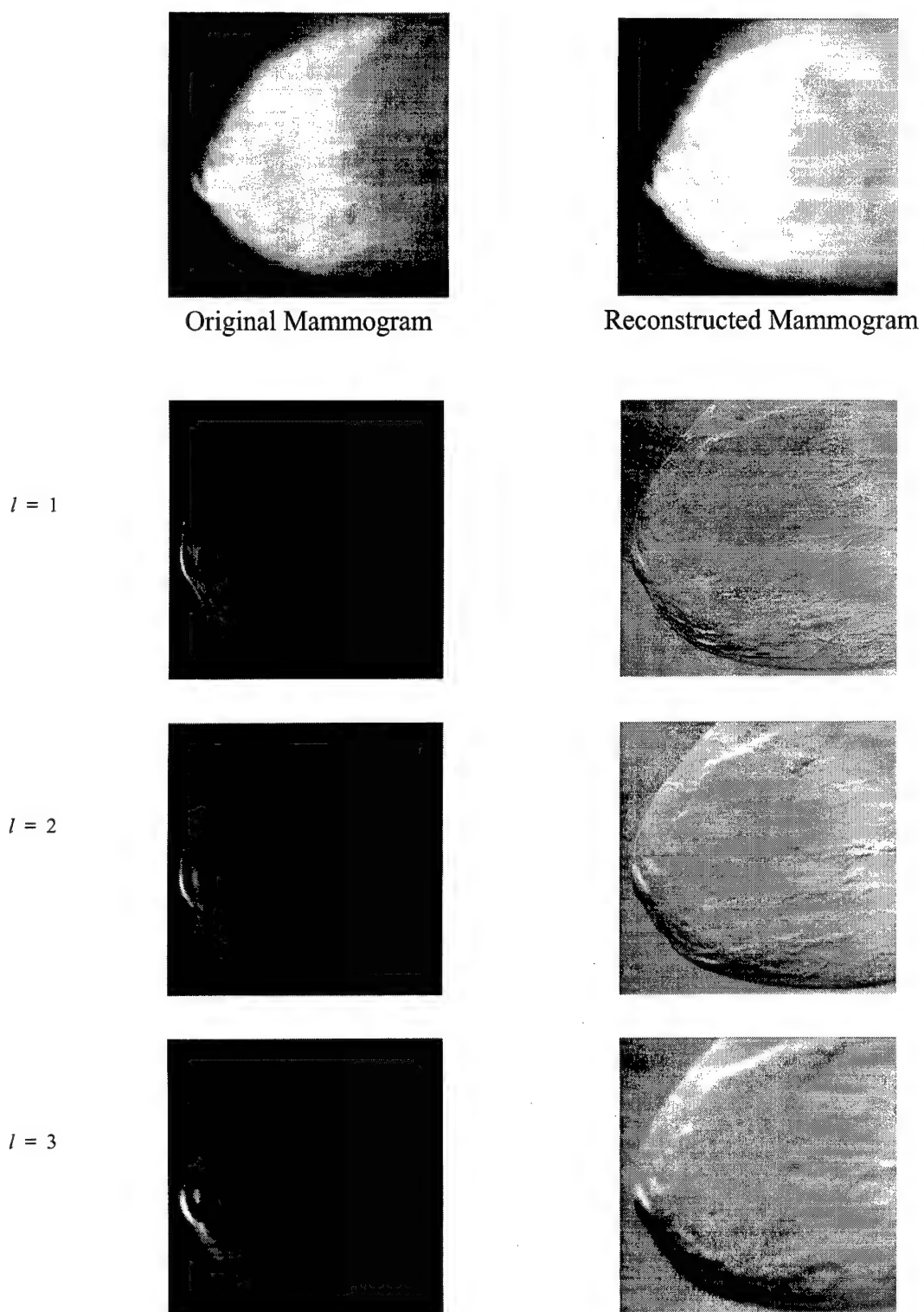
$l = 1$

$l = 2$

$l = 3$

Figure 60. Wavelet coefficients of a mammogram with the proposed scheme. The first and second column show the wavelet coefficients in horizontal direction and vertical direction, respectively.

3 Conclusions

In the paragraphs below, we summarize the results and progress made during the past year and identify the final tasks of our investigation to be carried out during the last year of the project.

We extended the one-dimensional discrete dyadic wavelet transform to two dimensions and showed that in case of wavelets being equal to the second derivative of a central B-spline function, the two-dimensional discrete dyadic wavelet transform decomposition is included in the multiscale spline derivative-based transform decomposition. This attests to the flexibility of the latter transform, which can incorporate a variety of wavelet based mammographic image enhancement methods.

The multiscale spline derivative-based transform was used for a novel image enhancement scheme: the input image was first processed for enhancement of specific mammographic features, and the resultant enhanced images were fused into a final result. The described scheme represents a synthesis between our early global methods developed for an overall improvement of image quality and the local processing, targeting specific mammographic features.

The employed transform is highly redundant, and efficient implementation is of particular importance. We presented a fast filter bank implementation that takes advantage of filter and signal symmetries. Tests of our method included convincing quantitative evidence in terms of improved visibility and detection of subtle features.

We derived and formulated a mass detector, based on multiscale analysis, that very finely samples the scale parameter, in search for subtle masses in mammography. The importance of arbitrary scale analysis was demonstrated by digital radiographs of a mammography phantom and digitized mammograms. For the first time, wavelets and CFAR detectors were combined into a single formulation. We demonstrated that this powerful detector was able to detect very subtle masses, which were rated to be almost invisible by radiologist specializing in mammography.

We embedded a maxima-across-scale scheme [51, 52] under a wavelet framework. And showed that wavelet maxima across scales can provide boundary information of an object and indicate its location. By combining wavelet theory and the geometric knowledge of a tumor, we propose to use a normalized contrast as an index to find the best scale. This method appeared to be promising in selecting the best scale (automatically) for tumor detection.

An enhancement algorithm relying on multiscale wavelet analysis and extracting oriented information at each scale of analysis was investigated. The evolution of wavelet coefficients

across scales characterized the local shape of irregular structures. Using oriented information to detect the features proved to be an effective method of enhancing complex and subtle structures of the breast. Steerable filters, rotated at arbitrary orientations reliably found visual cues within each spatial-frequency sub-band of an image. Coherence measure and dominant orientation clearly helped to discriminate features from complex surrounding tissue in mammograms.

The lifting scheme alone can speed up wavelet analysis processing by a factor of two [76]. In addition, since convolution using a block algorithm can further reduce processing time by two fold within each level of analysis [85], our proposed algorithm can achieve an overall speedup of four over standard overcomplete wavelet transform computations where an FFT is the basic implementation tool. As pointed out in [32], the FFT method performs best when the filter length is long (over 16 taps). These results suggest that our approach for computing overcomplete wavelet representations with compactly supported lifting filters, compared to existing algorithms, is significantly more efficient than previously known methods. This algorithm will provide the computational speed up, needed to carry out methods of multiscale enhancement processing interactively, on diagnostic electronic display systems in the future.

As mentioned in the overview of this report, the final report of the project will contain the results of an ongoing ROC study. This study is being carried out in collaboration with radiologists and medical physicists at Columbia-Presbyterian Hospital at Columbia University.

References

[1] S. L. Parker, T. Tong, S. Bolden, and P. A. Wingo, "Cancer statistics 1996", *CA–A Cancer Journal for Clinicians*, vol. 46, no. 1, pp. 5–27, 1996.

[2] R. A. Smith, "Epidemiology of breast cancer", in *A Categorical Course in Physics, Technical Aspects of Breast Imaging*, A. G. Haus and M. J. Yaffe, Eds. The 79th Scientific Assembly and Annual Meeting of the Radiological Society of North America (RSNA), 1993, pp. 21–33.

[3] P. C. Johns and M. J. Yaffe, "X-ray characterization of normal and neoplastic breast tissues", *Physics in Medicine and Biology*, vol. 32, no. 6, pp. 675–695, 1987.

[4] M. J. Yaffe, R. J. Jennings, R. Fahrig, and T. R. Fewell, "X-ray spectral considerations for mammography", in *A Categorical Course in Physics, Technical Aspects of Breast Imaging*, A. G. Haus and M. J. Yaffe, Eds. The 79th Scientific Assembly and Annual Meeting of the Radiological Society of North America (RSNA), 1993, pp. 63–72.

[5] C. E. Metz, "ROC methodology in radiologic imaging", *Investigative Radiology*, vol. 21, pp. 720–733, 1986.

[6] C. E. Metz, "Practical issues of experimental design and data analysis in radiological ROC studies", *Investigative Radiology*, vol. 24, pp. 234–245, 1989.

[7] C.-M. Chang and A. Laine, "Enhancement of mammograms from oriented information", in *Proceedings of the IEEE International Conference on Image Processing*, Santa Barbara, CA, 1997, vol. 3, pp. 524–527.

[8] J. Fan and A. Laine, "Multiscale contrast enhancement and denoising in digital radiographs", in *Wavelets in Medicine and Biology*, A. Aldroubi and M. Unser, Eds., Boca Raton, FL, 1996, pp. 163–189, CRC Press.

[9] A. F. Laine, S. Schuler, J. Fan, and W. Huda, "Mammographic feature enhancement by multiscale analysis", *IEEE Transactions on Medical Imaging*, vol. 13, no. 4, pp. 725–740, 1994.

[10] W. M. Morrow, R. B. Paranjape, R. M. Rangayyan, and J. E. L. Desautels, "Region-based contrast enhancement of mammograms", *IEEE Transactions on Medical Imaging*, vol. 11, no. 3, pp. 392–406, 1992.

[11] R. N. Strickland and H. I. Hahn, "Wavelet transform matched filters for the detection and classification of microcalcifications in mammography", in *Proceedings of the IEEE International Conference on Image Processing*, Washington, D.C., 1995, vol. 1, pp. 422–425.

[12] R. N. Strickland and H. I. Hahn, "Wavelet transforms for detecting microcalcifications in mammograms", *IEEE Transactions on Medical Imaging*, vol. 15, no. 2, pp. 218–229, 1996.

[13] H. Yoshida, W. Zhang, W. Cai, K. Doi, R. M. Nishikawa, and M. L. Giger, "Optimizing wavelet transform based on supervised learning for detection of microcalcifications in digital mammograms", in *Proceedings of the IEEE International Conference on Image Processing*, Washington, D.C., 1995, vol. 3, pp. 152–155.

[14] I. Koren, A. Laine, F. Taylor, and M. Lewis, "Interactive wavelet processing and techniques applied to digital mammography", in *Proceedings of the IEEE International Conference on Acoustics, Speech, and Signal Processing*, Atlanta, GA, 1996, vol. 3, pp. 1415–1418.

[15] S. Mallat and S. Zhong, "Characterization of signals from multiscale edges", *IEEE Transactions on Pattern Analysis and Machine Intelligence*, vol. 14, no. 7, pp. 710–732, 1992.

[16] I. Daubechies, *Ten Lectures on Wavelets*, SIAM, Philadelphia, PA, 1992.

[17] M. Unser, A. Aldroubi, and S. J. Schiff, "Fast implementation of the continuous wavelet transform with integer scales", *IEEE Transactions on Signal Processing*, vol. 42, no. 12, pp. 3519–3523, 1994.

[18] C. E. Shannon, "Communication in the presence of noise", *Proceedings of the IRE*, vol. 37, no. 1, pp. 10–21, 1949.

[19] M. Unser, A. Aldroubi, and M. Eden, "Polynomial spline signal approximations: Filter design and asymptotic equivalence with Shannon's sampling theorem", *IEEE Transactions on Information Theory*, vol. 38, no. 1, pp. 95–103, 1992.

[20] M. Unser, A. Aldroubi, and M. Eden, "Fast B-spline transforms for continuous image representation and interpolation", *IEEE Transactions on Pattern Analysis and Machine Intelligence*, vol. 13, no. 3, pp. 277–285, 1991.

[21] M. Holschneider, R. Kronland-Martinet, J. Morlet, and Ph. Tchamitchian, "A real-time algorithm for signal analysis with the help of the wavelet transform", in *Wavelets: Time-frequency Methods and Phase Space*, J. M. Combes, A. Grossmann, and Ph. Tchamitchian, Eds., Springer-Verlag, Berlin, Germany, 1990, pp. 286–304.

[22] C. de Boor, *A Practical Guide to Splines*, Springer-Verlag, New York, NY, 1978.

[23] A. J. Jerri, "The Shannon sampling theorem—its various extensions and applications: A tutorial review", *Proceedings of the IEEE*, vol. 65, no. 11, pp. 1565–1596, 1977.

[24] J. Canny, "A computational approach to edge detection", *IEEE Transactions on Pattern Analysis and Machine Intelligence*, vol. 8, no. 6, pp. 679–698, 1986.

[25] D. Marr and E. Hildreth, "Theory of edge detection", *Proceedings of the Royal Society of London*, vol. 207, no. 1167, pp. 187–217, 1980.

[26] A. Laine, J. Fan, and S. Schuler, "A framework for contrast enhancement by dyadic wavelet analysis", in *Digital Mammography*, A. G. Gale, S. M. Astley, D. R. Dance, and A. Y. Cairns, Eds., Amsterdam, The Netherlands, 1994, pp. 91–100, Elsevier.

[27] I. Koren, A. Laine, and F. Taylor, "Image fusion using steerable dyadic wavelet transform", in *Proceedings of the IEEE International Conference on Image Processing*, Washington, D.C., 1995, vol. 3, pp. 232–235.

[28] W. P. Kegelmeyer Jr., J. M. Pruneda, P. D. Bourland, A. Hillis, M. W. Riggs, and M. L. Nipper, "Computer-aided mammographic screening for spiculated lesions", *Radiology*, vol. 191, no. 2, pp. 331–337, 1994.

[29] W. T. Freeman and E. H. Adelson, "The design and use of steerable filters", *IEEE Transactions on Pattern Analysis and Machine Intelligence*, vol. 13, no. 9, pp. 891–906, 1991.

[30] I. Koren and A. Laine, "A discrete dyadic wavelet transform for multidimensional feature analysis", in *Time-Frequency and Wavelets in Biomedical Signal Engineering*, M. Akay, Ed., IEEE Press, New York, NY, 1998, pp. 425–449.

[31] A. V. Oppenheim and R. W. Schafer, *Discrete-Time Signal Processing*, Prentice-Hall, Englewood Cliffs, NJ, 1989.

[32] O. Rioul and P. Duhamel, "Fast algorithms for discrete and continuous wavelet transforms", *IEEE Transactions on Information Theory*, vol. 38, no. 2, pp. 569–586, 1992.

[33] B. Friedlander and B. Porat, "Performance analysis of transient detectors based on a class of linear data transforms", *IEEE Transactions on Information Theory*, vol. 38, no. 2, pp. 665–673, 1992.

[34] M. Frisch and H. Messer, "The use of the wavelet transform in the detection of an unknown transient signal", *IEEE Transactions on Information Theory*, vol. 38, no. 2, pp. 892–897, 1992.

[35] S. D. Marco and J. Weiss, "M-band wavepacket-based transient signal detector using a translation-invariant wavelet", *Optical Engineering*, vol. 33, no. 7, pp. 2175–2182, 1994.

[36] D. P. Casasent, J. Smokelin, and A. Ye, "Wavelet and Gabor transforms for detection", *Optical Engineering*, vol. 31, no. 9, pp. 1893–1898, 1992.

[37] D. Chen, C.-M. Chang, and A. Laine, "Detection and enhancement of small masses via precision multiscale analysis", in *Proceedings of the Third Asian Conference on Computer Vision*, Hong Kong, PRC, 1998, vol. 1, pp. 192–199.

[38] A. Laine, W. Huda, D. Chen, and J. Harris, "Segmentation of masses using continuous scale representations", in *Digital Mammography*, K. Doi, M. L. Giger, R. M. Nishikawa, and R. A. Schmidt, Eds., Amsterdam, The Netherlands, 1996, pp. 447–450, Elsevier.

[39] I. Daubechies, "The wavelet transform, time-frequency localization and signal analysis", *IEEE Transactions on Information Theory*, vol. 36, no. 5, pp. 961–1005, 1990.

[40] M. Vrhel, C. Lee, and M. Unser, "Fast computation of the continuous wavelet transform through oblique projections", in *Proceedings of the IEEE International Conference on Acoustics, Speech and Signal Processing*, Atlanta, GA, 1996, pp. 1459–1462.

[41] M. Vrhel, C. Lee, and M. Unser, "Fast continuous wavelet transform", in *Proceedings of the IEEE International Conference on Acoustics, Speech and Signal Processing*, Detroit, MI, 1995, pp. 1165–1168.

[42] L. M. Novak, M. B. Sechtin, and M. J. Cardullo, "Studies of target detection algorithms that use polarimetric radar data", *IEEE Transactions on Aerospace and Electronic Systems*, vol. 25, no. 2, pp. 150–165, 1989.

[43] A. Grossmann and J. Morlet, "Decomposition of Hardy functions into square integrable wavelets of constant shape", *SIAM Journal on Mathematical Analysis*, vol. 15, no. 4, pp. 723–736, 1984.

[44] A. Aldroubi and M. Unser, "Sampling procedures in function spaces and asymptotic equivalence with Shannon's sampling theory", *Numerical Functional Analysis and Optimization*, vol. 15, no. 1–2, pp. 1–21, 1994.

[45] G. Strang, "Wavelets and dilation equations: A brief introduction", *SIAM Review*, vol. 31, no. 4, pp. 614–627, 1989.

[46] A. Aldroubi, M. Unser, and M. Eden, "Cardinal spline filters: Stability and convergence to the ideal sinc interpolator", *Signal Processing*, vol. 28, pp. 127–138, 1992.

[47] S. G. Mallat, "A theory for multiresolution signal decomposition: The wavelet representation", *IEEE Transactions on Pattern Analysis and Machine Intelligence*, vol. 11, no. 7, pp. 674–693, 1989.

[48] G. B. Goldstein, "False-alarm regulation in log-normal and Weibull clutter", *IEEE Transactions on Aerospace and Electronic Systems*, vol. 9, no. 1, pp. 84–92, 1973.

[49] A. G. Haus and M. J. Yaffe, *A Categorical Course in Physics: Technical Aspects of Breast Imaging*, The 80th Scientific Assembly and Annual Meeting of the Radiological Society of North America (RSNA), Oak Brook, IL, 1994.

[50] S. Mallat and W. L. Hwang, "Singularity detection and processing with wavelets", *IEEE Transactions on Information Theory*, vol. 38, no. 2, pp. 617–643, 1992.

[51] T. Lindeberg, "On scale selection for differential operators", in *Proceedings of Scandinavian Conference on Image Analysis*, A. Hanson and E. Riseman, Eds., Troms, Norway,, 1993, pp. 857–866, Academic Press.

[52] D. Chen, J. G.Harris, and A. F. Laine, "Automatic scale detection", in *Visual Communications and Image Processing* Proceedings of SPIE, Orlando, FL, 1996, vol. 2727, pp. 960–972.

[53] R. L. Egan, *Breast Imaging*, W. B. Saunders Company, Philadelphia, PA, 1988.

[54] R. McLelland, "Stellate lesions of the breast", *Recent Results in Cancer Research*, vol. 119, pp. 24–27, 1990.

[55] Y. Xing, W. Huda, A. Laine, J. Fan, B. Steinbach, and J. Honeyman, "Comparison of a dyadic wavelet image enhancement algorithm with unsharp masking and median filtering", in *Medical Imaging: Image Processing,* Proceedings of SPIE, San Diego, CA, 1995, vol. 2434, pp. 718–729.

[56] W. Qian, L. P. Clarke, M. Kallergi, H.-D. Li, R. Velthuizen, R. A. Clark, and M. L. Silbiger, "Tree-structured nonlinear filter and wavelet transform for microcalcification segmentation in mammography", in *Biomedical Image Processing and Biomedical Visualization,* Proceedings of SPIE, San Jose, CA, 1993, vol. 1905, pp. 509–520.

[57] W. B. Richardson Jr., "Nonlinear filtering and multiscale texture discrimination for mammograms", in *Mathematical Methods in Medical Imaging,* Proceedings of SPIE, San Diego, CA, 1992, vol. 1768, pp. 293–305.

[58] L. Li, W. Qian, and L. P. Clark, "X-ray medical image processing using directional wavelet transform", in *Proceedings of the IEEE International Conference on Acoustics, Speech, and Signal Processing,* Atlanta, GA, 1996, vol. 4, pp. 2251–2254.

[59] M. Kass and A. Witkin, "Analyzing oriented patterns", *Computer Vision, Graphics, and Image Processing,* vol. 37, no. 3, pp. 362–385, 1987.

[60] A. R. Rao and B. G. Schunck, "Computing oriented texture fields", in *Proceedings of the IEEE Computer Society Conference on Computer Vision and Pattern Recognition,* San Diego, CA, 1989, pp. 61–68.

[61] M. C. Morrone and R. A. Owens, "Feature detection from local energy", *Pattern Recognition Letters,* vol. 6, no. 5, pp. 303–313, 1987.

[62] K. R. Castleman, *Digital Image Processing,* Prentice-Hall Inc., Upper Saddle River, NJ, 1996.

[63] H. G. Barrow and J. M. Tenenbaum, "Recovering intrinsic scene characteristics from images", in *Computer Vision Systems,* A. Hanson and E. Riseman, Eds., New York, NY, 1978, pp. 3–26, Academic Press.

[64] D. Marr, *Vision,* Freeman, San Francisco, CA, 1982.

[65] C.-M. Chang, *Coherence of multiscale features for enhancement of digital mammograms,* PhD thesis, University of Florida, 1997.

[66] M. J. Shensa, "The discrete wavelet transform: Wedding the à trous and Mallat algorithms", *IEEE Transactions on Signal Processing*, vol. 40, no. 10, pp. 2464–2482, 1992.

[67] A. Laine and C.-M. Chang, "De-noising via wavelet transforms using steerable filters", in *IEEE International Symposium on Circuits and Systems*, Seattle, WA, 1995, vol. 3, pp. 1956–1959.

[68] J. J. Koenderink and A. J. van Doorn, "Generic neighborhood operators", *IEEE Transactions on Pattern Analysis and Machine Intelligence*, vol. 14, no. 6, pp. 597–605, 1992.

[69] P. Perona, "Deformable kernels for early vision", *IEEE Transactions on Pattern Analysis and Machine Intelligence*, vol. 17, no. 5, pp. 488–499, 1995.

[70] N. Karssemeijer and G. M. te Brake, "Detection of stellate distortions in mammograms", *IEEE Transactions on Medical Imaging*, vol. 15, no. 5, pp. 611–619, 1996.

[71] R. Owens, S. Venkatesh, and J. Ross, "Edge detection is a projection", *Pattern Recognition Letters*, vol. 9, no. 4, pp. 233–244, 1989.

[72] E. L. Hall, *Computer Image Processing and Recognition*, Academic Press, New York, NY, 1979.

[73] E. Peli, "Contrast in complex images", *Journal of the Optical Society of America A*, vol. 7, no. 10, pp. 2032–2040, 1990.

[74] A. F. Laine, J. Fan, and W. Yang, "Wavelets for contrast enhancement of digital mammography", *IEEE Engineering in Medicine and Biology*, vol. 14, no. 5, pp. 536–550, 1995.

[75] W. Sweldens, "The lifting scheme: A new philosophy in biorthogonal wavelet constructions", in *Wavelet Applications III*, Proceedings of SPIE, San Diego, CA, 1995, vol. 2569, pp. 68–79.

[76] W. Sweldens, "The lifting scheme: A custom-design construction of biorthogonal wavelets", *Applied and Computational Harmonic Analysis*, vol. 3, no. 2, pp. 186–200, 1996.

[77] I. Daubechies and W. Sweldens, "Factoring wavelet transforms into lifting steps", Tech. Rep., Bell Laboratories, Lucent Technologies, 1996.

[78] I. Daubechies, "Orthonormal bases of compactly supported wavelets", *Communications on Pure and Applied Mathematics*, vol. 41, no. 7, pp. 909–996, 1988.

[79] I. Daubechies A. Cohen and J. Feauveau, "Biorthogonal bases of compactly supported wavelets", *Communications on Pure and Applied Mathematics*, vol. 45, pp. 485–560, 1992.

[80] M. Vetterli and C. Herley, "Wavelets and filter banks: Theory and design", *IEEE Transactions on Signal Processing*, vol. 40, no. 9, pp. 2207–2232, 1992.

[81] W. Sweldens, "Building your own wavelets at home", *Wavelets in Computer Graphics, ACM SIGGRAPH Course notes*, pp. 15–87, 1996.

[82] G. Deslauriers and S. Dubuc, "Symmetric iterative interpolating processes", *Constructive Approximation*, vol. 5, no. 1, pp. 49–68, 1989.

[83] D. L. Donoho, "Interpolating wavelet transforms", Tech. Rep., Department of Statistics, Stanford University, 1992.

[84] A. Grossmann, R. Kronland-Martinet, and J. Morlet, "Reading and understanding continuous wavelet transforms", in *Wavelets: Time-frequency Methods and Phase Space*, J. M. Combes, A. Grossmann, and Ph. Tchamitchian, Eds., Springer-Verlag, Berlin, Germany, 1990, pp. 2–20.

[85] M. Shim and A. Laine, "A fast algorithm to support interactive wavelet processing on a radiologist workstation", Tech. Rep. TR97-022, Computer and Information Science and Engineering Department, University of Florida, 1997.